CHEMISTRY OF MATERIALS

pubs.acs.org/cm

Review

Advances in the Synthesis of Halide Perovskite Single Crystals for Optoelectronic Applications

Jiakai Yan, Haojin Li, Mahmoud Hussein Aldamasy, Chiara Frasca, Antonio Abate,* Kui Zhao,* and Yue Hu*

Cite This: *Chem. Mater.* 2023, 35, 2683−2712

Read Online

ACCESS | Metrics & More | Article Recommendations

ABSTRACT: Perovskite materials have attracted much attention in various optoelectronics applications such as solar cells, light-emitting diodes, and photodetectors. Compared to multicrystalline films, single crystal perovskites are free of grain boundaries and exhibit lower defect density, longer carrier lifetimes, longer carrier diffusion distances, and outstanding stability, thus having the potential to show superior performances in optoelectronic devices. In addition, single crystal nanostructures are ideal model systems for studying the fundamental optoelectronic properties of newly designed functional materials. This review provides a thorough introduction to the fundamental theories behind crystal nucleation and growth. In addition, we provide an in-depth analysis of the application of classic ideas to the experimental formation of perovskite crystals including inorganic and hybrid halide perovskites with low-dimensional and three-dimensional structures. Subsequently, we correlate the crystal structure and optoelectronic properties and summarize the recent advances in the application of perovskite single crystals in various optoelectronic devices. Finally, we discuss the ongoing challenges in single crystal growth and the emerging optoelectronic applications. This review will serve as a valuable resource for future studies on the synthesis and uses of perovskite single crystals.

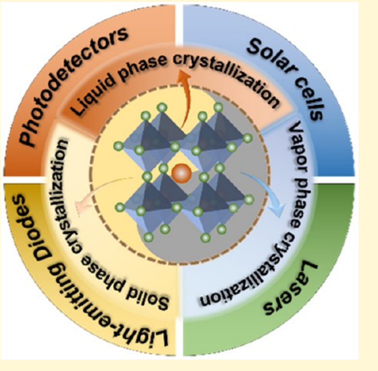

1. INTRODUCTION

Recently, lead halide perovskites received considerable research attention due to their excellent optoelectronic properties, making them suitable for various optoelectronic applications. In 1978, Weber et al. synthesized organic−inorganic hybrid metal halide perovskites for the first time by replacing Cs ions with organic methylammonium (MA^+) cations in an inorganic perovskite previously synthesized by Møller.[1] Since then, metal halide perovskites' unique chemical and physical properties have been studied widely. The community did not recognize the exceptional optoelectronic capabilities of the perovskites until 2009, when Miyasaka et al. introduced $MAPbI_3$ and $MAPbBr_3$ into the photovoltaic (PV) application. Compared with other PV materials, metal halide perovskites exhibit many advantages such as tunable bandgap,[2−14] high light absorption capability,[14−16] long carrier lifetime,[17−20] and diffusion length.[21−24] Very soon, they were applied in a variety of optoelectronics and showed excellent performance in lasers,[25−28] luminescent devices,[29−32] photodetectors,[33−35] and high-energy ray detectors,[36,37] as shown in Figure 1.

Currently, perovskite polycrystalline thin films are commonly used in optoelectronic applications. However, these films tend to contain many grain boundaries and charge traps, which increase the nonradiative charge recombination and ion migration and limit the development of optoelectronic

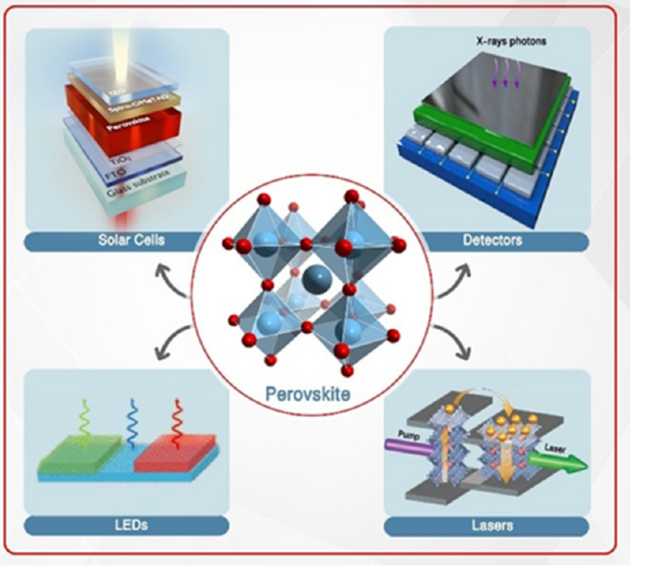

Figure 1. Main applications of perovskite materials.

Received: November 23, 2022
Revised: March 9, 2023
Published: March 24, 2023

https://doi.org/10.1021/acs.chemmater.2c03505
Chem. Mater. 2023, 35, 2683−2712

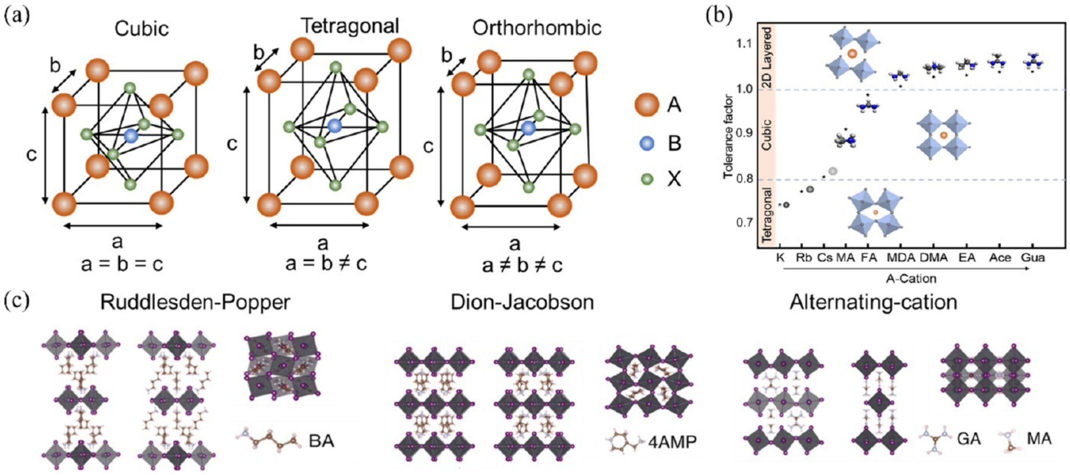

Figure 2. (a) Schematic lattices of 3D perovskites. Reproduced from permission.[52] Copyright 2016, Royal Society of Chemistry. (b) Relationship between the composition and the tolerance factor ($B = Pb^{2+}$, $X = I^-$), where K = potassium (138 pm), Rb = Rubidium (152 pm), Cs = Cesium (167 pm), MA = methylammonium (217 pm), FA = formamidinium (253 pm), MDA = methylenediammonium (262 pm), DMA = dimethylammonium (272 pm), EA = ethylammonium (274 pm), Ace = acetamidinium (277 pm), Gua = guanidinium (278 pm). Reproduced with permission from ref 53. Copyright 2018, American Chemical Society. (c) Example of 2D perovskite with different crystal structures. Reproduced with permission from ref 54. Copyright 2019, American Chemical Society.

devices.[38−41] Relative to polycrystalline thin films, perovskite single crystals (SCs) exhibit higher carrier mobilities,[15,17,42] lower trap state densities,[17,23,42] longer carrier diffusion lengths[15,22,23,42,43] and larger light absorption coefficients.[14,44] In addition, the intrinsic material properties are best demonstrated in SCs, which are the ideal vehicle for the intrinsic structure of materials. Therefore, high-quality perovskite SCs are important for studying material properties and subsequent device fabrication. Low-defect single crystals are the optimum semiconductor material for optoelectronic devices. To further increase the performance of these devices, a considerable scientific effort is devoted to synthesis perovskite SCs and prepare single-crystal optoelectronic devices. The first synthesis of three-dimensional (3D) perovskite materials based on $CsPbX_3$ ($X = Cl^-$, Br^-, and I^-) was made by H. L. Wells as early as 1892, and in 1957 these materials were identified as perovskite crystal structure with a semiconductive nature by C. K. Møller.[45,46] In 1977, Huber et al. synthesized two-dimensional (2D) layered perovskite SCs of $(C_nH_{n+1}NH_3)_2MX_4$ and $NH_3(CH_2)_mNH_3MX_4$ (n = 1, 2,..., 18 and m = 2, 3,..., 8). Therein, M and X represent divalent metal ions of Cl^- or Br^-, respectively.[47] In 1987, Weber et al. produced 3D perovskite SCs of $MAPbX_3$, where $X = Cl^-$, Br^-, and I^-, and explored the dependence of the crystal structure on the temperature.[1] On the other hand, Mitzi et al. fabricated 3D perovskite $MASnI_3$ SCs in 1995.[48] Numerous methods were developed for preparing and growing high-quality metal halide SCs. The quality of the synthesized SCs improved with advancements in the synthesis and growing techniques for perovskite crystals. Then, by reducing the solution temperature and evaporation rate, Lemmerer et al. grew 2D high-quality perovskite $(C_nH_{2n+1}NH_3)_2PbI_4$ (n = 4, 5, and 6) SCs.[2] In 2014, Tao et al. greatly developed large $MAPbI_3$ SCs through the solution temperature-lowering method.[14] In 2015, Bakr et al. pioneered synthesizing a series of $MAPbI_3$ SCs through the inverse temperature crystallization method.[49] For the melting method, Kanatzidis et al. synthesized all-inorganic perovskite $CsPbBr_3$ SCs in 2013.[50] Later, Hodes et al. successfully prepared high-quality perovskite $CsPbBr_3$ SCs through an antisolvent vapor-assisted method.[51]

Techniques for synthesizing and growing metal halide perovskite SCs are being developed, and they have varying effects on the quality and properties of SCs. Choosing the appropriate growing method for particular perovskite crystals is essential, depending on the chemical compositions.

In this review, we provide a valuable reference for future research on the synthesis and applications of perovskite SCs. This review begins with crystal nucleation and growth theory, followed by classifying the different growth methods by the main phases involved in the synthesis. It highlights the continuous improvement, summarizing their pros and cons. Finally, it discusses the applications of perovskite SCs in optoelectronic devices in detail.

2. CRYSTAL STRUCTURE OF PEROVSKITE

Figure 2a shows the structure of metal halide perovskites with the general formula, ABX_3, where A can be an inorganic (e.g., Cs^+, and Rb^+) or organic group (e.g., MA^+, and FA^+) cation, B is a divalent metal cation (e.g., Pb^{2+}, and Sn^{2+}), and X is a halide anion (e.g., Cl^-, Br^-, and I^-). Due to the ease of formation of ionic bonds between the B and X ions, $[BX_6]^{4-}$ octahedral structures could also be easily formed. These octahedral structures form the 3D networks in the organic−inorganic hybrid metal halide perovskite structure.[52] They can also form perovskite cages with the disordered A cations filling the confined octahedral gaps.[53] The ionic radius of each ion in the ABX_3 perovskite crystal structure must be confirmed with the tolerance factor (t), which can be calculated using eq 1

$$t = \frac{R_A + R_B}{\sqrt{2}(R_B + R_X)} \quad (1)$$

where R_A, R_B, and R_X are the ionic radii of A, B, and X, respectively. The ideal cubic perovskite crystal structure can be formed when $0.9 \le t \le 1$ (Table 1). When $0.7 \le t \le 0.9$, cation A is so small that the octahedral gap is not entirely filled; this gap and the octahedral framework are deformed. Therefore, the structure could easily transit into a tetragonal

https://doi.org/10.1021/acs.chemmater.2c03505
Chem. Mater. 2023, 35, 2683−2712

Table 1. Tolerance Factor (t) for Hybrid Perovskites

tolerance factor (t)	structure	description
<0.71		A and B have similar ionic radii
0.71−0.9	tetragonal/orthorhombic/rhombohedral	A is small or B is large
0.9−1.0	cubic	A and B have ideal size
>1.0	hexagonal/tetragonal	A is large or B is small

or orthorhombic crystal lattice. In contrast, when $t < 1$, the octahedral structure dissociates and ceases to be connected at the common vertex, which yields a 2D layered crystal structure, as shown in Figure 2b.[53] The crystal structure, which can be altered by varying the value of t, affects the optoelectronic properties of the perovskite material.

By decreasing the perovskite crystal dimensions, the required t is relaxed, allowing large A cations to enter the perovskite cage as well and forming 2D perovskite crystal structures, such as Ruddlesden−Popper (RP), Dion−Jacobson (DJ), and alternating cation in the interlayer space (ACI) phases, as shown in Figure 2c.[54] The 2D RP and DJ perovskite phases are more widely studied among these crystal structures.[9] In RP perovskites, the organic spacer cations commonly contain an amine group, and the inorganic layers form a staggered arrangement. The tails of the organic cations are connected between the adjacent inorganic layers through van der Waals forces, thereby forming an arrangement connected through feeble intermolecular forces of attraction. Therefore, large interlayer distances may be detrimental to the stability of RP perovskites.[55] In contrast, in DJ perovskites, each organic spacer cation contains two amine groups, which can simultaneously connect to two adjacent inorganic layers, forming a plane that aligns with these adjacent octahedral organic structures. This effectively enhances the interaction forces and reduces distances between adjacent inorganic layers, which could facilitate interlayer charge transfers.[56] Lastly, the ACI structure can be formed by alternating the organic spacer cations to connect two adjacent inorganic layer.

3. PEROVSKITE CRYSTALLIZATION FROM LIQUID PHASE

3.1. Theories of Crystal Nucleation and Growth.

Crystal is a solid substance consisting of a large number of atoms (ions or molecules) arranged in space in a regular periodic repetition. Crystal preparation can be divided into two processes: nucleation and growth. The solid-phase nuclei act as templates for subsequent crystal growth. Crystal nucleation proceeds either through a homogeneous or heterogeneous path. Homogeneous nucleation is the direct formation of nuclei with clusters of atoms in the parent phase.[57] In contrast, heterogeneous nucleation occurs when the new phase forms at heterogeneities, such as foreign surfaces, impurities, grain boundaries, and dislocations, which preferentially occurs in the parent phase.

When a crystal nucleus appears in the parent phase, the atoms in this region gradually convert from an aggregated to an aligned state in the solid phase, decreasing the free energy in the system. The entire nucleation process can be explained using thermodynamic principles. According to the existed classical nucleation theory, ΔG represents the free energy change of the system during homogeneous nucleation of a spherical nucleus with radius r.[58] And ΔG can be defined as the sum of the energy change induced by the surface crystal free energy (σ) and the bulk crystal free energy (ΔG_V) in a spherical nucleus, so the system's total free energy (ΔG) when a crystal nucleus appears can be described using eq 2:

$$\Delta G = 4\pi r^2\sigma + \frac{4}{3}\pi r^3\Delta G_v \quad (2)$$

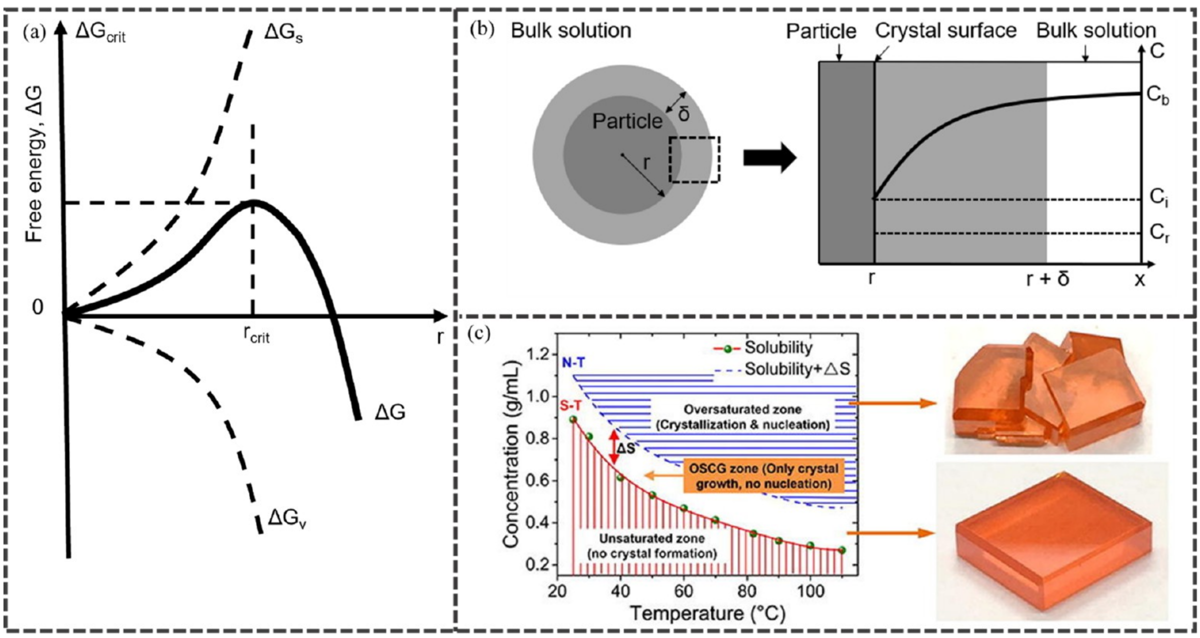

Figure 3. (a) Schematic diagram of heterogeneous nucleation. (b) Diagram of concentration distribution of monomers around particles. Reproduced with permission from ref 62. Copyright 2011, Wiley-VCH. (c) Solubility and concentration curves vs the growth temperature for different regions in the single crystal growth model, and the different $MAPbBr_3$ crystals morphology of different regions. Reproduced with permission from ref 65. Copyright 2019, Elsevier.

However, both variables (σ, ΔG_V) are dependent on temperature (T).[59] Therefore, at a certain value of T, ΔG becomes a function of r. Figure 3a shows the dependence of ΔG with r. In the ΔG vs r curve, the presence of a critical radius (r_{crit}) can be observed. When $r < r_{crit}$, the nucleus redissolves in the solution. When $r \geq r_{crit}$, ΔG_v gradually decreases, and the nucleus becomes stable.

Under experimental conditions, there may be another phase in the parent solution, wherein heterogeneous nucleation can occur. In contrast to homogeneous nucleation, the nuclei form on the surface of heterogeneities in this process.[60]

The precise control of the crystal growth is critical to obtain high-quality crystals. In general, crystal growth depends on the reaction of the solute on the crystal surface and its diffusion into the crystallite.[61] The rate of the reaction on the surface is assumed to be irrelevant to the size of the particles. Figure 3b shows the model for this process. The total flux (J) of the monomers passing through a spherical plane with radius r is defined as, where k is the rate of reaction on the surface related to temperature, C_i is the concentration of monomers at the liquid solution−solid particle interface, and C_r is the solubility of the particles. In contrast, the diffusion-limited process follows Fick's first law of diffusion.[62] However, the rate of diffusion varies exponentially with the temperature. In general, low growth rates yield high-quality crystals.[63]

Aside from the temperature, the solubility of the solute also plays an essential role in the growth of high-quality crystals. The formed crystal nuclei can only grow without extraneous nucleation when the solution is slightly oversaturated, i.e., the solute concentration is just over the solubility limit.[64] Figure 3c illustrates the three phases in single-crystal growth, namely the unsaturated, oversaturated, and optimized growth regions, which are bounded by the solubility (S−T) and nucleation (N−T) curves. First, the saturated solution is necessary for precipitation, so no crystal can be formed in an unsaturated solution below the S−T curve. In addition to the saturated condition, the temperature of the solution also affects the quality of the crystals formed. Second, when the saturated solution is heated to a temperature slightly above S-T curve to enter the oversaturated region, which results in only crystal growth but no nucleation. Therefore, after the solution has formed fewer nuclei during the temperature rising, the solution can be heated to this region to ensure that the nuclei can grow slowly and no new nuclei are formed. Lastly, when the oversaturated solution is heated to a temperature slightly above the N-T curve to enter the supersaturated region, which leads to defects, twins, and fine crystals, as shown in Figure 3c.[65]

A few theories describe the mechanism of crystal nucleation and growth. The primary nucleation mechanism is the LaMer mechanism, wherein nucleation and growth are considered two distinct processes and divided into three stages.[66] First, the concentration of solute in the solution gradually increases and approaches the saturation limit. Once saturation is achieved, nucleation occurs in the solution, which rapidly decreases the solute concentration. Lastly, under solute diffusion, crystal growth starts at the center with the crystal nuclei. As shown in Figure 4a, these three stages appear individually over time.[60]

Moreover, the Ostwald ripening mechanism is founded on the Gibbs−Thompson theory,[67] which implies that tiny particles with high solubility and surface energy rapidly dissolve in solutions. As a result, a concentration gradient forms in the solution due to the difference between the solute concentration around smaller and larger particles; higher solute concentration is often observed around smaller particles. The concentration gradient promotes the movement of the solute toward low-concentration regions. These processes cause small particles to precipitate on the surface of large particles, thereby increasing the size of the particles, as shown in Figure 4b.[68] In contrast, the theory of digestive ripening, described by Lee et al., states that the surface energy-controlled large particles redissolve to support the growth of smaller particles.[69]

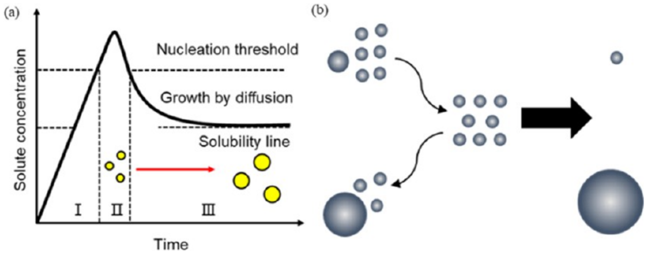

Figure 4. (a) LaMer effect. Reproduced from permission from ref 60. Copyright 1950, American Chemical Society. (b) Ostwald ripening scheme. Reproduced with permission from ref 68. Copyright 1961, Elsevier.

Aside from the LaMer mechanism and Ostwald ripening, other theories, such as the Finke−Watzky two-step mechanism, orientated attachment, and intraparticle growth, are used to explain the nucleation and growth of crystals. In the Finke−Watzky two-step mechanism, nucleation and growth coincide. This phenomenon was observed in the reduction of transition metal salts by cyclohexene. In this mechanism, the first process involves slow and constant nucleation, and the second step presents spontaneous growth that is not controlled by diffusion.[70] On the other hand, orientated attachment was introduced by Penn and Banfield in their work on the hydrothermal synthesis of TiO_2 nanocrystals. In this mechanism, the orientation of the nanocrystals is constant throughout the growth process. Larger particles can be formed by interconnecting the nanoparticles on a shared crystalline surface.[71] The principles of coalescence and orientated attachment are very similar. However, during coalescence, the orientation of the nanoparticles is not consistent.[72]

Liquid phase crystallization techniques are currently the most widely used route to produce high-quality perovskite SCs due to the low cost and simplicity. In these methods, the solubility of the solute in the saturated perovskite precursor solution is gradually reduced to grow the perovskite SCs.

3.2. Solution Temperature-Lowering (STL) Method.

The solution temperature-lowering (STL) approach exploits the fact that the solubility of the perovskite precursor decreases with decreasing solution temperature. This method involves three stages: (i) the mixed solution is heated at a relatively high temperature to form a clear precursor solution, (ii) the precursor solution is continuously cooled to precipitate the seed crystals, (iii) the cooling rate of the precursor solution is controlled to facilitate the growth of the seed crystals. The STL approach has the advantage of being able to control the growth rate of perovskite crystals. Therefore, high-quality and large crystals can be synthesized through this route by controlling slower cooling. Figure 5 shows a schematic of the STL method.

The first organic−inorganic hybrid metal halide perovskites were fabricated using this method. As reported by Weber et al., equimolar amounts of MA^+ and Pb^{2+} ions in an aqueous HX solution yield $MAPbX_3$ crystals (X = Cl^-, Br^-, I^-) through the STL method. Later, this method was employed and refined in

https://doi.org/10.1021/acs.chemmater.2c03505
Chem. Mater. 2023, 35, 2683−2712

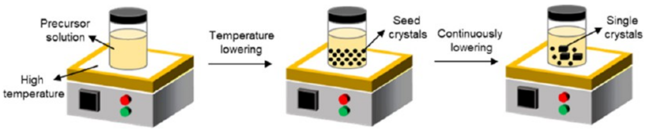

Figure 5. Schematic diagram of STL method.

succeeding research works.[1] Recently, Tao et al. reported the first use of this method to grow centimeter-sized perovskite $MAPbI_3$ SCs, where $Pb(CH_3COOH)_2 \cdot 3H_2O$ and CH_3NH_3I were dissolved in aqueous HI at 70 °C to obtain a clear perovskite precursor solution. At 65 °C, a saturated precursor solution was obtained, which was slowly cooled down to 40 °C to precipitate out the SCs. The dimensions of the synthesized large SCs were $10 \times 10 \times 8$ mm^3, as shown in Figure 6a.[14] Lin et al. also successfully synthesized SCs of MAPbX3 (X = Br−, I−). For the growth of the $MAPbI_3$ crystals, the precursor solution was heated to 90 °C and then cooled down to 45 °C at a precisely controlled cooling rate. Centimeter-sized SCs were obtained, as shown in Figure 6b. The solubility of $MAPbI_3$ in HI acid as a function of temperature was also investigated. Figure 6c shows the corresponding solubility curve. $MAPbBr_3$ SCs with a lateral size greater than 5 mm were also produced after 10 days, as shown in Figure 6d.[73]

In 2016, Kanatzidis et al. employed a similar strategy to grow 2D RP perovskite SCs based on $(CH_3(CH_2)_3NH_3)_2(CH_3NH_3)_{n-1}Pb_nI_{3n+1}$ with n = 1, 2, 3, 4, ∞, as shown in Figure 6e.[10] Since then, this method was extended to other materials to prepare other single-crystal 2D perovskite structures, such as DJ perovskite using $(NH_3C_mH_{2m}NH_3)(CH_3NH_3)_{n-1}Pb_nI_{3n+1}$ with m = 7−9 and n = 1−4, and ACI phase using $(C(NH_2)_3)(CH_3NH_3)_nPb_nI_{3n+1}$ with n = 1, 2, 3.[9,74] In addition to MA-based perovskite SCs, Tisdale et al. synthesized perovskite $(C_4H_9NH_3)_2(FA)Pb_2I_7$ SCs through STL method using larger formamidinium (FA^+) cations.[7] Song et al. obtained low-dimensional Sn-based perovskite SCs, $(BEA)FA_2Sn_3I_{10}$, which exhibited a longer carrier lifetime and higher carrier mobility than the 2D Pb-based perovskite SCs.[75] In the STL method, the corresponding HX (X = Cl^-, Br^-, I^-) acid is the best growth solution for these perovskite SCs, which has better solubility and lower boiling point. Furthermore, aqueous HX can supplement the properties of the corresponding halide cation. On the other hand, Lin et al. used deionized H_2O as a novel solvent for the growth of a single-crystal, all-inorganic perovskite ($CsPbBr_3$). In contrast to the traditional growth process that utilized aqueous HBr, the pure $CsPbBr_3$ phase was stabilized when the $CsBr:PbBr_2$ ratio was ≥1:1 in H_2O; however, $CsPb_2Br_5$ easily formed with excessive amounts of the Br^- ions, as shown in Figure 6f.[19] Other all-inorganic perovskite SCs, such as $CsGeI_3$, were also successfully synthesized in previous reports.[11]

To produce high-quality single crystals, the STL method was optimized into top-seeded solution growth (TSSG) and bottom-seeded solution growth (BSSG) methods.

In the TSSG method, the difference in the solubility of perovskites under a temperature gradient is utilized to grow the single crystals. Initially, seed crystals are fixed on the silicon substrate at the top of the solution. Then, tiny seed crystals at the bottom are heated to supersaturation. Convection occurs due to the temperature difference between the top and bottom layers of the solution; the saturated solution at the bottom flows to the low-temperature region at the top. Thereafter, the

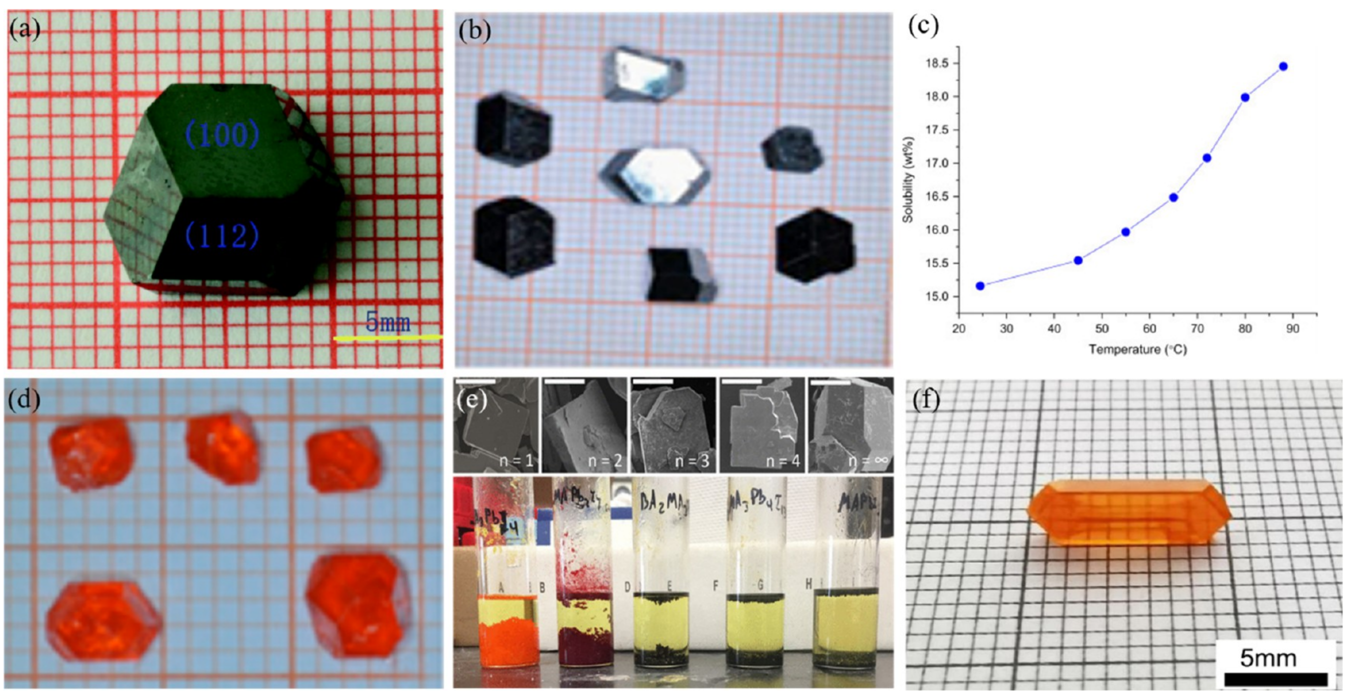

Figure 6. (a, b) $MAPbI_3$ SCs prepared by STL method. Reproduced from permission from ref 14. Copyright 2015, Royal Society of Chemistry. Reproduced with permission from ref 73. Copyright 2015, Elsevier. (c) Solubility curve of $MAPbI_3$ in HI (57 wt %) under different temperatures. Reproduced with permission.[73] Copyright 2015, Elsevier. (d) $MAPbBr_3$ SCs. Reproduced with permission from ref 73. Copyright 2015, Elsevier. (e) 2D SCs $(CH_3(CH_2)_3NH_3)_2(CH_3NH_3)_{n-1}Pb_nI_{3n+1}$ (n = 1, 2, 3, 4, ∞). Reproduced from permission from ref 10. Copyright 2016, American Chemical Society. (f) $CsPbBr_3$ single crystal. Reproduced with permission from ref 19. Copyright 2021, Springer Nature. reproduced without any modification and licensed under CC BY 4.0, https://creativecommons.org/licenses/by/4.0/.

https://doi.org/10.1021/acs.chemmater.2c03505
Chem. Mater. 2023, 35, 2683−2712

single crystals precipitate and attach to the top seed to produce high-quality large perovskite SCs, as shown in Figure 7a.[52]

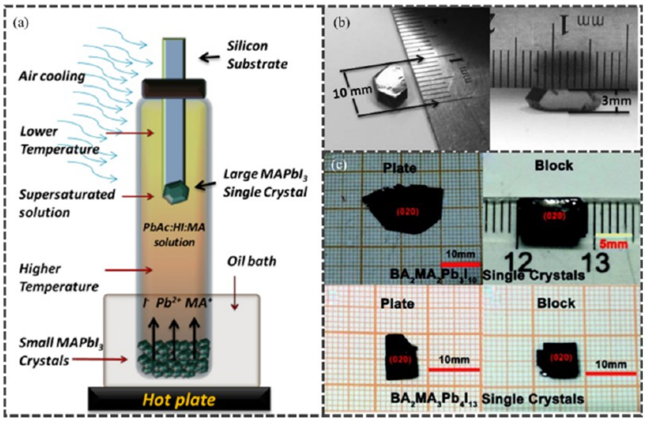

Figure 7. (a) Schematic illustrations of the growth of large size $MAPbI_3$ single crystal. Reproduced from permission from ref 52. Copyright 2016, Royal Society of Chemistry. (b) $MAPbI_3$ SCs by the TSSG method. Reproduced with permission from ref 22. Copyright 2015, American Association for the Advancement of Science. (c) Plate-shaped $BA_2MA_2Pb_3I_{10}$ and block-shaped $BA_2MA_3Pb_4I_{13}$ SCs. Reproduced from permission from ref 77. Copyright 2018, Royal Society of Chemistry.

Huang et al. synthesized high-quality $MAPbI_3$ crystals through the TSSG method. First, the seed crystals were precipitated from a mixed acid solution. Then, they were fixed at the bottom of the vial, where a Si substrate was inserted. Then, the substrate was cooled with air in the top half of the vial to remove the latent heat efficiently. This resulted in the formation of large seed crystals with low defect concentrations. The seed crystals were dissolved in an oil bath to form a supersaturated solution while maintaining the temperature of the vial. The inflow of outside air formed a temperature gradient between the top and bottom layers of the solution in the vial. The supersaturated solution at the bottom flowed to the top and nucleated on the low-temperature Si substrate to produce the bulk $MAPbI_3$ SCs. The resulting single crystals exhibited good quality; they can be left in the air for at least six months without losing their surface luster, as shown in Figure 7b.[22] In 2016, Tao et al. prepared bulk single crystals of $MASnI_3$ ($20 \times 16 \times 10$ mm^3) and $FASnI_3$ ($8 \times 6 \times 5$ mm^3) for the first time through the TSSG method under ambient atmosphere. The growth temperature was precisely controlled, and high-quality seed crystals were utilized. Furthermore, the changes in the solubility of these crystals in a $HI-H_3PO_2$ mixed solution were monitored; Figure 7c shows the corresponding solubility curves.[76] In addition to these single-crystal 3D perovskites, large 2D perovskite SCs, such as BA_2PbI_4, $BA_2MA_2Pb_3I_{10}$, and $BA_2MA_3Pb_4I_{13}$, could also be prepared through the TSSG route.[77]

The principles of crystallization in the BSSG method are similar to those involved in the TSSG route. In these methods, single seed crystals are precipitated through the cooling of the supersaturated solution.[78] However, the positions of single crystal seed growth and cooling regions in these two methods are reversed, as shown in Figure 8.

In 1995, Mitzi et al. reported the growth of $MASnI_3$ single crystal for the first time based on the cooling crystallization method. First, methylammonium iodide (MAI) and SnI_2 were

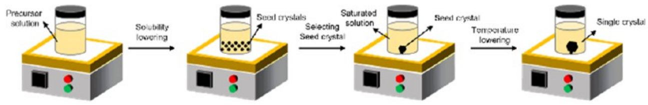

Figure 8. Schematic diagram of the BSSG method.

dissolved individually in HI acid. The resulting solutions were heated in a water bath at 90 °C and then mixed to obtain a clear yellow solution. The clear precursor solution was cooled down to room temperature to precipitate crystals seeds at the bottom of the vial.[48] In 2016, Tao et al. synthesized bulk $NH_3(CH_3)_3SnX_3$ (X = Cl^-, Br^-) SCs in an ambient atmosphere for the first time. The small seed crystals were deposited on the bottom of the substrate and then rotated using electric motors to avoid uneven crystallization due to the nonuniformity of the solution concentration. When the initial temperature was above 60 °C, aqueous HX (X = Cl^-, Br^-) evaporated, which increased the opacity of the $NH_3(CH_3)_3SnX_3$ (X = Cl^-, Br^-) SCs. Therefore, the controlled temperature range played a critical role in crystal growth. The seed crystals gradually grew through the attachment of the precipitated single crystals from the saturated solution. Finally, $NH(CH_3)_3SnCl_3$ ($13 \times 8 \times 6$ mm^3) and $NH(CH_3)_3SnBr_3$ ($8 \times 6 \times 4$ mm^3) SCs were synthesized with good atmospheric and thermal stability, shown in Figure 9a.[79] On the other hand, Sun et al. produced

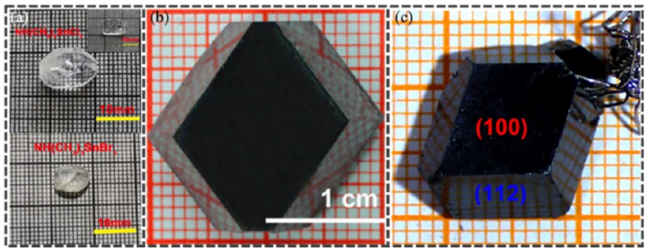

Figure 9. (a) $NH(CH_3)_3SnCl_3$ and $NH(CH_3)_3SnBr_3$ SCs. Reproduced from permission from ref 79. Copyright 2016, American Chemical Society. (b, c) $MAPbI_3$ SCs by the BSSG method. Reproduced with permission from refs 15, 17, and 42. Copyright 2015, Springer Nature. Reproduced without any modification and licensed under CC BY 4.0, https://creativecommons.org/licenses/by/4.0/. Reproduced from permission from ref 18. Copyright 2016, American Chemical Society.

bulk single-crystal $MAPbI_3$ through the BSSG method and reported that the introduction of Cl into the precursor solution could improve the crystalline quality of the perovskite and accelerate its growth rate. First, two separate solutions of $Pb(CH_3COO)_2$ and MAI−MACl mixture (1:1 ratio) in aqueous HI were prepared. Later, the two solutions were mixed to form the precursor (growth) solution and then rapidly cooled to produce the small $MAPbI_3$(Cl) seed crystals. High-quality seed crystals were selected and introduced into the growth solution. The temperature of the growth solution was controlled in an oil bath. First, the outer surface of the seed crystals was melted at 105 °C and then cooled down to 40 °C over 5 days; the seed crystals grew slowly. The dimensions of the synthesized bulk single crystal were $20 \times 18 \times 6$ mm^3, as shown in Figure 9b.[18] Large $MAPbI_3$ SCs were also produced through the BSSG method. First, black single crystals with a lateral size of approximately 3 mm were prepared and then fixed at the end of a Pt wire at the bottom of the perovskite

https://doi.org/10.1021/acs.chemmater.2c03505
Chem. Mater. 2023, 35, 2683−2712

growth solution. The outer surface of the seed crystals was dissolved at 100 °C for 10 min. Then, these were rapidly cooled down to 82 °C to produce high-quality seed crystals. Finally, slow cooling was performed to produce the bulk $MAPbI_3$ SCs with dimensions of 12 × 12 × 7 mm^3, as shown in Figure 9c. Throughout the precipitation of the single crystals, some precipitates developed at the bottom of the flask and stuck preferentially to the surface of the growing seeds during the cooling phase, significantly inhibiting the single crystals growth. As a result, Pt wire was used to support the seed crystals from touching the bottom of the vial.[15]

In the procedures indicated above, perovskite SCs were created in the liquid phase after the precursor perovskite materials were first dissolved at high temperatures. Tiny perovskite seed crystals were produced after cooling down the precursor solution. Then, they were fixed in another vial containing saturated solutions. Finally, bulk single crystals are synthesized through a precisely controlled cooling process. During the synthesis of $MAPbI_3$, yellow needle-like $(MA)_4PbI_6{\cdot}2H_2O$ crystals may form in the solution when the temperature drops to approximately 40 °C; the formation of such crystals affects the slow growth of the seed crystals.[80] In addition, if the cooling rate is too high, multiple nuclei may be produced, which hinders the single crystals growth. In contrast, the synthesis process becomes time-consuming and inefficient if the cooling rate is too low.

3.3. Inverse Temperature Crystallization (ITC) Method. In general, the solubility of the solute in the precursor solution increases with increasing temperature. However, in 2013, Bakr et al. observed the contrary; the solubility of some perovskite materials in specific organic solutions decreased with increasing temperature. Considering this retrograde solubility of materials, a new technique to grow perovskite SCs, inverse temperature crystallization (ITC), was proposed. In this method, γ-butyrolactone (GBL), *N*,*N*-dimethylformamide (DMF), and dimethyl sulfoxide (DMSO) are commonly used as solvents for the preparation of organic hybrid perovskite SCs with highly tunable sizes and shapes, as shown in Figure 10.[81]

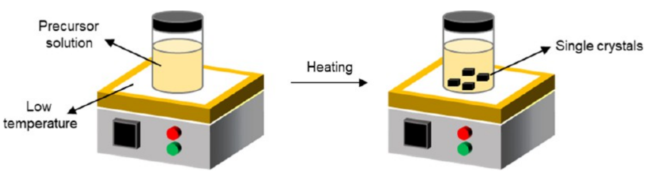

Figure 10. Schematic diagram of the ITC method. Reproduced from permission from ref 81. Copyright 2016, Royal Society of Chemistry.

In 2015, Bakr et al. successfully synthesized $MAPbX_3$ (X = Br^-, I^-) perovskite SCs through ITC. The solubility of $MAPbI_3$ in GBL and $MAPbBr_3$ in DMF decreased as the temperature increased. Different solvents had varying effects on the coordination of the Pb−I bonds in the precursors. For example, the strong bonding of DMSO had a strong bonding interaction with the $MAPbI_3$ precursors, which slowed down the crystallization process, i.e., the solvent and the temperature employed are critical to prepare high-quality single crystals. $MAPbI_3$ crystals did not precipitate when DMF and DMSO solvents were used. Similarly, GBL was not used to synthesize $MAPbBr_3$ because of this solvent's low solubility of the perovskite precursors. Snith et al. also reported about the mechanism of crystal growth in ITC, that in the precursor solution the breaking up of colloids and the change in the solvent strength could lead to supersaturation and subsequent crystallization.[82]

In addition to the solvent, the growth temperature also plays a substantial role in the growth process. For example, the bromide solution can be prepared at room temperature, whereas the iodide solution needs to be heated to 60 °C. Figure 11a shows the corresponding SCs.[49]

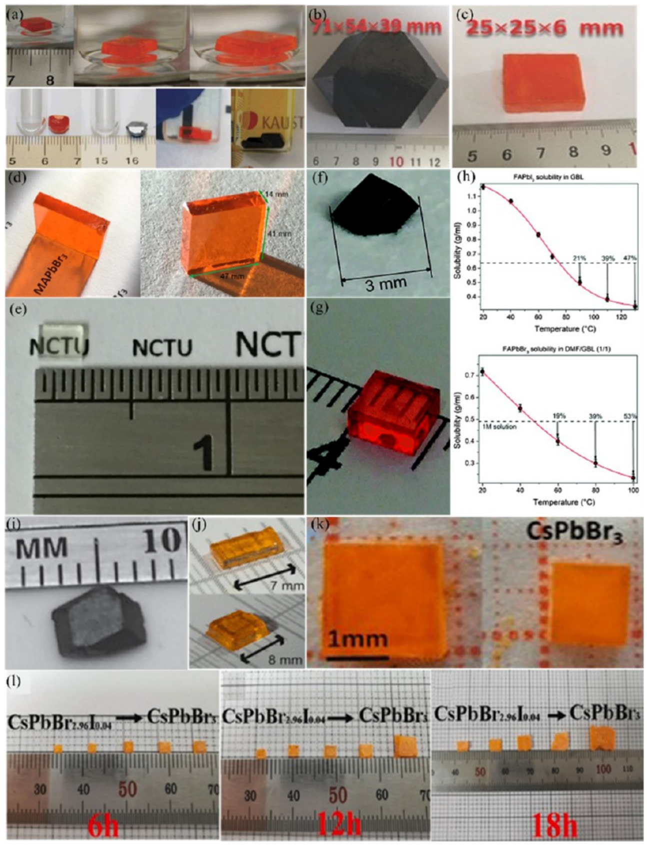

Figure 11. (a) $MAPbBr_3$ and $MAPbI_3$ SCs by the ITC method. Reproduced with permission from ref 49. Copyright 2015, Springer Nature, reproduced without any modification and licensed under CC BY 4.0, https://creativecommons.org/licenses/by/4.0/. (b) $MAPbI_3$ single crystal. Reproduced with permission from ref 84. Copyright 2015, Wiley-VCH. (c, d) $MAPbBr_3$ SCs. Reproduced with permission from ref 84. Copyright 2015, Wiley-VCH. Reproduced with permission from ref 65. Copyright 2019, Elsevier. (e) $MAPbCl_3$ SCs. Reproduced with permission from ref 85. Copyright 2019, Springer Nature, reproduced without any modification and licensed under CC BY 4.0, https://creativecommons.org/licenses/by/4.0/. (f) $FAPbI_3$ single crystal. Reproduced from permission from ref 81. Copyright 2016, Royal Society of Chemistry. (g) $FAPbBr_3$ single crystal. Reproduced from permission from ref 81. Copyright 2016, Royal Society of Chemistry. (h) Temperature-dependent solubility of $FAPbI_3$ in GBL and $FAPbBr_3$ in DMF:GBL (1:1 v/v). Reproduced from permission from ref 81. Copyright 2016, Royal Society of Chemistry. (i) α-Phase $FAPbI_3$ single crystal. Reproduced with permission from ref 86. Copyright 2016, Wiley-VCH. (j, k) $CsPbBr_3$ SCs. Reproduced from permission from ref 88. Copyright 2016, American Chemical Society. Reproduced from permission from refs 88 and 90. Copyright 2021, American Chemical Society. (l) Morphology of $CsPbBr_xI_{(3-x)}$ SCs under same time for growing.[91] Reproduced with permission from ref 91. Copyright 2020, Elsevier.

https://doi.org/10.1021/acs.chemmater.2c03505
Chem. Mater. 2023, 35, 2683−2712

Relative to the STL, TSSG, and BSSG methods, high-quality single crystals can be produced in shorter preparation times through ITC. Wang et al. precisely controlled the solution temperature from 60 to 80 °C to prepare $MAPbBr_3$ SCs in DMF. The seed crystals' slow nucleation and rapid growth were simultaneously achieved in this temperature range. The dimensions of the synthesized single crystal were 6 × 4 × 1.5 mm^3, which is sufficient for the preparation of optoelectronic devices.[83] Liu et al. also used this method to grow bulk $MAPbX_3$ (X = Cl^-, Br^-, I^-) SCs. For the synthesis of $MAPbI_3$ SCs, seed crystals with a lateral size of 1−2 mm were selected. As shown in Figure 11b, large single crystals with dimensions of 71 × 54 × 39 mm^3 were produced through ITC. From the XRD pattern of the $MAPbI_3$ SCs, the full width at half-maximum of the (200) plane was 0.3718°, further confirming the high degree of crystallinity of these large single crystals. In addition, $MAPbBr_3$ single crystal (25 × 25 × 6 mm^3) can also be synthesized as shown in Figure 11c.[84]

ITC was further improved by precisely controlling the temperature and solubility of the solute in the growth solution. This refined technique is referred to as low-temperature gradient crystallization. This method synthesized MAPbBr3 single crystal with dimensions of 47 × 41 × 14 mm^3, as shown in Figure 11d. The $MAPbBr_3$ SCs exhibited high carrier mobility, long carrier lifetime, and ultralow defect density of states equal to 81 ± 5 $cm^2\ V^{-1}s^{-1}$, 899 ± 127 ns, and 6.2 ± 2.7 × $10^9\ cm^{-3}$, respectively.[65] These excellent properties render large $MAPbX_3$ (X = Br^-, I^-) crystals as promising materials for high-performance optoelectronic devices. Using GBL, Xie et al. integrated ITC and TSSG methods to produce high-quality MAPbX3 (X = Br−, I−) crystals. First, the precursor materials were added and then dissolved in the GBL solvent through an initial heating process. The precursor solution was further heated to precipitate the small crystals. Then, high-quality crystals were selected and fixed on the substrate in the saturated solution. This was gradually cooled down to produce the large single crystals.[16] In addition to Br^- and I^- based perovskite SCs, Sun et al. successfully synthesized $MAPbCl_3$ crystals (2.5 × 2 × 1 mm^3) for the first time through low-temperature gradient crystallization. MACl and $PbCl_2$ were dissolved in a 1:1 DMF−DMSO solution under continuous stirring until a clear solution was obtained. The temperature was increased to 50 °C for 6−8 h to facilitate the precipitation of the single crystals, as shown in Figure 11e.[16,85]

Through a similar method, Bakr et al. pioneered the synthesis of $FAPbX_3$ (X = Br^-, I^-) SCs in 2013. $FAPbI_3$ was produced at 115 °C using GBL, whereas $FAPbBr_3$ was synthesized at 55 °C in a DMF−GBL (1:1 v/v) mixed solvent, as shown in Figure 11f and g. In addition, the temperature-dependent solubilities of $FAPbI_3$ and $FAPbBr_3$ in their corresponding solvents were also studied, as shown in Figure 11h.[81] Yang et al. grew $FAPbI_3$ SCs through an integrated STL−ITC method. First, the seed crystals of $FAPbI_3$ were produced through the STL method. The selected seed crystals were placed in a saturated solution at 100−105 °C for 3 h to avoid large temperature fluctuations. This led to the formation of high-quality $FAPbI_3$ crystals with a lateral size greater than 4 mm, as shown in Figure 11i.[81,86] Kuang et al. synthesized mixed-organic perovskite $MA_{0.45}FA_{0.55}PbI_3$ SCs in GBL. First, a precursor solution of $MA_{0.45}FA_{0.55}PbI_3$ was prepared at 60 °C and then kept at 160 °C for 30 min to obtain 0.5−1 mm seed crystals. Next, the seed crystals were moved into a fresh, saturated solution at 110−125 °C for 3 h to synthesize the bulk single crystals.[87]

Apart from organic halide perovskite SCs, Kovalenko et al. used a mixed solution of cyclohexanol, DMF, and DMSO to grow all-inorganic perovskite $CsPbBr_3$ crystals in 2016. The precursor solution temperature was utilized to determine the number of nuclei formed. One to three nuclei appear when the precursor solution temperature is fixed at 90 °C. However, no nuclei were formed at a higher temperature (110 °C). As shown in Figure 11j, the $CsPbBr_3$ crystals exhibited prismatic shapes with lateral sizes of over 7 mm.[88] In 2017, Bakr et al. also found that the CsBr/$PbBr_2$ ratio and solution temperature significantly impacted the perovskite synthesized in DMSO. A CsBr/$PbBr_2$ molar ratio of 1:2 led to the formation of high-purity $CsPbBr_3$ without $CsPb_2Br_5$ and Cs_4PbBr_6 byproducts at 120 °C.[89] Li et al. varied the mixture of the organic solvents employed using DMSO and small amounts of GBL and DMF, which can also effectively avoid the appearance of other phases, such as Cs_4PbBr_6 and $CsPb_2Br_5$, during the growth of the $CsPbBr_3$ crystals. The large $CsPbBr_3$ SCs were obtained by increasing and maintaining the temperature, as shown in Figure 11k.[90]

In 2020, Wang et al. successfully introduced I^- ions into $CsPbBr_3$ to obtain $CsPbBr_xI_{(3\text{-}x)}$ SCs through a growth process similar to that described above. After the $CsPbBr_xI_{(3\text{-}x)}$ crystals were produced, they were immediately collected and washed using a DMF solution to prevent the abrupt temperature decrease. Sudden temperature reductions could lead to the attachment of a small amount of the solution to the crystal surface, thereby dissolving some of the crystals and destroying the integrity of the products. In this process, the growth of the single crystals at the same temperature became difficult. On the other hand, the required growth time, thermal stability, and purity of the $CsPbBr_xI_{(3\text{-}x)}$ single crystals increased with increasing I^- ion concentration, as shown in Figure 11l.[91]

3.4. Slow Evaporation Crystallization (SEC) Method. In addition to lowering the solubility of the solute by lowering the temperature of the precursor solution, saturation can also be achieved by slowly evaporating the solvent. Slow evaporation crystallization (SEC) is a simple and traditional method for producing single crystals. To saturate the solution more quickly, it is often heated so that the solvent evaporates faster. In this method, heating only plays a secondary role in the growth process. The main driver for crystal growth is the evaporation of the solvent. Therefore, the evaporation rate of the precursor solution must be precisely controlled to ensure the supersaturation of the solution at a specific temperature, as shown in Figure 12.

In 2005, Mercier reported that SEC could be used to grow 2D perovskite SCs by dissolving $HO_2C(CH_2)_3NH_3$, CH_3NH_3, and PbI_2 in HI acid and then slowly evaporating the solvent at room temperature under an Ar atmosphere to avoid the

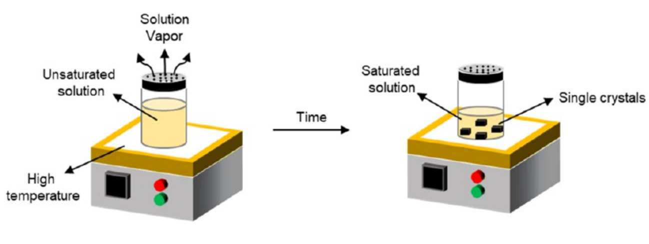

Figure 12. Schematic illustration of the SEC method.

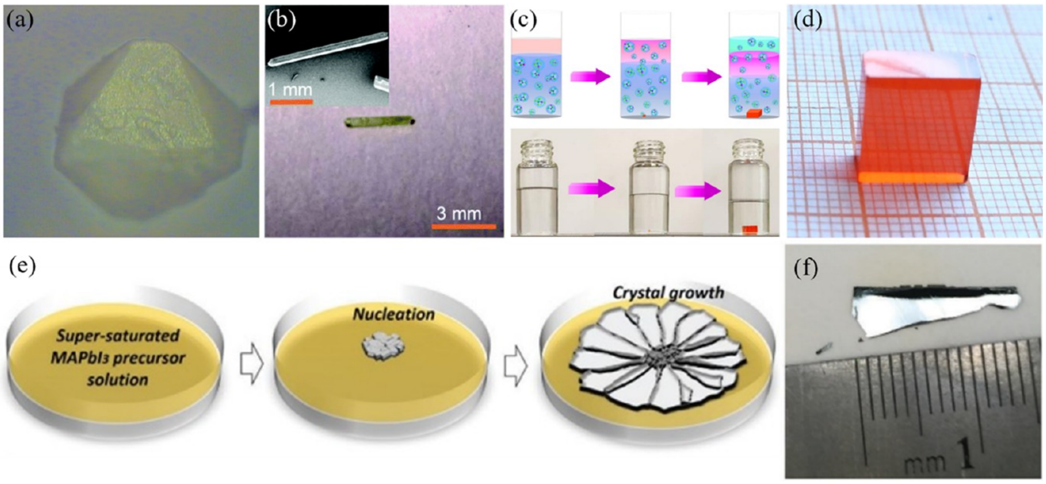

Figure 13. (a) $[TMA]_2SnBr_6$ single crystal. Reproduced with permission from ref 93. Copyright 2019, Elsevier. (b) FA-(N-MPDA)$PbBr_4$ perovskite SCs. Reproduced from permission from ref 95. Copyright 2020, Royal Society of Chemistry. (c) Schematic illustration of the growth of $MAPbBr_3$ SCs. Reproduced with permission from ref 96. Copyright 2020, Springer Nature, reproduced without any modification and licensed under CC BY 4.0, https://creativecommons.org/licenses/by/4.0/. (d) $MAPbBr_3$ SCs. Reproduced with permission from ref 96. Copyright 2020, Springer Nature, reproduced without any modification and licensed under CC BY 4.0, https://creativecommons.org/licenses/by/4.0/. (e) Schematic illustration of the growth of $MAPbI_3$ SCs. Reproduced with permission from ref 97. Copyright 2019, Wiley-VCH. (f) $MAPbI_3$ single crystal wafers. Reproduced with permission from ref 97. Copyright 2019, Wiley-VCH.

reduction of I^- ions to I_2. Red 2D $(HO_2C$-$(CH_2)_3NH_3)_2(CH_3NH_3)Pb_2I_7$ and orange needle-like $(HO_2C$-$(CH_2)_3NH_3)PbI_4$ SCs were successfully synthesized.[92] Bulou et al. prepared Sn-based SCs of $[TMA]_2SnBr_6$ (TMA= tetramethylammonium = $N(CH_3)_4$) through SEC, as shown in Figure 13a. The Sn-based SCs were grown through the slow evaporation of the solution at room temperature for several days.[93] 2D Ge-based perovskite SCs, such as $MAGeI_3$, $FAGeI_3$, $C(NH_2)_3GeI_3$, $(CH_3)_3NHGeI_3$, and $(CH_3)_2C(H)NH_3GeI$, can also be obtained through this method. A series of crystals eventually precipitates by evaporating the solvent to reduce the volume of the solution and decreasing the temperature to lower the solubility of the solute.[94] In addition, the successful synthesis of 2D single-crystal ACI perovskites, FA-(*N*-MPDA)$PbBr_4$, through SCE was also reported. *N*-methylpropane-1,3-diammonium (*N*-MPDA) was used as the organic long-chain diammonium spacer for the FA^+-filled perovskite cages to produce the stable 2D layered FA-(*N*-MPDA)$PbBr_4$ SCs, as shown in Figure 13b.

Initially, a saturated precursor solution was prepared and then slowly evaporated to facilitate the spontaneous crystallization of the seed crystals. The seed materials were allowed to grow into large crystals over 1 d. Under illumination for over 2 h, a perovskite random laser prepared using the synthesized single crystal showed a constant lasing emission without degradation, which revealed the stability of the 2D single-crystal ACI perovskite.[95] Recently, Fang et al. optimized the SCE method by using Si oil as the separation medium for the evaporation of the solvent. The density of Si oil is slightly higher than that of the solvent and lower than that of the perovskite precursor solution. The solvent diffused into the Si oil and then escaped, thereby forming a lower layer of supersaturated solution.

Single crystals precipitated as the solvent continued to escape, whereas the precursor solution remained at saturation, resulting in large crystals' growth, as shown in Figure 13c. The carrier lifetime and defect density of the $MAPbBr_3$ SCs grown through this optimized SCE method were 1 μs and 4.4×10^9 cm^{-3}, respectively, As shown in Figure 13d.[96] As the reduction of the surface tension is the driving force for crystal growth during solvent evaporation, the crystals preferentially nucleate and grow further at the vapor−liquid interface. As shown in Figure 13e and f, Huang et al. produced $MAPbI_3$ wafers with a lateral size of 1−1.5 cm within 30 min by maintaining the solution temperature at 90 °C, controlling the solvent evaporation rate, and obtaining the nucleation at the center area of the gas−liquid interface rapidly.[97]

Although SCE method is highly effective and practical, the shape of the resulting crystals produced through this technique is often difficult to control, which limits the application of the product in optoelectronic devices. However, SCE is commonly used with the STL method, where seed crystals are precipitated first by lowering the solution temperature. Then, the seeds are placed in a precursor solution and continuously evaporated to reach supersaturation, producing high-quality large single crystals with highly tunable shapes.

3.5. Antisolvent Vapor-Assisted Crystallization (AVC) Method. The antisolvent vapor-assisted crystallization method (AVC) takes advantage of the solubility difference of perovskites in two miscible solvents. The solvent in the system is the liquid in which the solute is soluble. In contrast, the other solvent, in which the solute is insoluble, is referred to as the antisolvent in the solvent−solute system. When the volatile antisolvent gradually diffuses into the precursor solution, it slowly reduces the solubility of the solvent; consequently, the solute precipitates. This method provides a new route for preparing high-quality single crystals with higher carrier mobilities and longer carrier lifetimes, as shown in Figure 14.

In 2015, Bakr et al. synthesized high-quality $MAPbX_3$ (X = Br^-, I^-) through AVC. First, MAX and PbX_2 were dissolved in DMF or GBL. Then, a dichloromethane (DCM) antisolvent was slowly introduced into the precursor solution. The prepared single crystals, Figure 15a and b, exhibited excellent properties, such as lower trap state density and higher carrier mobility than those of polycrystalline Si.[23] Through the same method, Lio et al. grew $MAPbBr_3$ SCs. Initially, a $MAPbBr_3$

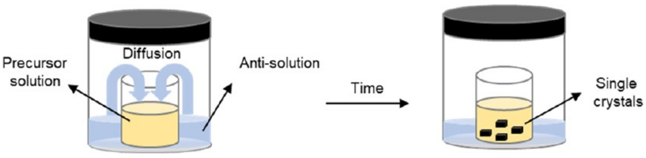

Figure 14. Schematic illustration of the AVC method.

precursor solution in DMF was prepared in a small tube, which was sealed using an Al foil with small holes to allow the diffusion of the DCM antisolvent. The precipitation of the $MAPbBr_3$ SCs was performed slowly. The size of the products reached a few millimeters after a few days, as shown in Figure 15c.[43] Kirmayer et al. grew single crystals of $MAPbBr_3$ and $MAPbI_3$ using isopropanol as an antisolvent. The addition of $PbCl_2$ nanocrystals had a remarkable effect on the growth processes of these single crystals. These nanocrystals acted as heterogeneous nucleation sites that facilitated the growth of the perovskite crystals in the solution. Increasing the $PbCl_2$ concentration improved the growth rate and led to the formation of more crystals with smaller particle sizes.[98] Xu et al. also used DCM as an antisolvent to synthesize $MAPbBr_3$. By controlling the dropwise addition of DCM, the dimensions of the crystals changed from $2 \times 2 \times 1$ mm^3 to $15 \times 15 \times 5$ mm^3. The resistivity of the grown bulk $MAPbBr_3$ SCs was 5.6×10^8 Ω cm. The mobility lifetime (τs) of the electrons and holes were 2.2×10^{-4} and 4.2×10^{-4} cm^2 V^{-1}, respectively.[99] Aside from DCM, toluene could also be used as an antisolvent to produce orange layered $MAPbBr_3$ SCs in a DMF solvent, as shown in Figure 15d.[100] In addition to selecting different antisolvents for AVC, Huang et al. regulated the ratio of $PbBr_2$ and MABr in the DMF solvent to produce $MAPbBr_3$ SCs, which were used to prepare a highly sensitive X-ray detector.

$PbBr_2$ has lower solubility than MABr in DMF. When DCM was diffused into the precursor solution, $PbBr_2$ preferentially precipitated rather than MABr. As a result, nonequilibrium opaque crystals were accumulated. To produce clear and high-quality $MAPbBr_3$ SCs, the $PbBr_2$/MABr molar ratio in DMF should be 0.8, as shown in Figure 15e. X-ray detectors were prepared from the grown $MAPbBr_3$ crystals by reducing the bulk defects and passivating the surface traps. The detector exhibited a record-high mobility lifetime of 1.2×10^{-2} cm^2 V^{-1} and an extremely low surface charge recombination velocity of 64 cm s^{-1}.[37] Tarasov et al. optimized AVC and proposed a solvent-conversion-induced rapid crystallization (SCIRC) technique. In this approach, two solvents (S1, S2) that react slowly and irreversibly are selected. When mixed, S1 and S2 should be able to dissolve the target substance (A). However, the product (P) of the intersolvent reaction, S1 + S2 → P, should not dissolve A. Due to the chemical conversion of the good solvent mixture (S1 + S2) to the poor solvent P, the

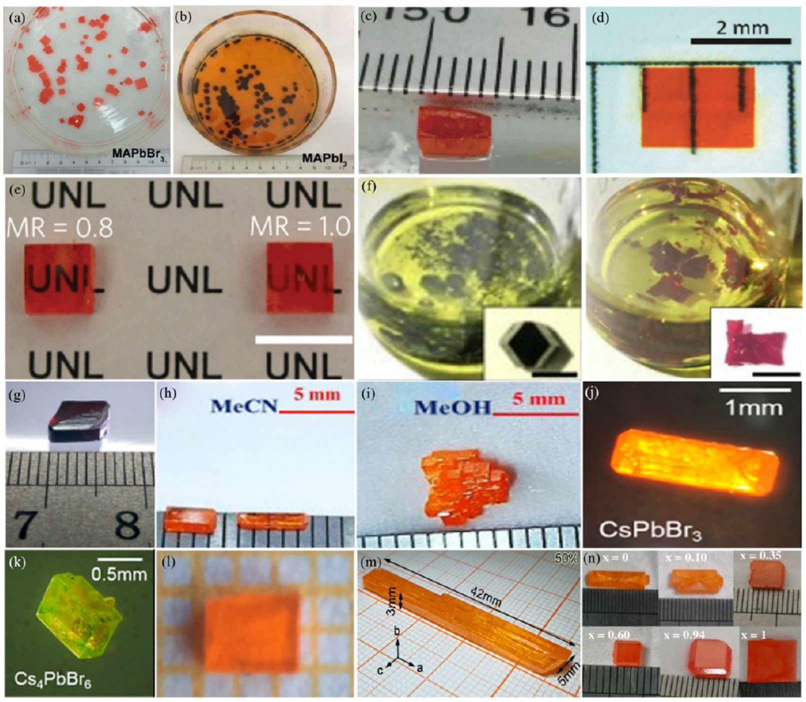

Figure 15. (a) $MAPbBr_3$ SCs. Reproduced with permission from ref 23. Copyright 2015, American Association for the Advancement of Science. (b) $MAPbI_3$ SCs. Reproduced with permission from ref 23. Copyright 2015, American Association for the Advancement of Science. (c−e) $MAPbBr_3$ SCs under different growth environments. Reproduced with permission from ref 37. Copyright 2016, Springer Nature. Reproduced with permission from ref 43. Copyright 2016, American Association for the Advancement of Science, reproduced without any modification and licensed under CC BY 4.0, https://creativecommons.org/licenses/by/4.0/. Reproduced with permission from refs 37, 43, and 100. Copyright 2016, Wiley-VCH. (f) $MAPbI_3$ SCs and $BA_2MAPb_2I_7$ SCs. Reproduced from permission from ref 101. Copyright 2020, American Chemical Society. (g) $(NH_4)_3Sb_2I_9$ single crystal. Reproduced from permission from ref 102. Copyright 2017, Wiley-VCH. (h−j) $CsPbBr_3$ SCs. Reproduced from permission from ref 51. Copyright 2016, American Chemical Society. Reproduced from permission from refs 51 and 103. Copyright 2016, American Chemical Society. (k) Cs_4PbBr_6 SCs. Reproduced from permission from ref 51. Copyright 2016, American Chemical Society. (l, m) $CsPbBr_3$ SCs. Reproduced from permission from ref 35. Copyright 2017, American Chemical Society. Reproduced from permission from refs 35 and 104. Copyright 2017, American Chemical Society. (n) $MA_xCs_{1-x}PbBr_3$ SCs by increasing the content of MA. Reproduced with permission from ref 36. Copyright 2020, Wiley-VCH.

solution becomes supersaturated, and the solute gradually crystallizes. In the work of Tarasov et al., ethylene carbonate (EC) or propylene carbonate (PC) was used as S1, whereas aqueous HI (57 wt %) was chosen as S2. The products formed using EC and PC were ethylene glycol and propylene glycol, respectively. The humidity and temperature throughout the experiment were controlled at 30−55% and 23−25 °C, respectively. $MAPbI_3$ SCs were grown using the solvent mixture of EC or PC with concentrated aqueous HI. A mixture of MAI and PbI_2 (1:1 ratio) powders was placed in a vial. Then, precursor solutions were prepared with an initial concentration that is 1−2% below the saturation concentration at a given T and ω_0 (the content of H_2O in the solvent). The precursor solution was vigorously stirred at 30−60 °C. The temperature was held constant throughout the crystallization process. After the solutes were completely dissolved in the solvent, the homogeneous solution was filtered and poured into a clean, flat-bottomed vial. Small holes were left at the top of the vial to facilitate the release of CO_2 formed during the hydrolysis reaction. The vial was then maintained at the same temperature to allow the growth of crystals. Finally, $MAPbI_3$ SCs were obtained and washed with dry ether. Additionally, $FA_xMA_{(1-x)}PbI_3$, $MAPb(Br_yI_{(1-y)})_3$, and $FA_xMA_{(1-x)}Pb(Br_yI_{(1-y)})_3$ SCs can also be grown through SCIRC. Meanwhile, 2D perovskite $(BA)_2(MA)Pb_2I_7$ SCs can also be synthesized using a slightly unsaturated solution based on an acidified $PC-H_2O$ mixture, as shown in Figure 15f. The desired number of layers (n) of the perovskite corresponded to the BAI/MAI/PbI_2 molar ratio.[101] As shown in Figure 15g,[102] apart from the products mentioned above, Pb-free perovskite SCs, such as $(NH_4)_3Sb_2I_9$, could also be successfully prepared using anhydrous ethanol (EtOH) and chloroform as the solvent and antisolvent, respectively.

All-inorganic perovskite single crystals can also be synthesized through the AVC method. In the work of Hodes et al., CsBr and $PbBr_2$ were dissolved in a 1:1 ratio in DMSO at 50 °C under constant stirring. Then, the precursor solution was cooled down to room temperature. Methyl cyanide (MeCN) and methanol (MeOH) were added dropwise into the original DMSO solution. When the MeCN/DMSO ratio = 1:1 and MeOH/DMSO ratio = 0.55:1, orange-yellow precipitates formed in the solution, which was then sealed and stirred for 24 h at 50 °C. After stirring, the solution was filtered to produce a saturated solution containing the grown crystals. Two growth processes were employed; however, the solubility of the solute was reduced by increasing the amount of the antisolvent in the precursor solution, which facilitated the rapid precipitation of the $CsPbBr_3$ crystals. The morphologies of the crystals produced using MeCN and MeOH antisolvents were different, as shown in Figure 15h and i. In the first case, MeCN and MeOH were used to grow the single crystals by heating the confined space under an antisolvent atmosphere, which gradually diffused into the precursor solution.

In the second case, the previously prepared precursor solution was heated to the desired temperature by taking advantage of the special properties of the antisolvent and of the grown crystals. Then, either MeCN or MeOH was added. After heating, an inverse gradient of soluble compounds that contain products other than $CsPbBr_3$ was formed. The unwanted product, Cs_4PbBr_6, was eliminated through a two-step heating cycle method. First, the solution was heated to the desired temperature for 4 h, which formed a mixed precipitate. Then, it was cooled down to room temperature under continuous stirring. After all the orange precipitate had dissolved, a mixture of Cs_4PbBr_6 and an unknown white precipitate was still present at the bottom of the flask. The solution was then filtered and transferred to a new vial. Second, the solution was heated to the same temperature as that in the first stage. No other reverse soluble compounds were formed during this heating cycle. As such, high-quality orange $CsPbBr_3$ crystals were produced.[103] Jung et al. grew $CsPbBr_3$ and Cs_4PbBr_6 SCs through similar methods. To prepare the $CsPbBr_3$ SCs, CsBr and $PbBr_2$ were dissolved in DMSO under sonication. After the dissolution was complete, the homogeneous mixture was filtered to obtain the precursor solution. The antisolution diffusion components and processes employed in the work of Jung et al. were similar to those utilized in the study of Bakr.[23] When the growth was complete, the crystals were collected from the solution and washed with DMF and DCM to remove the excess $PbBr_2$. On the other hand, Cs_4PbBr_6 SCs were prepared using a CsBr/$PbBr_2$ mixture with a molar ratio of 4 in DMSO. A small amount of HBr was added to the solution after the complete dissolution of the solutes to ensure that excess Br^- ions were supplied to the system. The crystals grew gradually through the antisolution diffusion process and then were collected through the same route as that of separating the CsPbBr3 crystals from the solution as shown in Figure 15j and k.[51]

Zhan et al. synthesized $CsPbBr_3$ SCs. In their work, MeOH was added dropwise to a saturated solution of $CsPbBr_3$ in DMSO until the yellow-white precipitates disappeared. Then, filtration was performed to obtain the growth solution. MeOH and EtOH were used as antisolvents to maintain the atmosphere and temperature of the solution during crystal growth, thereby forming high-quality $CsPbBr_3$ SCs, as shown in Figure 15l. The performance of the photodetector prepared using the (101) plane of the $CsPbBr_3$ SCs was considerably better than those of the polycrystalline film-based devices.[35]

Jie et al. produced different perovskite crystals, such as $CsPbBr_3$, $CsPb_2Br_5$, and Cs_4PbBr_6, by varying the $PbBr_2$/CsBr molar ratio in the precursor solution; $CsPbBr_3$ crystals were formed when the $PbBr_2$/CsBr molar ratio was in the range of 1−1.5. Furthermore, large $CsPbBr_3$ SCs with dimensions of 42 × 5 × 3 mm^3 were synthesized using a 1:1 mixture of MeOH and DMSO, as shown in Figure 15m. The $CsPbBr_3$ SCs exhibited satisfactory photo responses and had a high band gap and resistivity equal to 2.29 eV and 2.1 × 10^9 Ω cm, respectively.[104] On the other hand, Liao et al. grew organic−inorganic hybrid perovskite SCs ($MA_xCs_{1-x}PbBr_3$) through AVC using $MAPbBr_3$ in DMF (0.15 M) and $CsPbBr_3$ in DMSO (0.4 M) precursor solutions. The precursor solutions were mixed according to the required proportion between Cs^+ and MA^+ cations. Then, the homogeneous mixtures were placed in a confined system at 30 °C with an $EtOH-H_2O$ mixture (1:3 ratio). The growth process was performed for approximately 14 d. The crystals were collected, washed twice with ether, and then dried in a vacuum oven. The band gap of the crystals decreased from 2.25 to 2.16 eV as the concentration of the MA^+ ions in the precursor was increased, as shown in Figure 15n. High-sensitivity X-ray detectors have been developed based on mixed-cation crystals due to their excellent optoelectronic properties. A detector based on $MA_{0.6}Cs_{0.4}PbBr_3$ registered a sensitivity of 2017 μC Gy_{air}^{-1} cm^{-2}. Furthermore, the detector limit at an applied voltage of 1 V was 1.2 μ Gy_{air} s^{-1}. The efficiency of the mixed-metal cation-

https://doi.org/10.1021/acs.chemmater.2c03505
Chem. Mater. 2023, 35, 2683−2712

based detector exceeded those of $MAPbBr_3$- and $CsPbBr_3$-based devices.[36]

In the AVC method, selecting the appropriate solvent and antisolvent is critical for synthesizing and growing different perovskite SCs. Moreover, the rate of the antisolvent evaporation should be controlled to tune the rate of crystal growth and, in turn, to produce high-quality perovskite SCs. However, since the crystal growth processes occur spontaneously at room temperatures, longer periods relative to those needed in the STL and ITC methods are required to obtain large single crystals through AVC.

4. PEROVSKITE CRYSTALLIZATION FROM VAPOR PHASE

4.1. Chemical Vapor Deposition (CVD) Method. The crystal structures of organic hybrid halide perovskites are very complex, and their morphology must be controlled down to a single atomic layer. Chemical vapor deposition (CVD) is a promising method for synthesizing these hybrid perovskites.[105] The reaction temperature employed in CVD is higher than those utilized in other crystal growth methods to reduce the substability and defects, such as grain boundaries, in the metal halides and to achieve a good lattice match between the perovskite and substrate.

Zhu et al. varied the deposition rate of the precursor materials during the synthesis of 3D films of mixed halide perovskite SCs; the ratio between the deposition rates of MAI and $PbCl_2$ was approximately 10:1. On the other hand, the deposition rate ratio was approximately 4:1 during the synthesis of the pure iodine perovskite. After the deposition process, the films were annealed at 100 °C for 40 min under nitrogen atmosphere to remove the excess organic cations and promote further crystallization.[106] Shin et al. grew a pattern of single-crystal $MAPbI_3$ thin films on Si or SiO_2 substrates through CVD; Figure 16a illustrates the growth process employed.[107] Liu et al. modified CVD to synthesize single-crystal $MAPbI_3$ nanosheets with controllable sizes. Therein, CVD was divided into two steps. First, PbI_2 nanosheets were physically deposited onto a substrate, which was then placed in an Ar environment. The ambient temperature and reaction time were set based on the gas pressure, which increased with decreasing temperature. Second, the MAI powder was placed in an appropriate position and then heated to produce the $MAPbI_3$ nanosheets on the substrate. Figure 16b shows the scheme of the nanoplatelets synthesis process. Additionally, the temperature of the substrate affected the deposition rate; higher temperature resulted in faster material deposition and formed larger nanosheets, as shown in Figure 16c. On the other hand, increasing the deposition time also increased the nanosheet size.[108] Duan et al. and Yu et al. performed CVD at different temperatures using different $CsPbX_3$ precursor powders (550 °C for $CsPbI_3$, 600 °C for $CsPbBr_3$, 650 °C for $CsPbCl_3$). In these works, the cooled reactant vapor could be nucleated on top of the substrate and grown as single crystal microplates, as shown in Figure 16d.[109,110] Yang et al. synthesized high-quality single-crystal $CsPbBr_3$ microstructures, such as microwires and microplates, through CVD. The $CsBr/PbBr_2$ molar ratio was set to 2:1, and the precursor mixture was heated to 560−580 °C in an Ar atmosphere for 18 min. Different microstructures were synthesized by varying the reaction temperature; after 60 min of deposition, $CsPbBr_3$ microwires were grown at 380 °C, whereas microplates and triangular pyramids were obtained at 340 and 300 °C, respectively. Figure 16e shows research progress in one-step experimental synthesis of microstructures and the corresponding morphology of the products.[111] Apart from the above CVD methods, in low-temperature *in situ* dynamic thermal crystallization, the crystal grain size and the compactness of perovskite films can be easily tuned during the thermal coevaporation process.[112]

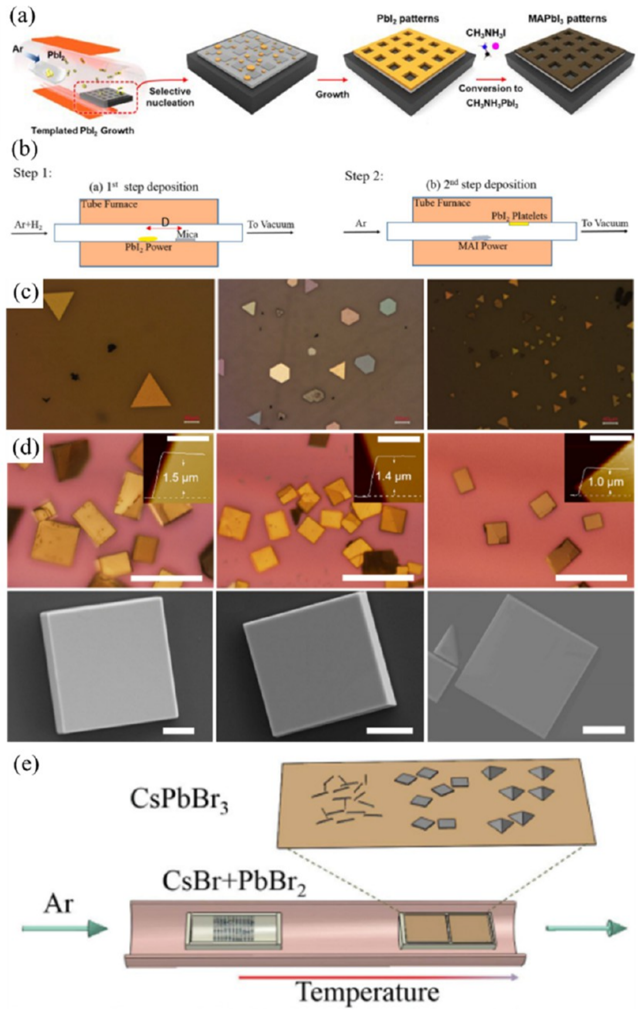

Figure 16. (a) Schematic illustration of growing $MAPbI_3$ single crystal thin films. Reproduced from permission from ref 107. Copyright 2019, American Chemical Society. (b) Schematic illustration of growing $MAPbI_3$ single crystal platelets. Reproduced with permission from ref 108. Copyright 2020, Elsevier. (c) $MAPbI_3$ nanosheets by decreasing deposition rate. Reproduced with permission from ref 108. Copyright 2020, Elsevier. (d) $CsPbX_3$ (X = I^-, Br^-, Cl^-) SCs microplates. Reproduced with permission from refs 109 and 110. Copyright 2016, Springer Nature. Copyright 2018, Wiley-VCH. (e) Schematic illustration of $CsPbBr_3$ single crystal microstructure. Reproduced from permission from ref 111. Copyright 2019, Royal Society of Chemistry.

5. PEROVSKITE CRYSTALLIZATION FROM SOLID PHASE

5.1. Bridgman Growth Method. The Bridgman growth method utilizes high vapor pressures and temperatures, which could affect the chemical stability of organic compounds. As such, this technique is most commonly used for the synthesis of large all-inorganic perovskite SCs. First, the raw material is placed in a vessel, which is then moved and heated in a furnace

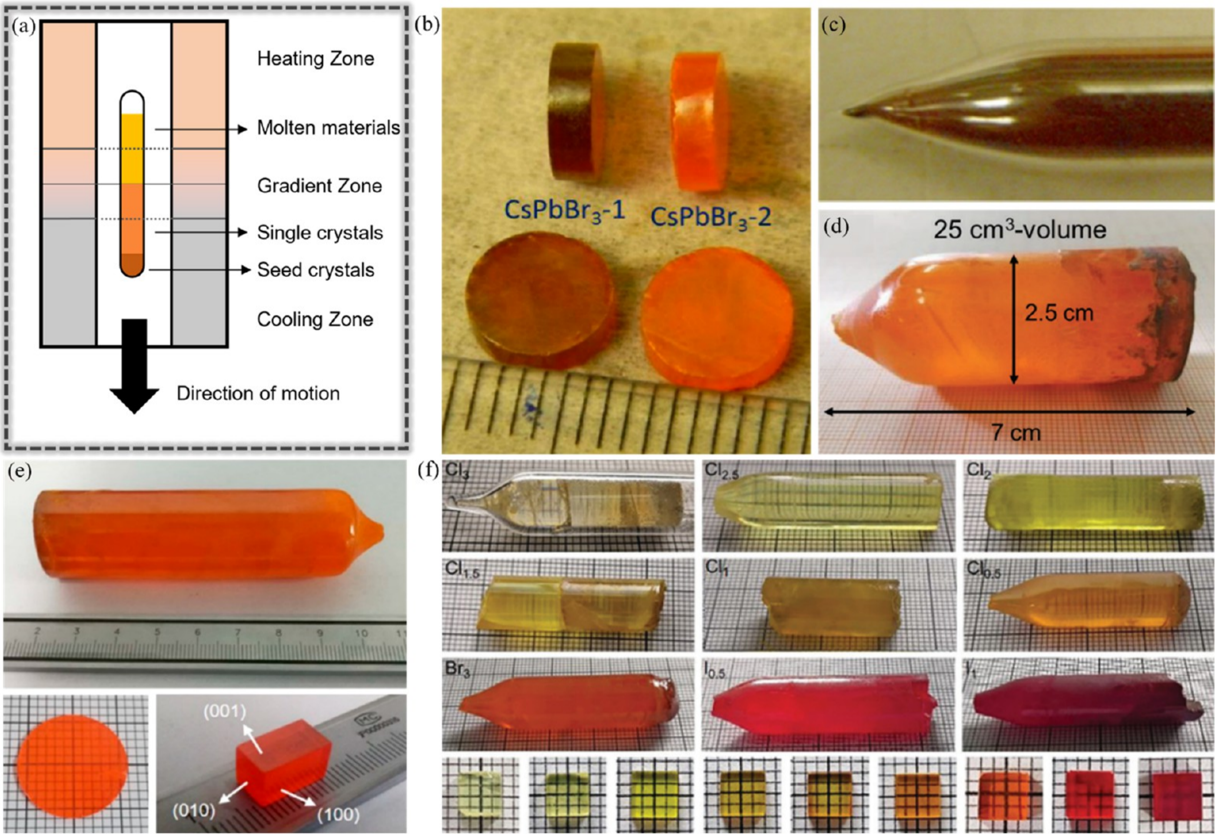

Figure 17. (a) Schematic illustration of the Bridgman growth. Reproduced from permission from ref 113. Copyright 2020, Springer Nature. (b−e) $CsPbBr_3$ SCs. Reproduced from permission from refs 50 and 114−116. Copyright 2013, American Chemical Society. Copyright 2016, American Physical Society. Copyright 2017, Wiley-VCH. Copyright 2018, American Chemical Society. (f) $CsPbBr_{3-3n}X_{3n}$ (X = Cl^-, I^-) SCs. Reproduced from permission from ref 117. Copyright 2021, Royal Society of Chemistry.

at temperatures above the melting point of the precursor. As such, the starting materials melt. As the vessel passes through the furnace and reaches the low-temperature zone at the end, the molten material begins to recrystallize. The seed crystals gradually grow as the temperature continues to drop, forming the desired crystal, as shown in Figure 17a.[113]

The Bridgman growth method produces high-quality crystals because of the ease of controlling the reaction temperature and vessel shape. This method allows for the preparation of mixed perovskite materials with a certain melting point. Furthermore, the interfacial curvature of this material preparation technique can be easily adjusted by varying the temperature at the top and bottom of the reaction vessel.[52] Kanatzidis et al. reported the preparation of $CsPbBr_3$ SCs through the Bridgman method for the first time. Therein, $PbBr_2$ and CsBr were mixed at a molar ratio of 1:1. The precursor mixture was grinded and transferred into a sealed and evacuated fused SiO_2 tube, which was then heated for 6 h to melt the raw materials. After cooling down the products to room temperature, $CsPbBr_3$ SCs were produced, as shown in Figure 17b.[50] On the other hand, Jang et al. mixed the precursor materials for the synthesis of $CsPbBr_3$ and then heated the mixture for 24 h to 700 °C. The temperature was held for 5 h and then was reduced to the room temperature for 24 h to ensure the fabrication of a homogeneous melt. The cooled melt was crushed and transferred to a fused SiO_2 tube, which was then placed in a Bridgman furnace to produce the $CsPbBr_3$ SCs with a diameter of 7 mm, as shown in Figure 17c. $CsSnI_3$ SCs were also produced through the above-mentioned method.[114] Similarly, Zeng et al. successfully synthesized $CsPbBr_3$ SCs through the Bridgman method. A higher temperature was employed in their work, which formed a depressed solid−liquid interface; however, inclusions were observed at the bottom of this interface during the fluctuations in the temperature. To avoid this phenomenon, the temperature and position of the starting materials were adjusted. The synthesized large $CsPbBr_3$ SCs exhibited dimensions up to Φ 2.5 × 7 mm^2, as shown in Figure 17d.[115]

Tao et al. demonstrated that removing impurities from single crystals during the growth process could improve the carrier transport properties of the resulting perovskite. They produced large (Φ 24 mm × 90 mm), high-quality $CsPbBr_3$ SCs with a hole mobility lifetime of 1.46×10^{-2} cm^2 V^{-1} through repeated directional crystallization and impurity removal processes, as shown in Figure 17e.[116] In addition, other halide anions can be introduced into the $CsPbBr_3$ SCs through the improved method to modulate the components and successfully grow $CsPbBr_{3-3n}X_{3n}$ (X = Cl^-, I^-) SCs. The ratio of the ions in the synthesized material was based on that of the ions in the precursor materials, as shown in Figure 17f.[117]

In the Bridgman growth technique, the temperature can be easily adjusted, and the desired crystal shape can be easily produced. However, the crystals are susceptible to interference due to the size limitations of the crystallization vessel. Furthermore, surface contact between the crystal and vessel can cause stresses, cracks, or small grain boundaries in the resulting perovskite crystals.[118]

https://doi.org/10.1021/acs.chemmater.2c03505
Chem. Mater. 2023, 35, 2683−2712

Table 2. Comparison of Growth Methods about Perovskite Single Crystals

growth method	growth conditions	advantages	disadvantages
STL	precise cooling temperature	low cost; simple operation; crystal size controllable	time-consuming; formation of multiphase
ITC	heating; retrograde solubility	high quality; simple operation	materials consuming; temperature sensitive; solvent limitation
SEC	slow solvent evaporation	highly effective; simple operation	time-consuming; random growth
AVC	slow diffusion of antisolvent vapor	high quality; lower cost; energy saving	time-consuming; random growth
CVD	high temperature; vapor deposition	defects reduction; convenient for devices preparation	small crystal size; precise temperature controlling
Bridgman method	vacuum; temperature gradient; zone-melt	temperature tunable; crystal shape and size controllable	energy consuming; unsuitable for growth of organic components

Herein, we give a detailed review of the related perovskite materials and crystal growth methods. A summary and description of the above-mentioned growth methods have been shown in Table 2. Furthermore, the perovskite SCs, properties, and critical parameters are summarized in Table 3. And then, the optoelectronic applications of perovskite SCs will be discussed.

6. OPTOELECTRONIC APPLICATIONS OF PEROVSKITE SINGLE CRYSTALS

Pb-based halide perovskite SCs exhibited great potential as active materials for solar cells, photosensors, and lasers. This section summarizes recent progress in the applications of Pb-based single-crystal perovskites in optoelectronics and discusses vital requirements in optimizing device performance.

6.1. Photovoltaics. Single crystals exhibit higher photovoltaic performance and greater stability than their polycrystalline counterparts because of the lack of grain boundaries in their structures and low bulk defect concentrations, which are approximately 3−5 orders of magnitude lower than those in polycrystals. The photocurrent in thick single-crystal photovoltaic cells may increase due to the secondary absorption of light.[130]

Single-crystal perovskite solar cells can be fabricated using vertical or lateral structures, as shown in Figure 18a.[131] Three types of vertical structure have been reported so far, such as ITO(FTO)/ crystal/metal, ITO(FTO)/ETL(HTL)/crystal/metal, and ITO(FTO)/ETL(HTL)/crystal/HTL(ETL)/metal arrangements. In these vertical structures, ITO, FTO, ETL, and HTL correspond to indium tin oxide, F-doped tin oxide, electron transport layer, and hole transport layer, respectively. In principle, charge-transporting layers are beneficial for extracting charges in a vertical structure. On the other hand, two lateral structures have been observed, such as metal/crystal/metal and metal/ETL(HTL)/crystal/HTL(ETL)/metal configurations. Figure 18b shows a sample schematic of the fabrication of lateral devices. First, the anode was deposited on the crystal surface. An ETL based on C_{60}/bathocuproine (BCP) was thermally evaporated on the anode. Then, the cathode was deposited on the ETL.[132] Figure 18c shows a schematic of the working mechanism of the crystal solar cells. The photogenerated electron−hole pairs in the perovskite light-absorption layer were separated into mobile electrons and holes extracted by the ETL and HTL, respectively.

Over the past five years, considerable progress has been made in the crystal growth, trap passivation, device design, and fabrication of single-crystal perovskite solar cells. The highest power conversion efficiency (PCE) reported for single-crystal solar cells was 22.8%, which is close to their polycrystalline counterpart (25.7%).[133] The first single-crystal solar cell was fabricated with a vertical structure based on $MAPbI_3$; in 2015, Li et al. produced $MAPbI_3$ crystal arrays on poly(3,4-ethylene dioxythiophene):polystyrenesulfonate (PEDOT:PSS)-coated ITO substrate through droplet-pinned crystallization. Then, solar cells with vertical structures, ITO/PEDOT:PSS/$MAPbI_3$ crystal arrays/phenyl-C_{61}-butyric acid methyl ester (PCBM)/ZnO/Al, were fabricated. The PCE of the fabricated device was 1.73%.[134] The relatively low value was attributed to the crystal's thickness, hindering the charge carrier's efficient extraction. The fabrication of thinner crystals is essential to improve the performance of single-crystal solar cells. In 2017, Liu et al. optimized a commercial monocrystalline Si cutting technology and identified the most favorable cutting process, cutting coolant and diamond-impregnated wire. Large perovskite $MAPbI_3$ crystals were sliced into wafers with thicknesses as low as 190 μm.[135] These thin $MAPbI_3$ crystal wafers were used to fabricate a device with a structure of Au/ITO/spiro-OMeTAD/$MAPbI_3$/ PCBM/LiF/Ag/Au. In this structure, spiro-OMeTAD corresponds to 2,2′,7,7′-tetrakis(*N*,*N*-di-4-methoxyphenylamino)-9,9′-spirobifluorene. The PCE of the assembled device was approximately 4%.[135] On the other hand, Li et al. grew high-quality $MAPbI_3$ single crystalline films directly on a FTO/TiO_2 substrate through a facile space-confined solution-processed strategy.[136] The PCE of the device was 8.78%.[137] Huang et al. proposed a facile route to reduce the thickness of crystals synthesized through a hydrophobic interface lateral growth method. MAI solution was introduced onto the crystal surface to reduce the interfacial trap density, leading to a PCE as high as 17.8%.[138] Bakr et al. fabricated high-quality crystals through solution space-limited inversion growth and low-temperature crystallization methods; the corresponding PCE of the synthesized crystals were as high as 21.09 and 21.93%, respectively.[139,140] Recently, Chen et al. introduced a hydrophobic poly(3-hexylthiophene) (P3HT) polymer into HTL to passivate the undercoordinated Pb^{2+} ions on the $MAPbI_3$ crystal surface.[141] Ion diffusion and non-radiative recombination were efficiently suppressed, leading to a PCE as high as 22.1%.

$FAPbI_3$-based SCs exhibit broader light utility. As a result, they are expected to perform better than $MAPbI_3$-based photovoltaic devices. Zhou et al. prepared $(FAPbI_3)_{0.85}(MAPbBr_3)_{0.15}$ crystals through a polydimethylsiloxane (PDMS)-assisted solvent evaporation crystallization method. The PCE of the fabricated solar cell with an ITO/NiO_X/$(FAPbI_3)_{0.85}(MAPbBr_3)_{0.15}$/$TiO_2$/Ag structure was 12.18%.[142] Recently, Bakr et al. synthesized high-quality $FA_{0.6}MA_{0.4}PbI_3$ crystals with a low band gap. The PCE was 22.8%, which is the highest value reported so far.[141] Currently, single-crystal perovskite solar cells with the highest PCE is based on 3D

https://doi.org/10.1021/acs.chemmater.2c03505
Chem. Mater. 2023, 35, 2683−2712

Table 3. Summary of Critical Parameters and Growth Method for Perovskite Single Crystal

perovskite	size	bandgap (eV)	method	growth temperature (°C)	growth period	growth environment	ref
$MAPbI_3$	10 × 10 × 8 mm^3	1.48	STL	40−65	Several days	HI	14
	Lateral 10 mm	1.61	TSSG	75−100	Several days	HI	22
	Lateral 6 mm	1.50	TSSG/ITC	152	3 h	GBL	16
	20 × 18 × 6 mm^3		BSSG	40−105	5 days	HI	18
		1.51	AVC	25	7 days	Solution: GBL Antisolution: DCM	23
	4 × 4 × 2.3 mm^3	1.50	ITC	60−70		Solution: GBL Antisolution: DCM	42
			AVC	25	2 days	HI	119
		1.49	AVC	25−120	30 min	Solution: HI Antisolution: diethyl ether/tetrahydrofuran/DCM/chloroform	120
	71 × 54 × 39 mm^3	1.53	ITC	100	2 days	GBL	84
	Lateral 7 mm	1.51	ITC	110	3 h	GBL	49
			STL	45−90	15 days	HI	73
$MAPbBr_3$	Lateral 3 mm	2.21	TSSG/ITC	80	3 h	DMF	16
	10 × 10 × 5 mm^3	2.15	SEC	25	Several hours	DMF	96
		2.21	AVC	25	7 days	Solution: DMF Antisolution: DCM	23
	1.4 × 1.4 × 0.7 mm^3	2.26	AVC	25	3 days	DMF	44
	5 × 3 × 1.7 mm^3	2.23	ITC	60	Several days	DMF	43
	6 × 6 × 2 mm^3	2.16	ITC	25	1 day	Solution: DMF Antisolution: DCM	42
	25 × 25 × 6 mm^3	2.24	ITC	100	2 days	DMF	84
	Lateral 7 mm	2.18	ITC	80	3 h	DMF	49
	47 × 41 × 14 mm^3	2.24	ITC	25−60	20 days	DMF	65
	Lateral 5 mm		STL	50−70	10 days	HBr	73
$MAPbCl_3$	11 × 11 × 4 mm^3	2.97	ITC	100	2 days	DMSO	84
	2.5 × 2 × 1 mm^3	2.94	ITC	50	6−8h	DMSO:DMF (1:1)	85
$MAPb(Cl_xI_{1-x})_3$	Lateral 3−5 mm	1.46−2.92	ITC	60−90	5−8 days	GBL	13
$MASnI_3$	10 × 10 × 8 mm^3	1.15	TSSG	25−75	One month	HI	76
$MAPb_xSn_{1-x}Br_3$	16 × 14 × 10 mm^3	2.02−2.18	TSSG	40−68	2 h	HBr	17
$MAGeI_3$		1.9	SEC	25−120	30 min	HI	11
$FAPbI_3$	Lateral 3 mm	1.40	ITC	80−120	5 h	GBL	81
	Lateral 6 mm	1.54	ITC	60−105	3 h	GBL	86
	Lateral 20 mm	1.49	ITC	80−120	12 h	GBL	121
	4.2 × 4.2 × 1.2 mm^3	1.41	ITC	80−120	5 h	GBL	81
$FAPbBr_3$	Lateral 5 mm	2.13	ITC	40−60	5 h	DMF	81
$FA_{(1-x)}MA_xPbI_3$	4.5 × 4.5 × 1.2 mm^3	2.15	ITC	40−60	5 h	DMF:GBL (1:1)	122
	Lateral 4 mm		ITC	40−60	5 h	GBL/HI	4
$MA0_{.45}FA_{0.55}PbI_3$	Lateral 8 mm		ITC	120−160	4.5 h	GBL	87
$CsPbI_3$			ITC	25−110	4 h	DMF	89
$CsPbBr_3$			TSSG	40−120	48 h	DMSO	103
	Lateral 5 mm	2.2	AVC	25	48 h	Solution: DMSO Antisolution: MeCN/MeOH	51
			STL	25−100	36 h	H_2O	19
			ITC	25−120	3.5 h	DMSO	123
	Lateral 1 mm	2.29	AVC	25	3−4 days	Solution: DMSO Antisolution: DCM	124
	Φ7 × 2.1 mm^3	2.25	Bridgman method	25−600	24h		114
	Φ26 × 100 mm^3	2.25	Bridgman method	60−1470	14 days		115
	6 × 6 × 3 mm^3	2.29	Bridgman method	25−590	3−5 days		125
	Φ24 × 90 mm^3	2.25	Bridgman method	25−600	3 days		116

https://doi.org/10.1021/acs.chemmater.2c03505
Chem. Mater. 2023, 35, 2683−2712

Table 3. continued

perovskite	size	bandgap (eV)	method	growth temperature (°C)	growth period	growth environment	ref
	$5 \times 5 \times 2$ mm^3		Bridgman method	25−645	70 h		126
	$3 \times 0.5 \times 0.5$ mm^3	2.254	ITC	90−110	12 h	DMSO/DMF/CyOH	88
			STL	40−80	12 h	HBr	127
	$42 \times 5 \times 3$ mm^3	2.29	AVC	25	3−14 days	Solution: DMSO Antisolution: MeOH	104
		2.21	ITC	60−120	10 h	DMSO	89
	Lateral 2 mm	2.19	ITC	60−90		DMSO/DMF/GBL	90
$CsPb_2Br_5$		3.1	AVC	25	5 weeks	Solution: DMSO Antisolution: MeOH	128
$Cs_2PbI_2Cl_2$		3.06	Bridgman method	25−650	6 days		129
Cs_4PbBr_6	Lateral 0.5 mm	2.35	AVC	25	A few days	Solution: DMSO Antisolution: DCM	124
$CsPbBr_xI_{(3-x)}$			ITC	60−160	10 h	DMSO	91
$CsPbBr_{3-3n}X_{3n}$ (X = Cl, I)	$7 \times 7 \times 1.5$ mm^3	1.90−2.88	Bridgman method	25−600	3 days		117
$MA_xCs_{1-x}PbBr_3$	Lateral 10 mm	2.16−2.25 eV	AVC	25−30	14 days	DMF (for $MAPbBr_3$) DMSO (for $CsPbBr_3$)	36
$MA_xCs_{1-x}PbBr_3$	Lateral 0.5−1.5 mm	2.29−2.34 eV	ITC	25		DMF	51

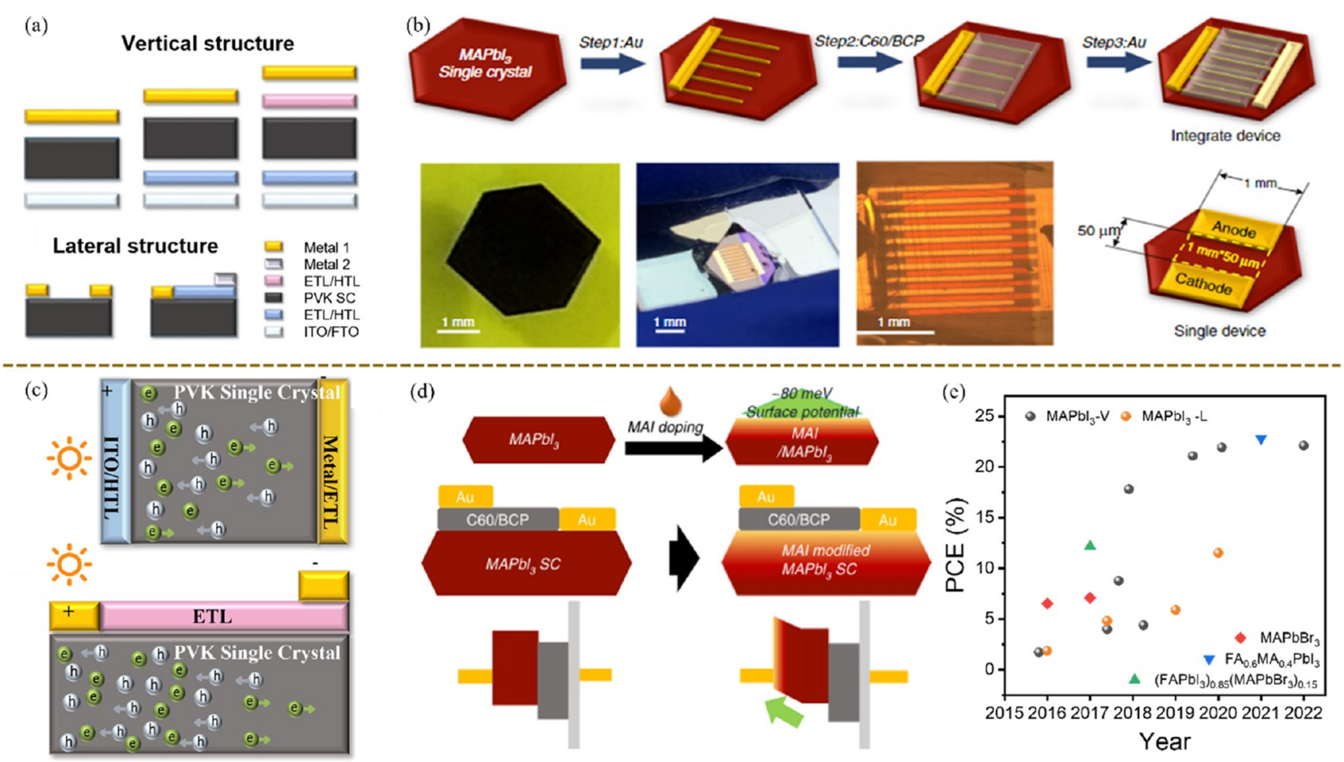

Figure 18. (a) Various architectures of single crystal perovskite solar cells (SCPSCs = single crystal perovskite solar cells). (b) Fabrication of lateral structure perovskite crystal solar cells. Reproduced with permission from ref 132. Copyright 2020, Springer nature, reproduced without any modification and licensed under CC BY 4.0, https://creativecommons.org/licenses/by/4.0/. (c) Working principle of perovskite crystal solar cells (PVK = perovskite). (d) Schematic diagram of device structures and energy levels for SCPSCs with and without MAI treatment.(SC = single crystal) Reproduced with permission from ref 132. Copyright 2020, Springer nature, reproduced without any modification and licensed under CC BY 4.0, https://creativecommons.org/licenses/by/4.0/. (e) Summary of PCEs for different SCPSCs.

perovskite single crystal materials, but the performance of perovskite solar cells prepared by 2D perovskite single crystal has also been developing. Gao et al. found that an initial power conversion efficiency of 5.83% was obtained from the $(CH_3(NH_2)_2)_2(CH_3NH_3)_3Pb_4I_{13}$ perovskite, with reasonable stability after aging for 1200 h.[143] Apart from the continuous development of organic−inorganic halide single-crystal perovskite solar cells, the inorganic perovskite solar cells efficiency has also raised. Song et al. reported that controlling the growth of $CsPbI_3$ crystal grains by vacuum-assisted thermal annealing

https://doi.org/10.1021/acs.chemmater.2c03505
Chem. Mater. 2023, 35, 2683−2712

Table 4. Summary of Critical Parameters and Corresponding Device Performance for Perovskite Crystal Solar Cells

	materials	growth method	device structure	incident wavelength (nm)	EQE (%)	R (A W^{1-})	D^* (Jones)	τ_r/τ_f	I_p/I_d	ref
Photoresistor	$MAPbBr_3$ microwire-array	Template-assisted method	Au/PVK/Au (lateral)	365		20	4.1×10^{11}	1.6/6.4 ms	$>10^5$	147
	$MAPbBr_3$	STL	Au/Cr/PVK/Cr/Au (lateral)	525	3900	16	6×10^{13}	43/36 μs	$>10^5$	148
	$MAPbBr_3$ planar-integrated	AVC	ITO/PVK	520	$>10^4$ (G)	>4000	$>10^{13}$	25/25 μs		34
	$MAPbBr_3$	ITC	Au/PVK/Au (lateral)	532	25	~0.1		0.08/0.09 s		149
	$MAPbI_3$	BSSG	Au/PVK/Au (lateral)	532	2.2×10^5	953		74/58 μs		15
	$MAPbI_3$	ITC	Au/PVK/Au (lateral)	808	22	~0.15		0.12/0.08 s		149
	$(C_4H_9NH_3)PbI_4$	STL	Au/PVK/Au (lateral)			~0.01	1.6×10^{13}	1.7/3.9 μs	$\sim 10^4$	150
	$(C_4H_9NH_3)\cdot MAPb_2I_6$	STL	Au/PVK/Au (lateral)			38	2.4×10^{13}	773/385 ms	$\sim 10^3$	150
	$(BA)_2(MA)Pb_2I_7$	STL	ITO/Au/PVK/Au (lateral)	620	200		10^{11}	125/74 ms	$\sim 10^3$	151
	$(PEA)_2PbBr_4$	STL	SiO_2/PVK/Au	405					$\sim 10^3$	152
	$PEA_2PbI_4\cdot(MAPbI_3)$	STL	Au/PVK/Au (lateral)	500	50	0.2	1.1×10^{13}			153
	$FAPbI_3$ wafer	STL	Au/PVK/Au (lateral)	515	~900	4.5		8.3/7.3 ms		121
	$MAPbI_3$ wafer	dynamic flow microreactor system	Au/PVK/Au (lateral)	635	600	2.5				154
	$(PEA)_2PbI_4$ SCM	induced peripheral crystallization	Au/PVK/Au (lateral)	462	26530	98.17	1.62×10^{15}	64/52 μs		63
Phototransistor	$MAPbCl_3$ thin-SC	ITC	Si/SiO_2/PVK/Au						1.45×10^5	155
	$MAPbBr_3$ thin-SC	ITC	Si/SiO_2/PVK/Au						3.37×10^5	155
	$MAPbI_3$ thin-SC	ITC	Si/SiO_2/PVK/Au						8.78×10^4	155
	$(C_4H_9NH_3)_2PbBr_4$	Solution-processed method	(Si/SiO_2)/PVK/graphene	470		~2100			$\sim 10^3$	156
	$CsPbBr_3$ thin-SC		Si/SiO2)/Au/PVK/MoS_2/Cr	442		13.1		2.5/1.8 ms	$>10^3$	157
Photodoide	$MAPbBr_3$ thin-SC	Space-limiting method	ITO/PTAA/PVK/C60/BCP/Cu	402	52–60	0.17–0.26	1.5×10^{13}	-/7.2 μs		158
	$MAPbBr_3$ thin film	Space-limiting method	ITO/PVK/Au/Pt	405	5×10^7 (G)	1.6×10^7	1.3×10^{13}	81/892 μs		159
	$MAPbI_3$ thin-SC	Space-limiting method	ITO/PTAA/PVK/C60/BCP/Cu	402	50–62	0.17–0.32		-/3.1 μs		158
	$MAPbBr_{3-x}Cl_x$ and $MAPbI_{3-x}Br_x$	STL	Glass/Ga/PVK/Au	425–640						160

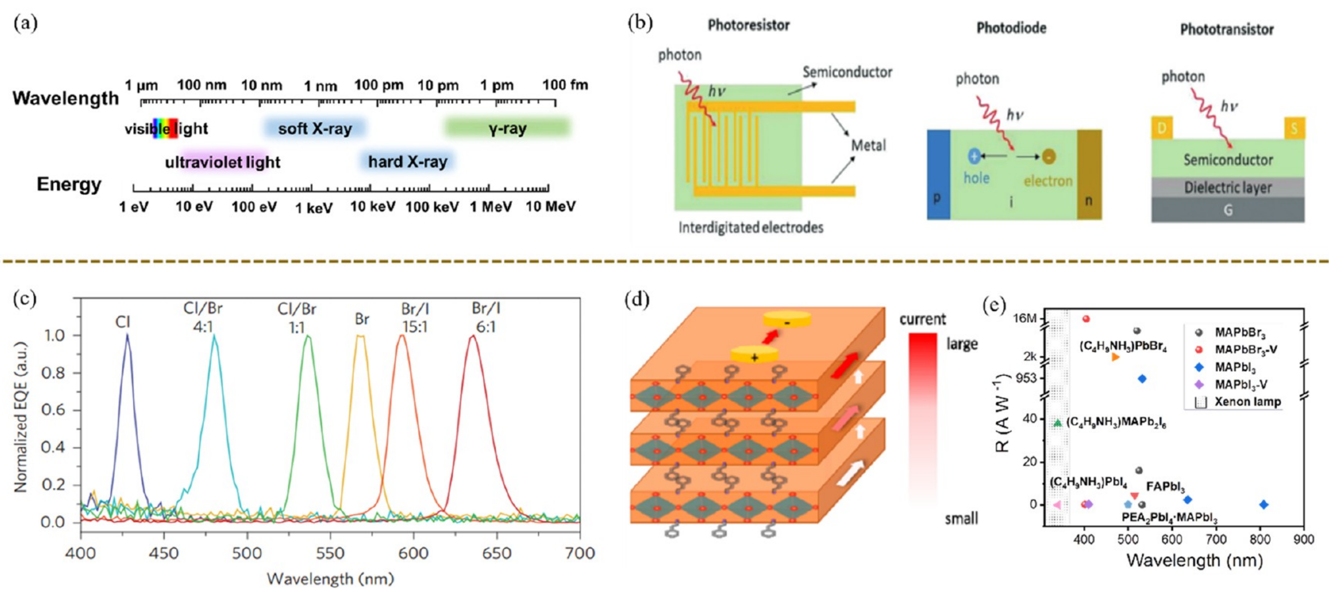

Figure 19. (a) Spectral wavelength classification and corresponding energy ranges. (b) Schematic illustrations of photodetectors. (c) Normalized EQE spectra of single-halide and mixed-halide perovskite single-crystal photodetectors with different halide compositions, showing the ultranarrow EQE peak and tunable spectral response (EQE spectra were measured under −1 V bias). Reproduced with permission from ref 160. Copyright 2015, Springer nature. (d) Schematic illustration of the confined charge carrier transport on the top of the 2D perovskite crystals. Reproduced with permission from ref 153. Copyright 2017, American Chemical Society. (e) Summary of responsivity for different perovskite SC visible light detectors.

could optimize the morphology and crystallinity of the $CsPbI_3$ perovskite films, which lead to that the PCE of the solar cells is increased from 17.26 to 20.06%.[144]

In contrast to vertical-structured devices, crystal thickness is less detrimental to charge transport processes in lateral-structured devices. In 2015, Huang et al. fabricated an efficient lateral battery based on piezoelectric-polarized $MAPbI_3$ SCs, reducing the need for expensive and inefficient transparent electrodes. Under 0.25 solar illumination at room temperature, the device with the structure Au/$MAPbI_3$/ Au achieved a PCE of 1.88%.[145] By introducing a C_{60} ETL to the $MAPbI_3$ wafer, the device efficiency increased to 5.9%.[97] On the other hand, Sung et al. employed a simple drum printing method to fabricate patterned $MAPbI_3$ thin films (3×3 in^2). The PCE of the fabricated device with a structure of SiO_2/ $MAPbI_3$/ Au/ PCBM/Ag was 4.83%.[146] In 2019, Dong et al. performed surface passivation through MAI treatment to improve the surface conductivity of $MAPbI_3$ SCs, as shown in Figure 18d, and achieved a PCE as high as 11.52%. Under 1 sun illumination for 200 h, no losses were observed at the maximum power condition.[97] The progress in perovskite crystal solar cells in terms of materials and device performance is summarized in Figure 18e. On the other hand, Table 4 outlines the materials, crystal growth methods, device structures, and photovoltaic parameters.

6.2. Photodetectors. Photodetectors are electronic devices capable of converting the incident optical signal into an electrical signal, with a wide range of applications, including optical communication systems, chemical/biological testing, and image detection. According to the bandgap of the semiconductor used in these devices, photodetectors can transduce photons of different energies. Perovskite SCs are promising materials for detecting photons from different electromagnetic spectra. Figure 19a shows the different types of electromagnetic waves classified according to their wavelengths in the molecular spectrum and their corresponding energy range. The broad spectral range of perovskite photodetectors allows their applications for near-infrared (NIR), ultraviolet (UV), visible light, and high-energy radiation applications.[161] Photodetectors work by converting photon energy to current or voltage output. First, the devices absorb photon energy to generate excitons. Then, these excitons or charges diffuse or drift through the material. The electrodes then collect these free charges. According to the photo conversion mechanism, photodetectors can be classified into photoresistors, photodiodes, and phototransistors (Figure 19b).[162] In this review, we discuss only visible light and high-energy X-ray radiation detection using perovskite-based devices.

6.2.1. Visible Light Detection. The performance of visible light detectors is evaluated using several parameters such as responsivity (R), detectivity (D^*), gain (G), and external quantum efficiency (EQE). R quantifies the photocurrent generated by the device in the external circuit under the action of the input unit optical power, which reflects the conversion ability between the input optical and output electrical signals of the detectors. On the other hand, the values of D^* and G represent the ability of the device to detect the minimum optical signal, unit incident photon, and carriers collected by the electrode.[163] EQE represents the electron−hole logarithm produced by the unit incident photon, relating the conversion efficiency between the input optical and output electrical signals of the detectors.

So far, the perovskite crystal-based visible light detectors have shown innovative and disruptive applications for high-speed optical communication and high-resolution imaging both in scientific research and industry due to the high absorption coefficient, adjustable optical bandgap, high carrier mobility, and long carrier diffusion length.[164] Sun et al. synthesized the first perovskite crystal-based visible light detector based on bulk $MAPbI_3$ SCs, which exhibited better optoelectronic properties than its thin-film counterparts.[15] The

https://doi.org/10.1021/acs.chemmater.2c03505
Chem. Mater. 2023, 35, 2683−2712

Table 5. Summary of Critical Parameters and Corresponding Device Performance for Perovskite Crystal Visible Light Detectors

structure	device structure	growth method	thickness (μm)	V_{oc} [V]	J_{sc} [mA cm^{-2}]	FF	PCE [%]	ref
vertical-structure	ITO/PEDOT:PSS/$MAPbI_3$ SC arrays/PCBM/ZnO/Al	Droplet-pinned crystallization method	∼1.5	0.52	8.69	0.379	1.73	134
	FTO/TiO_2/$MAPbBr_3$ SC/Au	Cavitation-triggered asymmetrical crystallization strategy	∼1	1.36	6.96	0.69	6.53	100
	FTO/TiO_2/$MAPbBr_3$ SC/Spiro-OMeTAD/Ag	Space-limited ITC	16	1.31	8.77	0.62	7.11	169
	Au/ITO/Spiro-Meo-TAD/$MAPbI_3$ SC wafer/PCBM/LiF/Ag/Au	Top-down method	NA	1.15	20.02	NA	4	135
	FTO/TiO_2/$MAPbI_3$ SC/Spiro-OMeTAD/Ag	Self-grow directly on electron-collecting FTO/TiO_2	NA	0.668	22.28	NA	8.78	137
	ITO/NiO_x/$(FAPbI_3)_{0.85}(MAPbBr_3)_{0.15}$ SC/TiO_2/Ag	SEC	24.5	23.14	1.03	0.51	12.18	142
	ITO/PTAA/$MAPbI_3$ SC/PCBM/C60/BCP/Cu	Hydrophobic interface-confined lateral growth method	10	1.08	21	0.786	17.8	138
	ITO//PEDOT:PSS/$MAPbI_3$ SC/PCBM/Ag	Seeded space-limited ITC	∼50	0.75	22.15	0.27	4.4	170
	ITO/PTAA/$MAPbI_3$/(C60/BCP)/Cu	Low-temperature ITC	20	1.144	23.68	0.81	21.93	140
	ITO/PTAA/$MAPbI_3$ SC/C60/BCP/Cu	Solution space-limited ITC	20	1.076	23.46	0.835	21.09	139
	Cu/(C60/BCP)/MAPbl$_3$ SC/PTAA:P3HT/Au	Space-confined ITC		1.13	23.88	0.818	22.1	171
	ITO/PTAA/$FA_{0.6}MA_{0.4}PbI_3$ SC/C60/BCP/Cu	Space limited ITC	15	1.1	26.2	0.79	22.8	141
lateral-structure	Au/$MAPbI_3$ /Au	STL		0.82	2.28 (0.25 sun)	NA	1.88	172
	SiO_2/$MAPbI_3$/Au/PCBM/Ag	Facile roll-printing method		0.81	18.33	0.329	4.83	146
	Au/(C60/BCP)/MAPbl3 SC wafer/Au	STL		0.66	5.06 (0.25 sun)	0.44	5.9	97
	Au/(C60/BCP)/MAI modified MAPbl$_3$ SC/Au	Simple methylammonium iodide surface treatment		0.93	22.49	0.51	11.52	132

devices were fabricated with a planar Au/$MAPbI_3$/ Au structure. Under visible light irradiation (λ = 532 nm, intensity = 2.12 nW cm^{-2}), the values of R and EQE were 953 A W^{1-} and 2.22 × 10^5%. The devices exhibited good stability and a relatively high response speed of 58 μs.

Halide engineering is an efficient strategy for regulating the bandgap of $MAPbX_3$ crystals and their corresponding photoresponse to illumination. Liu et al. developed a low-temperature gradient crystallization method to synthesize $MAPbBr_3$ SCs with high crystal quality, high uniformity, long carrier lifetime, high carrier mobility, low trap density, and long-term stability.[148] The fabricated pixel array imaging modules exhibited an astonishingly high response speed of approximately 40 μs. Furthermore, the high values of R (16 A W^{1-}) and D* (6 × 10^{13} Jones) revealed the modules' excellent responsivity and efficient detectivity. Huang et al. synthesized mixed halide perovskite $MAPbBr_{3-x}Cl_x$ and $MAPbI_{3-x}Br_x$ SCs.[160] The absorption edge gradually changed from blue to red, as shown in Figure 19c. The crystal detectors exhibited a tunable spectral response from blue to red by changing the halide composition and bandgap width. Later, they fabricated vertical *p-i-n* detectors based on thin $MAPbBr_3$ and $MAPbI_3$ SCs (10 μm) with low dark current, low noise equivalent power, and high specific detection.[158] The device registered a sub-pW cm^{-2} weak light detection limitation. Liu et al. also reported that the textured single-crystal photodetector based on $MAPbBr_3$ exhibits the superior responsivity of 63.0 A W^{1-}, external quantum efficiency of 1.50 × 10^4%, and detectivity D* of 8.12 × 10^{12} Jones under 520 nm irradiations with a weak power density of 0.54 μW cm^{-2} at 3 V, which are more than 4200% and 80000% higher than those of the photodetector based on single-crystal bulk and polycrystalline film, respectively. These photodetectors prove the great potential of perovskite thin SCs as materials for high-performance visible light detectors.[165] Furthermore, Yu et al. prepared the perovskite photodetector with a horizontal structure based on a $(FAPbI_3)_{0.79}(MAPbBr_3)_{0.13}(CsPbI_3)_{0.08}$ single-crystalline thin film (SC−TF), which exhibited excellent performance with an enhanced responsivity of 40 A W^{1-}, high detectivity of 1.9 × 10^{13} Jones, external quantum efficiency of 9100%, and superior stability.[166]

The thickness of the SCs affects the extraction of carriers in detectors. Therefore, the growth and application of thin crystalline wafers have received considerable research attention. In a pioneering work, Liu et al. successfully prepared 150 μm-thick $MAPbI_3$ and $FAPbI_3$ crystal wafers through geometrically controlled dynamic flow reaction and diamond wire saw cutting processes.[121,154] Wafer-based detectors exhibit better performance and higher photoelectric loudness than their polycrystalline counterparts. Bakr et al. fabricated a planar-integrated single-crystal (ISC) perovskite with a thickness of approximately 5 μm. The ISC perovskite can form highly crystalline thin films with areas larger than 1 cm^2 on planar surfaces without matching the substrate's lattice and even on amorphous surfaces, such as glass.[34] Metal−semiconductor−metal detectors were fabricated based on these $MAPbBr_3$ ISC perovskite crystals, delivering a high gain (more than 10^4 electrons per photon) and high gain bandwidth product (above 10^8 Hz). Ma et al. fabricated a visible light detector based on a SC−TF of $MAPbBr_3$ perovskite with an optimized thickness of hundreds of nanometers. When the thickness of the SC−TF was decreased from approximately 10 μm to several hundred nanometers, the device's minimum detectable power and internal gain increased by two and 4

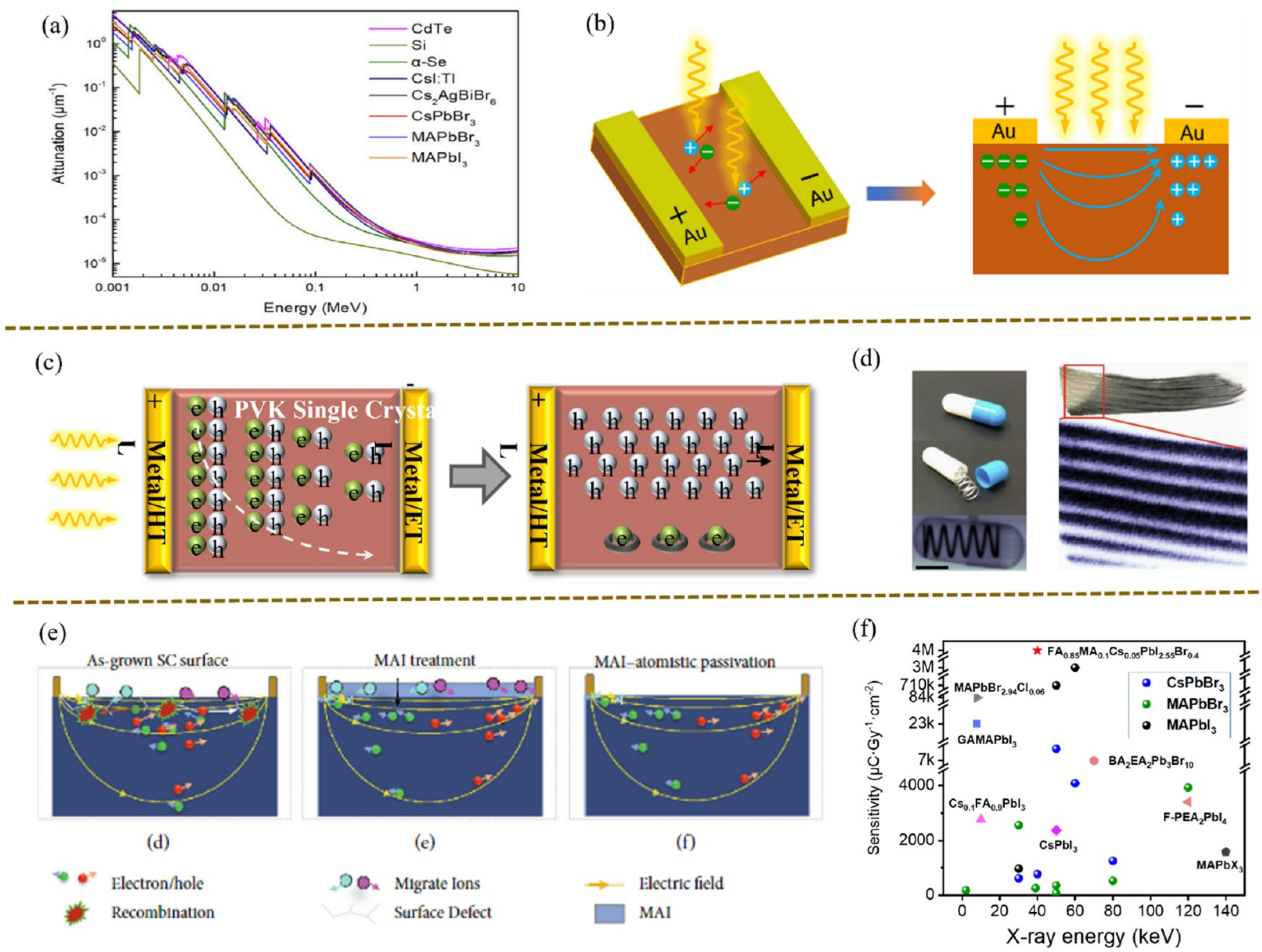

Figure 20. (a) Attenuation coefficients versus photon energy for some representative semiconductors. Reproduced with permission from ref 173. Copyright 2021, Elsevier. (b, c) Sketches of the planar and vertical structure of the X-ray detector. Reproduced with permission from ref 176. Copyright 2020, Wiley-VCH. (d) Optical and X-ray images of an encapsulated metallic spring and a portion of a fish caudal fin. Reproduced with permission from ref 180. Copyright 2017, Springer Nature. (e) Schematic diagram of the working principle of the X-ray detector with different surface treatments. Reproduced with permission from ref 186. Copyright 2020, American Association for the Advancement of Science, reproduced without any modification and licensed under CC BY 4.0, https://creativecommons.org/licenses/by/4.0/. (f) Summary of sensitivity for different perovskite crystal X-ray detectors. The abscissa is the highest voltage value, which is the keV of the X-ray tube.

orders of magnitude, respectively. The ultrahigh sensitivity of the fabricated photodetector can be attributed to the replacement of the polycrystalline thin film with the thickness-optimized SC−TF, which further confirmed the importance of the thickness of the perovskite active layer to the performance of photodetectors.[159] Sun et al. fabricated a single-crystal microwire array (SCMWA) based on $MAPbBr_3$ and encapsulated it with a hydrophobic trichlorosilane molecular layer.[147] The values of R and D^* of the fabricated high-performance flexible photodetector based on the $MAPbBr_3$ SCMWA were 20 A W^{1-} and 4.1 × 10^{11} Jones, respectively. The device maintained its original performance for more than one year without further encapsulation, which proved its excellent stability. Ding et al. synthesized centimeter scale fully inorganic perovskite $CsPbBr_3$ SC−TF (<40 μm) by an improved confined space method to adjust the heating area to control nucleation. The planar metal−semiconductor−metal photodetector using $CsPbBr_3$ SCF as the photosensitive layer demonstrates a limit response time of 200/300 ns and a visible light communication within 100−500 kHz frequency for both 365 nm and white light, which is superior to previously reported $CsPbBr_3$ polycrystalline film and single crystal photodetectors.[167]

As shown in Figure 19d, some 3D and ultrathin 2D layered perovskite crystals are promising materials for photodetection because of their improved stability and effectively suppressed ion migration. For example, Liu et al. proposed an induced peripheral crystallization method for the growth of a 2D flexible single-crystalline membrane (SCM) with a thickness as low as 0.6 μm and an area of more than 2500 mm^2.[63] The photodetector based on the $(PEA)_2PbI_4$ SCM exhibited an efficient photoelectric detection performance; the corresponding *EQE*, *R*, and D^* values were 26530% 98.17 A W^{1-}, and 1.62 × 10^{15} Jones, respectively. Bakr et al. also synthesized 2D $PEA_2PbI_4{\cdot}(MAPbI_3)_{n-1}$ (n = 1, 2, 3) crystals,[153] which exhibited a low concentration of self-doping and low electronic noise. The photodetectors based on these 2D crystals achieved an extremely high optical detection rate (10^{13} Jones), making them particularly advantageous for detecting weak light signals. However, Yu et al. achieved ultrahigh efficiency lateral structured photodetectors using 2D perovskite $PEA_2MA_3Pb_4I_{13}$ single crystals by an in situ reverse temperature crystallization. The photodetector with a record *EQE* of 7.2 × 10^6% showed the highest responsivity of 3077 A W^{1-}, which is over 20 times higher than previous reports.[168] Peng et al. fabricated $(C_4H_9NH_3)_2PbBr_4$ crystals with deep-blue luminescence.[156] In the interdigital graphene electrode structure, photoconductive photodetectors exhibited an ultrahigh value of *R* (2100 A W^{1-}), very low dark current (10^{-10} A), and high on−off current ratio (10^3).

The materials and device performances of the previously reported crystal visible light detectors are outlined in Figure 19e. The corresponding materials, crystal growth methods, device structures, and photoresponse parameters are summarized in Table 5.

Overall, the growth of high-quality crystals with few defects and low ion migration through materials engineering and chemical regulation is necessary. Device engineering should also be considered to achieve better photoresponse. For instance, photoconductive photoreceptors exhibit high values of *G* and *EQE* and can be fabricated through facile synthesis methods. However, their detection capability is reduced because of the large ohmic contact, large external bias voltage, high dark current, and slow photoresponse. On the other hand, photodiodes exhibit fast response and highly sensitive detection. However, they usually suffer from a low response and poor *EQE*. Therefore, a three-terminal phototransistor photodetector should be developed to balance these parameters.

6.2.2. High-Energy X-ray Radiation Detection. Figure 20a shows the absorption spectra of perovskite materials and conventional semiconductors for a wide range of photon energies calculated using the photon cross-section database.[173] Perovskite materials exhibit great potential for high-energy radiation detection owing to their high absorption coefficients, particularly due to the high atomic number of Pb in Pb-based perovskites. High-energy radiation devices can be classified as direct or indirect detectors based on the detection mechanism.[174] In direct detectors, electrons and holes convert X/γ rays radiation into electrical signals under the application of an external bias.[175] Similar to single crystal solar cells, direct-type detectors can be fabricated using lateral or vertical structures, as shown in Figure 20b and c.[176] On the other hand, indirect-type detectors convert the absorbed high-energy X/γ rays into optical signals through a scintillator. The optical signals are then detected by photodetectors and finally converted into electrical signals. The key performance parameters for direct detectors are the charge carrier mobility and lifetime product ($\mu\tau$), which reflect the charge collection efficiency of the semiconducting high-energy radiation detectors; higher values of these parameters imply better performance of the device. Meanwhile, signal-to-noise ratio (SNR) defines the ratio of the intensity of the electrical/optical signal to that of the background noise. The International Union of Pure and Applied Chemistry (IUPAC) defines the detection limit as the equivalent dose rate when SNR = 3. The most important performance indicator for high-energy radiation detectors is the sensitivity (*S*), which describes the response of the X-ray detector to a specific amount of radiation. In addition to their high absorption coefficient, the large $\mu\tau$ and high bulk resistivity of perovskite SCs also contribute to their great potential for high-energy radiation detection.[173,177,178]

In 2013, Stoumpos et al. used perovskite crystals for X-ray radiation detection for the first time.[50] The fabricated all-inorganic $CsPbBr_3$ crystals exhibited the $\mu\tau$ value as high as 1.7 × 10^{-3} cm^2 V^{-1}, which was approximately 10 times higher than the traditional CdZnTe material. This work highlighted the potential of perovskite crystals as X-ray detectors. Since then, great progress has been made in the application of perovskite SCs as X-ray detectors. For example, materials engineering through doping Rb into $CsPbBr_3$ enhanced the atomic interaction and orbital coupling between the Pb and Br atoms, which improved the carrier transport properties and X-ray detection performance of the perovskite.[179] The X-ray detector based on $Cs_{(1-x)}Rb_xPbBr_3$ exhibited a higher sensitivity (8097 μC Gy_{air}^{-1} cm^{-2}) than the $CsPbBr_3$ SC device (918 μC Gy_{air}^{-1} cm^{-2}) even at Rb dopant concentration as low as 0.037%. Huang et al. demonstrated the application of an organic−inorganic hybrid perovskite SCs in radiation detection. X-ray detectors were fabricated using 2−3 mm-thick $MAPbBr_3$ crystals.[37] The value of *S* of the device toward X-ray detection was 80 μC Gy_{air}^{-1} cm^{-2}. They also integrated 0.15 mm-thick $MAPbBr_3$ SCs to Si substrates,[180] which significantly reduced the dark current at high bias and increased the value of *S* to 2.1 × 10^4 μC Gy_{air}^{-1} cm^{-2}; the measured sensitivity was more than a thousand times higher than that of an amorphous Se X-ray detector. Figure 20d shows the clear images of the spring and caudal fins in the capsule. Later, Zhu et al. synthesized high-quality large $MAPbI_3$ SCs through a continuous-mass transport process (CMTP).[181] The performance of the CMTP-synthesized $MAPbI_3$ X-ray detector was comparable to those of the traditional high-quality CdZnTe-based devices.

Adding large cations to perovskite materials reduces the octahedral inclination of the PbI_6 framework. This phenomenon is known as the size effect, which stabilizes the perovskite structure. The introduced cations can also change the coordination between the ions within the crystals. For example, H-bonds derived from large organic cations and inorganic skeletons can improve the rigidity of cubic octahedral structures.[182,183] Yuan et al. prepared high-quality large perovskite SCs of $DMAMAPbI_3$ and $GAMAPbI_3$ by adding DMA^+ and GA^+ cations to $MAPbI_3$.[184] The addition of these large cations inhibited the electron−phonon coupling, increased the formation energy of defects, and reduced the nonradiative recombination. The sensitivity (2.3 × 10^4 μC Gy_{air}^{-1} cm^{-2}) and detection limit (16.9 nGy_{air} s^{-1}) of the $GAMAPbI_3$-based detectors were about an order (2.5 × 10^3 μC Gy_{air}^{-1} cm^{-2}) and three orders (19.1 μGy_{air} s^{-1}) of magnitude better than those of the control $MAPbI_3$ crystal detectors, respectively. The introduction of large cations can also regulate crystal growth to achieve better crystal quality. Huang et al. proposed a ligand-assisted solution method using 3-(decyldimethylamino)propanesulfonate inner salt (DPSI) as an additive to fabricate high-quality $MAPbI_3$ perovskite SCs.[185] The interaction of the DPSI ligands with the Pb^{2+} ions can inhibit the nucleation in the solution and lead to anisotropic crystal growth. The crystals exhibited better crystallinity due to the reduction of the bulk defect density by a factor of 23. The suppression of ion migration resulted in X-ray detection sensitivity as high as 2.6 ± 0.4 × 10^6 μC Gy_{air}^{-1} cm^{-2} and a detection limit as low as 5.0 ± 0.7 nGy_{air} s^{-1}.

Ion migration, which causes the high dark current, low imaging resolution, and instability of devices, should be considered when designing and fabricating high-performance

https://doi.org/10.1021/acs.chemmater.2c03505
Chem. Mater. 2023, 35, 2683−2712

Table 6. Summary of Critical Parameters and Corresponding Device Performance for Perovskite Crystal X-ray Detectors

perovskite	growth method	dimension	thickness (mm)	device structure	$\mu\tau$ product ($cm^2\ V^{-1}$)	sensitivity ($\mu C\ Gy_{air}^{-1}\ cm^{-2}$)	detection limit ($nGy_{air}\ s^{-1}$)	electric field ($V\ mm^{-1}$)	X-ray energy (keV)	ref
$CsPbBr_3$ SC	ITC	3D		Ag/PVK/ITO		770			40	192
	ITC	3D	2	Al/PVK/Au	$(2.5 \pm 0.2) \times 10^{-3}$	1256		20	80	193
	AVC	3D	2	Au/MoO_3/PVK/Ag		619		45	30	194
	STL	3D	1	ITO/NiOx/Poly-TPD/PVK/C70/BCP/Cu		4086		5	60	123
Rb-doped $CsPbBr_3$ SC	ITC	3D	∼1.5	Au/PVK/Au	7.2×10^{-4}	8097		20.1	50	179
$MAPbBr_3$ SC	ITC	3D	2.6	Au/MoO_3/PVK/Ag		2552		45	30	194
	STL	3D	0.15	Si/PVK/C60/BCP/Au	4×10^{-3}	21000	<100	46.7	8	180
	AVC	3D	∼2	Au/PVK/C60/BCP/Ag or Au	1.2×10^{-2}	80	500	25	50	37
	Liquid-diffused separation induced crystallization	3D	2.02	InGa/C70/PVK/Au.		184.6	<1200	1.98	∼2	96
	ITC	3D	∼5	Au/PVK/C60/BCP/Cr	2.59×10^{-2}	3928.3	8800	61	120	195
	ITC	3D	∼3	Au/PVKSC/Au.	4.1×10^{-2}	259.9		0.83	39	196
	AVC	3D	∼2	AZO/PVK/Au	2.6×10^{-4}	∼529	1210	5	80	197
Se-doped $MAPbI_3$ SC	Temperature-dependent crystallization	3D	4	Au/PVK/Au	1×10^{-3}	21000			60	198
Cuboid-$MAPbI_3$	Seed dissolution-regrowth method	3D	1	Au/Cr/PVK/Cr/Au	3.26×10^{-3}	968.9		1	30	199
$MAPbI_3$	Continuous-mass transport process	3D	1−2	Au/PVK/Au	1.6×10^{-3}				8	181
$MAPbI_3$ SC with DPSI	Ligand-assisted solution process	3D	2.4	Cr/PVK/C60/BCP/Cr	1.3×10^{-2}	2.9×10^{6}	5..7	41.67	60	185
$FA_{0.85}MA_{0.1}Cs_{0.05}PbI_{2.55}Br_{0.4}$	STL	3D	∼1	Au/BCP/C60/PVK/SpiroTTB/Au		$(3.5 \pm 0.2) \times 10^{6}$	42	60	40	187
$GAMAPbI_3$	IVC	3D	1.2	Ga/PVK/Au	1.3×10^{-2}	23000	16.9		8	184
$MAPbBr_{2.94}Cl_{0.06}$	ITC	3D	1	Cr/C60/BCP/PVK/Cr	1.8×10^{-2}	84000	7.6	60	8	200
$(3AMPY)Pb_2I_6$	STL	3D		Ga/PVK/Au	1.2×10^{-4}	207			50	201
$MAPbX_3$	Solution-processed epitaxial growth	3D	7.55	Gd, Ag/PVK/Au	1.29×10^{-3}	1580		66	140	202
$FA_{0.55}MA_{0.45}PbI_3$	Two-step crystal growth process	3D	800	ITO/PTAA/PVK/C60/BCP/Cu	2.9×10^{-3}	87000	27.7	0	50	203
$(CH_3OC_3H_9N)_2CsPb_2Br_7$	STL	Quasi-2D		Au/PVKAu	3.2×10^{-3}	410		0	80	189
$BA_2EA_2Pb_3Br_{10}$	STL	2D	2	Au/PVK/Au	1.0×10^{-2}	6800	5500	5	70	188
$(FPEA)_2PbI_4$	STL	2D	1.5	Au/PVK/BCP/Cr	5.1×10^{-4}	3402	23	133.33	120	190
$FAPbBr_3$/F-PEA_2PbBr_4	STL	3D/2D	2	Au/PVK/C60/NCP/Cr	2.42×10^{-3}		55	10	120	191
$MAPbI_3$	IVC	3D		Au/PVK/Au (lateral)		7.1×10^{5}	1.5	100	50	186
$Cs_{0.1}FA_{0.9}PbI_3$	Solution-processed uniform-cooling method	3D		Au/PVK/Au (lateral)		2772.1		150	>10	204
$(BDA)PbI_4$	STL	2D		Au/PVK/Au (lateral)	4.43×10^{-4}	242	430	310	40	176
$CsPbI_3$	STL	1D	0.25	Au/PVK/Au (lateral)	3.63×10^{-3}	2370		4.17	50	205

https://doi.org/10.1021/acs.chemmater.2c03505
Chem. Mater. 2023, 35, 2683−2712

detectors. Recently, Dong et al. employed a simple atomic surface passivation strategy to decrease the defects on the crystal surface using MAI (Figure 20e).[186] The surface treatment significantly increased the ion migration activation energy of the $MAPbI_3$ SCs, effectively suppressing the formation of metal halide defects without introducing additional movable ions. Thus, the dark current stability of the devices was significantly improved with a high electric field of 100 V mm^{-1}. Under continuous X-ray irradiation up to 50 keV, the detectors registered a sensitivity as high as 7.1×10^5 $\mu C\ Gy_{air}^{-1}\ cm^{-2}$ and a detection limit as low as 1.5 $nGy_{air}\ s^{-1}$. On the other hand, Liu et al. successfully incorporated smaller MA^+ and Cs^+ cations and Br^- anions into the $FAPbI_3$ lattice, which relaxed the lattice stress and decreased ion migration.[187] Perovskite $FA_{0.85}MA_{0.1}Cs_{0.05}PbI_{2.55}Br_{0.4}$ SCs (FAMAC SCs) exhibited high hardness, low trap density, long carrier lifetime, long diffusion length, high charge mobility, and excellent thermal stability. The value of S was as high as 3.5 (±0.2) × 10^6 $\mu C\ Gy_{air}^{-1}\ cm^{-2}$. Additionally, the crystal detectors exhibited a low detection limit (42 $nGy_{air}\ s^{-1}$) and stable dark current and photocurrent response. High-contrast X-ray images were also produced using the fabricated detector.

Low-dimensional perovskite crystals with low ion migration exhibit great potential for X-ray detection. In 2019, Luo et al. developed a high-performance 2D hybrid halide perovskite, $(C_4H_9NH_3)_2(C_2H_5NH_3)_2Pb_3Br_{10}$, with ferroelectric properties (Ps = 5 $\mu C\ cm^{-2}$).[188] Under a low operating voltage, the X-ray sensitivity of the device was as high as 6.8×10^3 $\mu C\ Gy_{air}^{-1}\ cm^{-2}$, more than 300-times that of the most advanced α-Se X-ray detector. The study explored the development and applicability of perovskite ferroelectric materials for high-performance optoelectronic devices. Soon after, they produced a quasi-2D ferroelectric material, $(CH_3OC_3H_9N)_2CsPb_2Br_7$, which exhibited a special volume photovoltaic effect by reconstructing the dimensions of a pure 2D monolayer perovskite, $(CH_3OC_3H_9N)_2PbBr_4$.[189] High-sensitivity X-ray photon self-driving detection was achieved using the fabricated device based on the quasi-2D double-layer hybrid ferroelectric perovskite. At zero bias voltage, the sensitivity was as high as 410 $\mu C\ Gy_{air}^{-1}\ cm^{-2}$. Yang et al. produced highly sensitive hard X-ray detectors based on 2D fluorophenyletherammonium lead iodide ($(F\text{-}PEA)_2PbI_4$) crystals.[190] Supramolecular electrostatic interactions were formed between the adjacent benzene rings, effectively suppressing the ion migration. The bulk resistivity of the crystals was 1.36×10^{12} Ω cm, which was beneficial for decreasing the noise current for hard X-ray detection. The $(F\text{-}PEA)_2PbI_4$ single-crystal detector exhibited a sensitivity of 3402 $\mu C\ Gy_{air}^{-1}\ cm^{-2}$ to 120 keV hard X-rays. On the other hand, the X-ray detection limit was 23 $nGy_{air}\ s^{-1}$. Clear X-ray images were obtained at low doses, outperforming dominant scintillators in commercial digital radiographic systems. In addition, Yang et al. obtained a 2D/3D crystal heterojunction by replacing some of the FA^+ cations with long organic cations.[191] This heterojunction efficiently inhibited ion migration, prevented the volatilization of the FA+ cations, decreased surface defects, and improved the device's performance. The optimal device based on the $(F\text{-}PEA_2PbBr_4)/(FAPbBr_3)$ crystal heterojunction reduced the ion mobility and increased the bulk resistivity by a factor of 1.5 and 2, respectively. At 120 keV, the hard X-ray detection limit was as low as 55 $nGy_{air}\ s^{-1}$, which was better than that of the $FAPbBr_3$ control sample (250 $nGy_{air}\ s^{-1}$). Finally, Figure 20f outlines the materials and device performance of the previously reported perovskite crystal X-ray detectors. The corresponding materials, crystal growth methods, device structures, and parameters are summarized in Table 6.

7. CONCLUSION AND OUTLOOK

Crystal growth techniques and the quality of perovskite single crystals have been continuously improved. In most cases, perovskite single crystals exhibit more potentials in improving the optoelectronic device performance. We believe that perovskite single crystals can exhibit unique roles in the commercialization of optoelectronic devices. Currently, many methods can be used for growing perovskite single crystals. If they are to be used in commercial devices, a variety of factors, including the purity, the quality, the duration and the cost of synthesis, should be considered. In addition, different growth methods should be chosen according to the difference in crystal composition. The solution temperature lowering method (STL) of liquid phase is the most popular choice for organic−inorganic hybrid metal halide perovskite single crystals due to its relatively simpler operation and lower cost. For inorganic metal halide perovskite single crystals preparing, Bridgman growth method is more suitable because the growth temperature can be easily adjusted based on which raw materials are chosen and the desired crystal shape can be easily produced in this method. It is challenging to use other solution-processing methods because the solubility of inorganic precursors in the liquid phase largely depends on the solvent, and it is difficult to avoid the phase separation of such perovskites.

In terms of promoting the performance improvement and commercialization of optoelectronic devices, we believe the future research on the applications of perovskite single crystals should focus on the following areas. (1) Although there are a lot of methods for the growth of single crystals, different methods have the different disadvantages, such as long preparation periods and high cost. Therefore, an efficient and highly controllable process for the growth of perovskite SCs needs to be further developed. (2) Because of the difficult combination of high-quality and large-sized perovskite single crystals and optoelectronic devices with excellent performance, most of the current research respectively focus on these two processes. If these two processes are perfectly combined, it will further promote the commercialization of optoelectronic devices based on perovskite materials. (3) To date, perovskite single crystals still exhibit poor stability. This can be addressed by using inorganic cations instead of organic cations, such as MA^+ and FA^+. However, the quality of all-inorganic perovskite single crystals is still not comparable to those of organic perovskites. Furthermore, Pb-based perovskites show better photoelectric performance compared to other metal ions. However, the Pb^{2+} ions are toxic to human health, which would hinder the commercial development of Pb-based optoelectronic devices. Therefore, it is necessary to continuously optimize the choosing of metal ions in perovskite materials.

Therefore, crystal growth techniques should be continuously explored and enhanced to produce large, high-quality single crystals. This can help better comprehend the fundamental properties of perovskites and develop more applications of the perovskite single crystals.

https://doi.org/10.1021/acs.chemmater.2c03505
Chem. Mater. 2023, 35, 2683−2712

AUTHOR INFORMATION

Corresponding Authors

Antonio Abate − *Helmholtz-Zentrum Berlin für Materialien und Energie GmbH, 14109 Berlin, Germany;* orcid.org/0000-0002-3012-3541; Email: antonio.abate@helmholtz-berlin.de

Kui Zhao − *Key Laboratory of Applied Surface and Colloid Chemistry, Ministry of Education, Shaanxi Key Laboratory for Advanced Energy Devices, Shaanxi Engineering Lab for Advanced Energy Technology, Institute for Advanced Energy Materials, School of Materials Science and Engineering, Shaanxi Normal University, Xi'an, Shaanxi 710119, PR China;* orcid.org/0000-0002-9512-0405; Email: zhaok@snnu.edu.cn

Yue Hu − *Wuhan National Laboratory for Optoelectronics, Huazhong University of Science and Technology, Wuhan, Hubei 430074, PR China; School of Chemistry, University of Edinburgh, Edinburgh EH9 3FJ, U.K.;* orcid.org/0000-0003-0163-4702; Email: Yue.Hu@ed.ac.uk

Authors

Jiakai Yan − *Wuhan National Laboratory for Optoelectronics, Huazhong University of Science and Technology, Wuhan, Hubei 430074, PR China*

Haojin Li − *Key Laboratory of Applied Surface and Colloid Chemistry, Ministry of Education, Shaanxi Key Laboratory for Advanced Energy Devices, Shaanxi Engineering Lab for Advanced Energy Technology, Institute for Advanced Energy Materials, School of Materials Science and Engineering, Shaanxi Normal University, Xi'an, Shaanxi 710119, PR China*

Mahmoud Hussein Aldamasy − *Helmholtz-Zentrum Berlin für Materialien und Energie GmbH, 14109 Berlin, Germany*

Chiara Frasca − *Helmholtz-Zentrum Berlin für Materialien und Energie GmbH, 14109 Berlin, Germany*

Complete contact information is available at: https://pubs.acs.org/10.1021/acs.chemmater.2c03505

Notes

The authors declare no competing financial interest.

ACKNOWLEDGMENTS

Jiakai Yan and Haojin Li contributed equally to this work. The authors acknowledge financial support from the National Natural Science Foundation of China (Grant Nos. 22075094, 51933010, 61974085), and the Fundamental Research Funds for the Central Universities.

REFERENCES

(1) Poglitsch, A.; Weber, D. Dynamic disorder in methylammoniumtrihalogenoplumbates (II) observed by millimeter-wave spectroscopy. *J. Chem. Phys.* **1987**, *87* (11), 6373−6378.

(2) Billing, D. G.; Lemmerer, A. Synthesis, characterization and phase transitions in the inorganic-organic layered perovskite-type hybrids $[(C_nH_{2n+1}NH_3)_2PbI_4]$, n = 4, 5 and 6. *Acta Crystallogr. B* **2007**, *63* (5), 735−47.

(3) Chae, J.; Dong, Q.; Huang, J.; Centrone, A. Chloride incorporation process in $CH_3NH_3PbI_{3-x}Cl_x$ perovskites via nanoscale bandgap maps. *Nano Lett.* **2015**, *15* (12), 8114−8121.

(4) Huang, Y.; Li, L.; Liu, Z.; Jiao, H.; He, Y.; Wang, X.; Zhu, R.; Wang, D.; Sun, J.; Chen, Q.; Zhou, H. The intrinsic properties of $FA_{(1-x)}MA_xPbI_3$ perovskite single crystals. *Journal of Materials Chemistry A* **2017**, *5* (18), 8537−8544.

(5) Lemmerer, A.; Billing, D. G. Effect of heteroatoms in the inorganic−organic layered perovskite-type hybrids $[(ZC_nH_{2n}NH_3)_2PbI_4]$, n = 2, 3, 4, 5, 6; Z = OH, Br and I; and $[(H_3NC_2H_4S_2C_2H_4NH_3)PbI_4]$. *CrystEngComm* **2010**, *12* (4), 1290−1301.

(6) Li, X.; Hoffman, J.; Ke, W.; Chen, M.; Tsai, H.; Nie, W.; Mohite, A. D.; Kepenekian, M.; Katan, C.; Even, J.; Wasielewski, M. R.; Stoumpos, C. C.; Kanatzidis, M. G. Two-Dimensional Halide Perovskites Incorporating Straight Chain Symmetric Diammonium Ions,$(NH_3C_mH_{2m}NH_3)(CH_3NH_3)_{n-1}Pb_nI_{3n+1}$ (m = 4−9; n = 1−4). *J. Am. Chem. Soc.* **2018**, *140* (38), 12226−12238.

(7) Paritmongkol, W.; Dahod, N. S.; Stollmann, A.; Mao, N.; Settens, C.; Zheng, S.-L.; Tisdale, W. A. Synthetic variation and structural trends in layered two-dimensional alkylammonium lead halide perovskites. *Chem. Mater.* **2019**, *31* (15), 5592−5607.

(8) Safdari, M.; Svensson, P. H.; Hoang, M. T.; Oh, I.; Kloo, L.; Gardner, J. M. Layered 2D alkyldiammonium lead iodide perovskites: synthesis, characterization, and use in solar cells. *Journal of Materials Chemistry A* **2016**, *4* (40), 15638−15646.

(9) Soe, C. M. M.; Stoumpos, C. C.; Kepenekian, M.; Traore, B.; Tsai, H.; Nie, W.; Wang, B.; Katan, C.; Seshadri, R.; Mohite, A. D.; Even, J.; Marks, T. J.; Kanatzidis, M. G. New Type of 2D Perovskites with Alternating Cations in the Interlayer Space, $(C(NH_2)_3)(CH_3NH_3)_nPb_nI_{3n+1}$: Structure, Properties, and Photovoltaic Performance. *J. Am. Chem. Soc.* **2017**, *139* (45), 16297−16309.

(10) Stoumpos, C. C.; Cao, D. H.; Clark, D. J.; Young, J.; Rondinelli, J. M.; Jang, J. I.; Hupp, J. T.; Kanatzidis, M. G. Ruddlesden−Popper Hybrid Lead Iodide Perovskite 2D Homologous Semiconductors. *Chem. Mater.* **2016**, *28* (8), 2852−2867.

(11) Stoumpos, C. C.; Frazer, L.; Clark, D. J.; Kim, Y. S.; Rhim, S. H.; Freeman, A. J.; Ketterson, J. B.; Jang, J. I.; Kanatzidis, M. G. Hybrid germanium iodide perovskite semiconductors: active lone pairs, structural distortions, direct and indirect energy gaps, and strong nonlinear optical properties. *J. Am. Chem. Soc.* **2015**, *137* (21), 6804−19.

(12) Su, J.; Chen, D. P.; Lin, C. T. Growth of large $CH_3NH_3PbX_3$ (X = I, Br) single crystals in solution. *J. Cryst. Growth* **2015**, *422*, 75−79.

(13) Xu, Z.; Li, H.; Zhao, H.; Fu, Q.; Tao, H.; Wang, S.; Ma, Z.; Ding, J.; Ma, Y.; Han, Y. Optimizing optoelectronic performances by controlling halide compositions of $MAPb(Cl_xI_{1-x})_3$ single crystals. *CrystEngComm* **2019**, *21* (28), 4169−4174.

(14) Dang, Y.; Liu, Y.; Sun, Y.; Yuan, D.; Liu, X.; Lu, W.; Liu, G.; Xia, H.; Tao, X. Bulk crystal growth of hybrid perovskite material $CH_3NH_3PbI_3$. *CrystEngComm* **2015**, *17* (3), 665−670.

(15) Lian, Z.; Yan, Q.; Lv, Q.; Wang, Y.; Liu, L.; Zhang, L.; Pan, S.; Li, Q.; Wang, L.; Sun, J. L. High-performance planar-type photodetector on (100) facet of $MAPbI_3$ single crystal. *Sci. Rep.* **2015**, *5* (2015), 16563−16572.

(16) Zhou, Y.; Li, C.; Wang, Y.; Du, X.; Liu, P.; Xie, W. Preparation and characterization of high-quality perovskite $CH_3NH_3PbX_3$ (I, Br) single crystal. *IOP Conference Series: Materials Science and Engineering* **2017**, *167* (2017), 012019−012025.

(17) Ju, D.; Dang, Y.; Zhu, Z.; Liu, H.; Chueh, C.-C.; Li, X.; Wang, L.; Hu, X.; Jen, A. K. Y.; Tao, X. Tunable band gap and long carrier recombination lifetime of stable mixed $CH_3NH_3Pb_xSn_{1-x}Br_3$ single crystals. *Chem. Mater.* **2018**, *30* (5), 1556−1565.

(18) Lian, Z.; Yan, Q.; Gao, T.; Ding, J.; Lv, Q.; Ning, C.; Li, Q.; Sun, J. L. Perovskite $CH_3NH_3PbI_3(Cl)$ single crystals: rapid solution growth, unparalleled crystalline quality, and low trap density toward 108 cm^{-3}. *J. Am. Chem. Soc.* **2016**, *138* (30), 9409−9412.

(19) Peng, J.; Xia, C. Q.; Xu, Y.; Li, R.; Cui, L.; Clegg, J. K.; Herz, L. M.; Johnston, M. B.; Lin, Q. Crystallization of $CsPbBr_3$ single crystals in water for X-ray detection. *Nat. Commun.* **2021**, *12* (1), 1531−1540.

(20) Yoo, J. J.; Seo, G.; Chua, M. R.; Park, T. G.; Lu, Y.; Rotermund, F.; Kim, Y. K.; Moon, C. S.; Jeon, N. J.; Correa-Baena, J. P.; Bulovic, V.; Shin, S. S.; Bawendi, M. G.; Seo, J. Efficient perovskite solar cells via improved carrier management. *Nature* **2021**, *590* (7847), 587−593.

(21) Stranks, S. D.; Eperon, G. E.; Grancini, G.; Menelaou, C.; Alcocer, M. J.; Leijtens, T.; Herz, L. M.; Petrozza, A.; Snaith, H. J. Electron-hole diffusion lengths exceeding 1 micrometer in an organometal trihalide perovskite absorber. *Science* **2013**, *342* (6156), 341−344.

(22) Dong, Q.; Fang, Y.; Shao, Y.; Mulligan, P.; Qiu, J.; Cao, L.; Huang, J. Electron-hole diffusion lengths > 175 μm in solution-grown $CH_3NH_3PbI_3$ single crystals. *Science* **2015**, *347* (6225), 967−970.

(23) Shi, D.; Adinolfi, V.; Comin, R.; Yuan, M.; Alarousu, E.; Buin, A.; Chen, Y.; Hoogland, S.; Rothenberger, A.; Katsiev, K.; et al. Low trap-state density and long carrier diffusion in organolead trihalide perovskite single crystals. *Science* **2015**, *347* (6221), 519−522.

(24) Kojima, A.; Teshima, K.; Shirai, Y.; Miyasaka, T. Organometal halide perovskites as visible-light sensitizers for photovoltaic cells. *J. Am. Chem. Soc.* **2009**, *131* (17), 6050−6051.

(25) Zhu, H.; Fu, Y.; Meng, F.; Wu, X.; Gong, Z.; Ding, Q.; Gustafsson, M. V.; Trinh, M. T.; Jin, S.; Zhu, X. Y. Lead halide perovskite nanowire lasers with low lasing thresholds and high quality factors. *Nat. Mater.* **2015**, *14* (6), 636−642.

(26) Zhou, H.; Yuan, S.; Wang, X.; Xu, T.; Wang, X.; Li, H.; Zheng, W.; Fan, P.; Li, Y.; Sun, L.; Pan, A. Vapor growth and tunable lasing of band gap engineered cesium lead halide perovskite micro/nanorods with triangular cross section. *ACS Nano* **2017**, *11* (2), 1189−1195.

(27) Xing, G.; Mathews, N.; Lim, S. S.; Yantara, N.; Liu, X.; Sabba, D.; Gratzel, M.; Mhaisalkar, S.; Sum, T. C. Low-temperature solution-processed wavelength-tunable perovskites for lasing. *Nat. Mater.* **2014**, *13* (5), 476−680.

(28) Li, M.; Wei, Q.; Muduli, S. K.; Yantara, N.; Xu, Q.; Mathews, N.; Mhaisalkar, S. G.; Xing, G.; Sum, T. C. Enhanced exciton and photon confinement in Ruddlesden-Popper perovskite microplatelets for highly stable low-threshold polarized lasing. *Adv. Mater.* **2018**, *30* (23), 1707235−1707242.

(29) Lee, C. C.; Iskandar, J.; Akbar, A. K.; Cheng, H.-M.; Liu, S. W. Controllable crystallization based on the aromatic ammonium additive for efficiently near-infrared perovskite light-emitting diodes. *Org. Electron.* **2021**, *99* (2021), 106327−106333.

(30) Chen, Z.; Zhang, C.; Jiang, X. F.; Liu, M.; Xia, R.; Shi, T.; Chen, D.; Xue, Q.; Zhao, Y. J.; Su, S.; Yip, H. L.; Cao, Y. High-performance color-tunable perovskite light emitting devices through structural modulation from bulk to layered film. *Adv. Mater.* **2017**, *29* (8), 1603157−1603164.

(31) Sessolo, M.; Gil-Escrig, L.; Longo, G.; Bolink, H. J. Perovskite luminescent materials. *Topics in Current Chemistry* **2016**, *374* (4), 52−79.

(32) Zhevstovskikh, I. V.; Averkiev, N. S.; Sarychev, M. N.; Semenova, O. I.; Tereshchenko, O. E. Low-temperature luminescence in organic-inorganic lead iodide perovskite single crystals. *J. Phys. D: Appl. Phys.* **2022**, *55* (9), 095105−095114.

(33) Yang, Z.; Xu, Q.; Wang, X.; Lu, J.; Wang, H.; Li, F.; Zhang, L.; Hu, G.; Pan, C. Large and ultrastable all-Inorganic $CsPbBr_3$ monocrystalline films: low-temperature growth and application for high-performance photodetectors. *Adv. Mater.* **2018**, *30* (44), 1802110−1802119.

(34) Saidaminov, M. I.; Adinolfi, V.; Comin, R.; Abdelhady, A. L.; Peng, W.; Dursun, I.; Yuan, M.; Hoogland, S.; Sargent, E. H.; Bakr, O. M. Planar-integrated single-crystalline perovskite photodetectors. *Nat. Commun.* **2015**, *6* (1), 8724−8730.

(35) Ding, J.; Du, S.; Zuo, Z.; Zhao, Y.; Cui, H.; Zhan, X. High detectivity and rapid response in perovskite $CsPbBr_3$ single-crystal photodetector. *J. Phys. Chem. C* **2017**, *121* (9), 4917−4923.

(36) Fan, Z.; Liu, J.; Zuo, W.; Liu, G.; He, X.; Luo, K.; Ye, Q.; Liao, C. Mixed-Cation $MA_xCs_{1-x}PbBr_3$ Perovskite Single Crystals with Composition Management for High-Sensitivity X-Ray Detection. *physica status solidi RRL* **2020**, *14* (10), 2000226.

(37) Wei, H.; Fang, Y.; Mulligan, P.; Chuirazzi, W.; Fang, H.-H.; Wang, C.; Ecker, B. R.; Gao, Y.; Loi, M. A.; Cao, L.; Huang, J. Sensitive X-ray detectors made of methylammonium lead tribromide perovskite single crystals. *Nat. Photonics* **2016**, *10* (5), 333−339.

(38) Jiang, Q.; Zhao, Y.; Zhang, X.; Yang, X.; Chen, Y.; Chu, Z.; Ye, Q.; Li, X.; Yin, Z.; You, J. Surface passivation of perovskite film for efficient solar cells. *Nat. Photonics* **2019**, *13* (7), 460−466.

(39) Bai, Y.; Lin, Y.; Ren, L.; Shi, X.; Strounina, E.; Deng, Y.; Wang, Q.; Fang, Y.; Zheng, X.; Lin, Y.; Chen, Z.-G.; Du, Y.; Wang, L.; Huang, J. Oligomeric silica-wrapped perovskites enable synchronous defect passivation and grain stabilization for efficient and stable perovskite photovoltaics. *ACS Energy Letters* **2019**, *4* (6), 1231−1240.

(40) Wang, K.; Tang, M. C.; Dang, H. X.; Munir, R.; Barrit, D.; De Bastiani, M.; Aydin, E.; Smilgies, D. M.; De Wolf, S.; Amassian, A. Kinetic stabilization of the sol-gel state in perovskites enables facile processing of high-efficiency solar cells. *Adv. Mater.* **2019**, *31* (32), 1808357−1808367.

(41) Yuan, Y.; Huang, J. Ion migration in organometal trihalide perovskite and its impact on photovoltaic efficiency and stability. *Acc. Chem. Res.* **2016**, *49* (2), 286−293.

(42) Murgulov, V.; Daub, M.; Hillebrecht, H.; Fiederle, M.; Franc, J.; Dedič, V. Growth and Characterization of Radiation Sensors Based on Single Crystals of Hybrid Metal−Organic Methylammonium Lead Bromide and Iodide Perovskite. *Crystal Research Technology* **2020**, *55* (11), 2000112.

(43) Fang, H.-H.; Adjokatse, S.; Wei, H.; Yang, J.; Blake, G. R.; Huang, J.; Even, J.; Loi, M. A. Ultrahigh sensitivity of methylammonium lead tribromide perovskite single crystals to environmental gases. *Science Advances* **2016**, *2* (7), No. e1600534.

(44) Yang, Y.; Yan, Y.; Yang, M.; Choi, S.; Zhu, K.; Luther, J. M.; Beard, M. C. Low surface recombination velocity in solution-grown $CH_3NH_3PbBr_3$ perovskite single crystal. *Nat. Commun.* **2015**, *6*, 7961.

(45) Wells, H. L. Über die cäsium-und kalium-bleihalogenide. *Zeitschrift für anorganische Chemie* **1893**, *3* (1), 195−210.

(46) MØller, C. Crystal structure and photoconductivity of caesium plumbohalides. *Nature* **1958**, *182* (4647), 1436−1436.

(47) Arend, H.; Huber, W.; Mischgofsky, F.; Richter-Van Leeuwen, G. Layer perovskites of the $(C_nH_{2n+1}NH_3)_2MX_4$ and $NH_3(CH_2)_mNH_3MX_4$ families with M= Cd, Cu, Fe, Mn or Pd and X= Cl or Br: Importance, solubilities and simple growth techniques. *J. Cryst. Growth* **1978**, *43* (2), 213−223.

(48) Mitzi, D. B.; Feild, C.; Schlesinger, Z.; Laibowitz, R. Transport, optical, and magnetic properties of the conducting halide perovskite CH3NH3SnI3. *J. Solid State Chem.* **1995**, *114* (1), 159−163.

(49) Saidaminov, M. I.; Abdelhady, A. L.; Murali, B.; Alarousu, E.; Burlakov, V. M.; Peng, W.; Dursun, I.; Wang, L.; He, Y.; Maculan, G.; Goriely, A.; Wu, T.; Mohammed, O. F.; Bakr, O. M. High-quality bulk hybrid perovskite single crystals within minutes by inverse temperature crystallization. *Nat. Commun.* **2015**, *6*, 7586.

(50) Stoumpos, C. C.; Malliakas, C. D.; Peters, J. A.; Liu, Z.; Sebastian, M.; Im, J.; Chasapis, T. C.; Wibowo, A. C.; Chung, D. Y.; Freeman, A. J.; Wessels, B. W.; Kanatzidis, M. G. Crystal Growth of the Perovskite Semiconductor $CsPbBr_3$: A New Material for High-Energy Radiation Detection. *Cryst. Growth Des.* **2013**, *13* (7), 2722−2727.

(51) Kaslasi, H.; Feldman, Y.; Rakita, Y.; Cahen, D.; Hodes, G. Single-crystal growth and thermal stability of $(CH_3NH_3)_{1-x}Cs_xPbBr_3$. *Cryst. Growth Des.* **2020**, *20* (7), 4366−4374.

(52) Dang, Y.; Ju, D.; Wang, L.; Tao, X. Recent progress in the synthesis of hybrid halide perovskite single crystals. *CrystEngComm* **2016**, *18* (24), 4476−4484.

(53) Babu, R.; Giribabu, L.; Singh, S. P. Recent Advances in Halide-Based Perovskite Crystals and Their Optoelectronic Applications. *Cryst. Growth Des.* **2018**, *18* (4), 2645−2664.

(54) Mao, L.; Stoumpos, C. C.; Kanatzidis, M. G. Two-Dimensional Hybrid Halide Perovskites: Principles and Promises. *J. Am. Chem. Soc.* **2019**, *141* (3), 1171−1190.

(55) Chen, Y.; Sun, Y.; Peng, J.; Tang, J.; Zheng, K.; Liang, Z. 2D Ruddlesden-Popper Perovskites for Optoelectronics. *Adv. Mater.* **2018**, *30* (2), 1703487.

(56) Zhang, F.; Lu, H.; Tong, J.; Berry, J. J.; Beard, M. C.; Zhu, K. Advances in two-dimensional organic−inorganic hybrid perovskites. *Energy Environ. Sci.* **2020**, *13* (4), 1154−1186.

(57) Criado, C. L.; Reséndez, R. M. Formación de partículas nanométricas en soluciones sobresaturadas. *CIENCIA-UANL* **2008**, *11* (3), 6.
(58) Kelton, K. F. Crystal Nucleation in Liquids and Glasses. In *Solid State Physics*; Ehrenreich, H., Turnbull, D., Eds.; Academic Press, 1991; Vol. *45*, pp 75−177.
(59) Strey, R.; Wagner, P. E.; Viisanen, Y. The Problem of Measuring Homogeneous Nucleation Rates and the Molecular Contents of Nuclei: Progress in the Form of Nucleation Pulse Measurements. *J. Phys. Chem.* **1994**, *98* (32), 7748−7758.
(60) LaMer, V. K.; Dinegar, R. H. Theory, production and mechanism of formation of monodispersed hydrosols. *J. Am. Chem. Soc.* **1950**, *72* (11), 4847−4854.
(61) Thanh, N. T.; Maclean, N.; Mahiddine, S. Mechanisms of nucleation and growth of nanoparticles in solution. *Chem. Rev.* **2014**, *114* (15), 7610−30.
(62) Kwon, S. G.; Hyeon, T. Formation mechanisms of uniform nanocrystals via hot-injection and heat-up methods. *Small* **2011**, *7* (19), 2685−702.
(63) Liu, Y.; Zhang, Y.; Yang, Z.; Ye, H.; Feng, J.; Xu, Z.; Zhang, X.; Munir, R.; Liu, J.; Zuo, P.; Li, Q.; Hu, M.; Meng, L.; Wang, K.; Smilgies, D. M.; Zhao, G.; Xu, H.; Yang, Z.; Amassian, A.; Li, J.; Zhao, K.; Liu, S. F. Multi-inch single-crystalline perovskite membrane for high-detectivity flexible photosensors. *Nat. Commun.* **2018**, *9* (1), 5302.
(64) Dash, J. G. Clustering and percolation transitions in helium and other thin films. *Phys. Rev. B* **1977**, *15* (6), 3136−3146.
(65) Liu, Y.; Zhang, Y.; Yang, Z.; Feng, J.; Xu, Z.; Li, Q.; Hu, M.; Ye, H.; Zhang, X.; Liu, M.; Zhao, K.; Liu, S. Low-temperature-gradient crystallization for multi-inch high-quality perovskite single crystals for record performance photodetectors. *Mater. Today* **2019**, *22*, 67−75.
(66) Sugimoto, T.; Shiba, F.; Sekiguchi, T.; Itoh, H. Spontaneous nucleation of monodisperse silver halide particles from homogeneous gelatin solution I: silver chloride. *Colloids Surfaces A: Physicochemical Engineering Aspects* **2000**, *164* (2−3), 183−203.
(67) Yec, C. C.; Zeng, H. C. Synthesis of complex nanomaterials via Ostwald ripening. *J. Mater. Chem. A* **2014**, *2* (14), 4843−4851.
(68) Lifshitz, I. M.; Slyozov, V. V. The kinetics of precipitation from supersaturated solid solutions. *Journal of physics chemistry of solids* **1961**, *19* (1−2), 35−50.
(69) Lee, W.-r.; Kim, M. G.; Choi, J.-r.; Park, J.-I.; Ko, S. J.; Oh, S. J.; Cheon, J. Redox− transmetalation process as a generalized synthetic strategy for core− shell magnetic nanoparticles. *J. Am. Chem. Soc.* **2005**, *127* (46), 16090−16097.
(70) Watzky, M. A.; Finney, E. E.; Finke, R. G. Transition-metal nanocluster size vs formation time and the catalytically effective nucleus number: a mechanism-based treatment. *J. Am. Chem. Soc.* **2008**, *130* (36), 11959−11969.
(71) Penn, R. L.; Banfield, J. F. Morphology development and crystal growth in nanocrystalline aggregates under hydrothermal conditions: Insights from titania. *Geochimica et cosmochimica acta* **1999**, *63* (10), 1549−1557.
(72) Zheng, H.; Smith, R. K.; Jun, Y.-w.; Kisielowski, C.; Dahmen, U.; Alivisatos, A. P. Observation of single colloidal platinum nanocrystal growth trajectories. *Science* **2009**, *324* (5932), 1309−1312.
(73) Su, J.; Chen, D. P.; Lin, C. T. Growth of large $CH_3NH_3PbX_3$ (X = I, Br) single crystals in solution. *J. Cryst. Growth* **2015**, *422* (2015), 75−79.
(74) Li, X.; Hoffman, J.; Ke, W.; Chen, M.; Tsai, H.; Nie, W.; Mohite, A. D.; Kepenekian, M.; Katan, C.; Even, J.; Wasielewski, M. R.; Stoumpos, C. C.; Kanatzidis, M. G. Two-Dimensional Halide Perovskites Incorporating Straight Chain Symmetric Diammonium Ions, $(NH_3C_mH_{2m}NH_3)(CH_3NH_3)_{n-1}Pb_nI_{3n+1}$ (m = 4−9; n = 1−4). *J. Am. Chem. Soc.* **2018**, *140* (38), 12226−12238.
(75) Li, P.; Liu, X.; Zhang, Y.; Liang, C.; Chen, G.; Li, F.; Su, M.; Xing, G.; Tao, X.; Song, Y. Low-Dimensional Dion-Jacobson-Phase Lead-Free Perovskites for High-Performance Photovoltaics with Improved Stability. *Angew. Chem., Int. Ed. Engl.* **2020**, *59* (17), 6909−6914.
(76) Dang, Y.; Zhou, Y.; Liu, X.; Ju, D.; Xia, S.; Xia, H.; Tao, X. Formation of Hybrid Perovskite Tin Iodide Single Crystals by Top-Seeded Solution Growth. *Angew. Chem., Int. Ed. Engl.* **2016**, *55* (10), 3447−3450.
(77) Dang, Y.; Wei, J.; Liu, X.; Wang, X.; Xu, K.; Lei, M.; Hu, W.; Tao, X. Layered hybrid perovskite solar cells based on single-crystalline precursor solutions with superior reproducibility. *Sustainable Energy & Fuels* **2018**, *2* (10), 2237−2243.
(78) Li, J.; Han, Z.; Gu, Y.; Yu, D.; Liu, J.; Hu, D.; Xu, X.; Zeng, H. Perovskite Single Crystals: Synthesis, Optoelectronic Properties, and Application. *Adv. Funct. Mater.* **2021**, *31* (11), 2008684.
(79) Dang, Y.; Zhong, C.; Zhang, G.; Ju, D.; Wang, L.; Xia, S.; Xia, H.; Tao, X. Crystallographic Investigations into Properties of Acentric Hybrid Perovskite Single Crystals $NH(CH_3)_3SnX_3$ (X = Cl, Br). *Chem. Mater.* **2016**, *28* (19), 6968−6974.
(80) Vincent, B. R.; Robertson, K. N.; Cameron, T. S.; Knop, O. Alkylammonium lead halides. Part 1. Isolated PbI_6^{4-} ions in $(CH_3NH_3)_4PbI_6$• $2H_2O$. *Canadian journal of chemistry* **1987**, *65* (5), 1042−1046.
(81) Saidaminov, M. I.; Abdelhady, A. L.; Maculan, G.; Bakr, O. M. Retrograde solubility of formamidinium and methylammonium lead halide perovskites enabling rapid single crystal growth. *Chem. Commun.* **2015**, *51* (100), 17658−17661.
(82) Nayak, P. K.; Moore, D. T.; Wenger, B.; Nayak, S.; Haghighirad, A. A.; Fineberg, A.; Noel, N. K.; Reid, O. G.; Rumbles, G.; Kukura, P.; Vincent, K. A.; Snaith, H. J. Mechanism for rapid growth of organic−inorganic halide perovskite crystals. *Nat. Commun.* **2016**, *7* (1), 13303.
(83) Wang, X.; Huang, Y.; Lei, W.; Li, Q.; Zhang, X.; Khan, Q.; Wang, B. Asymmetrical Photodetection Response of Methylammonium Lead Bromide Perovskite Single Crystal. *Crystal Research and Technology* **2017**, *52* (9), 1700115.
(84) Liu, Y.; Yang, Z.; Cui, D.; Ren, X.; Sun, J.; Liu, X.; Zhang, J.; Wei, Q.; Fan, H.; Yu, F.; Zhang, X.; Zhao, C.; Liu, S. F. Two-inch-sized perovskite $CH_3NH_3PbX_3$ (X = Cl, Br, I) crystals: Growth and Characterization. *Adv. Mater.* **2015**, *27* (35), 5176−5183.
(85) Hsu, H. P.; Li, L. C.; Shellaiah, M.; Sun, K. W. Structural, Photophysical, and Electronic Properties of $CH_3NH_3PbCl_3$ Single Crystals. *Sci. Rep.* **2019**, *9* (1), 13311.
(86) Han, Q.; Bae, S. H.; Sun, P.; Hsieh, Y. T.; Yang, Y. M.; Rim, Y. S.; Zhao, H.; Chen, Q.; Shi, W.; Li, G.; Yang, Y. Single crystal formamidinium lead Iodide ($FAPbI_3$): Insight into the structural, optical, and electrical properties. *Adv. Mater.* **2016**, *28* (11), 2253−2258.
(87) Li, W.-G.; Rao, H.-S.; Chen, B.-X.; Wang, X.-D.; Kuang, D.-B. A formamidinium−methylammonium lead iodide perovskite single crystal exhibiting exceptional optoelectronic properties and long-term stability. *Journal of Materials Chemistry A* **2017**, *5* (36), 19431−19438.
(88) Dirin, D. N.; Cherniukh, I.; Yakunin, S.; Shynkarenko, Y.; Kovalenko, M. V. Solution-Grown $CsPbBr_3$ Perovskite Single Crystals for Photon Detection. *Chem. Mater.* **2016**, *28* (23), 8470−8474.
(89) Saidaminov, M. I.; Haque, M. A.; Almutlaq, J.; Sarmah, S.; Miao, X.-H.; Begum, R.; Zhumekenov, A. A.; Dursun, I.; Cho, N.; Murali, B.; Mohammed, O. F.; Wu, T.; Bakr, O. M. Inorganic Lead Halide Perovskite Single Crystals: Phase-Selective Low-Temperature Growth, Carrier Transport Properties, and Self-Powered Photodetection. *Advanced Optical Materials* **2017**, *5* (2), 1600704.
(90) Wang, K.; Jing, L.; Yao, Q.; Zhang, J.; Cheng, X.; Yuan, Y.; Shang, C.; Ding, J.; Zhou, T.; Sun, H.; Zhang, W.; Li, H. Highly In-Plane Polarization-Sensitive Photodetection in $CsPbBr_3$ Single Crystal. *the Journal of Physical Chemistry Letters* **2021**, *12* (7), 1904−1910.
(91) Yang, Y.; Wu, D.; Zhang, Z.; Cao, W.; Zhao, X.; Hao, Y.; Yang, P.; Wang, J. Rapid synthesis of inorganic halide perovskite single crystals with high thermal stability. *Chem. Phys. Lett.* **2020**, *759*, 759.

(92) Mercier, N. $(HO_2C(CH_2)_3NH_3)_2(CH_3NH_3)Pb_2I_7$: a predicted non-centrosymmetrical structure built up from carboxylic acid supramolecular synthons and bilayer perovskite sheets. *CrystEngComm* **2005**, *7* (70), 429−432.

(93) Mhiri, A.; Krichen, F.; Oueslati, A.; Lhoste, J.; Goutenoire, F.; Gargouri, M.; Bulou, A. Synthesis, structural characterization and spectroscopic studies of bis tetramethylammonium hexabromostannate $[N(CH_3)_4]_2SnBr_6$. *J. Alloys Compd.* **2019**, *772* (2019), 546−556.

(94) Stoumpos, C. C.; Frazer, L.; Clark, D. J.; Kim, Y. S.; Rhim, S. H.; Freeman, A. J.; Ketterson, J. B.; Jang, J. I.; Kanatzidis, M. G. Hybrid germanium iodide perovskite semiconductors: active lone pairs, structural distortions, direct and indirect energy gaps, and strong nonlinear optical properties. *J. Am. Chem. Soc.* **2015**, *137* (21), 6804−6819.

(95) Roy, P. K.; Ulaganathan, R. K.; Raghavan, C. M.; Mhatre, S. M.; Lin, H. I.; Chen, W. L.; Chang, Y. M.; Rozhin, A.; Hsu, Y. T.; Chen, Y. F.; Sankar, R.; Chou, F. C.; Liang, C. T. Unprecedented random lasing in 2D organolead halide single-crystalline perovskite microrods. *Nanoscale* **2020**, *12* (35), 18269−18277.

(96) Yao, F.; Peng, J.; Li, R.; Li, W.; Gui, P.; Li, B.; Liu, C.; Tao, C.; Lin, Q.; Fang, G. Room-temperature liquid diffused separation induced crystallization for high-quality perovskite single crystals. *Nat. Commun.* **2020**, *11* (1), 1194−1202.

(97) Liu, Y.; Dong, Q.; Fang, Y.; Lin, Y.; Deng, Y.; Huang, J. Fast Growth of Thin $MAPbI_3$ Crystal Wafers on Aqueous Solution Surface for Efficient Lateral-Structure Perovskite Solar Cells. *Adv. Funct. Mater.* **2019**, *29* (47), 1807707.

(98) Tidhar, Y.; Edri, E.; Weissman, H.; Zohar, D.; Hodes, G.; Cahen, D.; Rybtchinski, B.; Kirmayer, S. Crystallization of methyl ammonium lead halide perovskites: implications for photovoltaic applications. *J. Am. Chem. Soc.* **2014**, *136* (38), 13249−56.

(99) Liu, X.; Zhang, H.; Zhang, B.; Dong, J.; Jie, W.; Xu, Y. Charge Transport Behavior in Solution-Grown Methylammonium Lead Tribromide Perovskite Single Crystal Using α Particles. *J. Phys. Chem. C* **2018**, *122* (26), 14355−14361.

(100) Peng, W.; Wang, L.; Murali, B.; Ho, K. T.; Bera, A.; Cho, N.; Kang, C. F.; Burlakov, V. M.; Pan, J.; Sinatra, L.; Ma, C.; Xu, W.; Shi, D.; Alarousu, E.; Goriely, A.; He, J. H.; Mohammed, O. F.; Wu, T.; Bakr, O. M. Solution-Grown Monocrystalline Hybrid Perovskite Films for Hole-Transporter-Free Solar Cells. *Adv. Mater.* **2016**, *28* (17), 3383−90.

(101) Fateev, S. A.; Petrov, A. A.; Ordinartsev, A. A.; Grishko, A. Y.; Goodilin, E. A.; Tarasov, A. B. Universal Strategy of 3D and 2D Hybrid Perovskites Single Crystal Growth via In Situ Solvent Conversion. *Chem. Mater.* **2020**, *32* (22), 9805−9812.

(102) Zuo, C.; Ding, L. Lead-free Perovskite Materials $(NH_4)_3Sb_2I_xBr_{9-x}$. *Angew. Chem., Int. Ed. Engl.* **2017**, *56* (23), 6528−6532.

(103) Rakita, Y.; Kedem, N.; Gupta, S.; Sadhanala, A.; Kalchenko, V.; Böhm, M. L.; Kulbak, M.; Friend, R. H.; Cahen, D.; Hodes, G. Low-Temperature Solution-Grown $CsPbBr_3$ Single Crystals and Their Characterization. *Cryst. Growth Des.* **2016**, *16* (10), 5717−5725.

(104) Zhang, H.; Liu, X.; Dong, J.; Yu, H.; Zhou, C.; Zhang, B.; Xu, Y.; Jie, W. Centimeter-Sized Inorganic Lead Halide Perovskite $CsPbBr_3$ Crystals Grown by an Improved Solution Method. *Cryst. Growth Des.* **2017**, *17* (12), 6426−6431.

(105) Trivedi, S.; Prochowicz, D.; Parikh, N.; Mahapatra, A.; Pandey, M. K.; Kalam, A.; Tavakoli, M. M.; Yadav, P. Recent Progress in Growth of Single-Crystal Perovskites for Photovoltaic Applications. *ACS Omega* **2021**, *6* (2), 1030−1042.

(106) Wu, X.; Trinh, M. T.; Niesner, D.; Zhu, H.; Norman, Z.; Owen, J. S.; Yaffe, O.; Kudisch, B. J.; Zhu, X. Y. Trap states in lead iodide perovskites. *J. Am. Chem. Soc.* **2015**, *137* (5), 2089−96.

(107) Kim, G.; An, S.; Hyeong, S.-K.; Lee, S.-K.; Kim, M.; Shin, N. Perovskite Pattern Formation by Chemical Vapor Deposition Using Photolithographically Defined Templates. *Chem. Mater.* **2019**, *31* (19), 8212−8221.

(108) Che, T.; Shen, C.; Gao, J.; Ji, X.; Kong, W.; Liu, Y. Size control of single-crystal perovskite nanoplatelets based on vapor deposition. *Opt. Mater.* **2020**, *107*, 110120.

(109) Wang, Y.; Guan, X.; Li, D.; Cheng, H.-C.; Duan, X.; Lin, Z.; Duan, X. Chemical vapor deposition growth of single-crystalline cesium lead halide microplatelets and heterostructures for optoelectronic applications. *Nano Research* **2017**, *10* (4), 1223−1233.

(110) Guo, P.; Hossain, M. K.; Shen, X.; Sun, H.; Yang, W.; Liu, C.; Ho, C. Y.; Kwok, C. K.; Tsang, S.-W.; Luo, Y.; Ho, J. C.; Yu, K. M. Room-Temperature Red-Green-Blue Whispering-Gallery Mode Lasing and White-Light Emission from Cesium Lead Halide Perovskite ($CsPbX_3$, X = Cl, Br, I) Microstructures. *Advanced Optical Materials* **2018**, *6* (3), 1700993.

(111) Mo, X.; Li, X.; Dai, G.; He, P.; Sun, J.; Huang, H.; Yang, J. All-inorganic perovskite $CsPbBr_3$ microstructures growth via chemical vapor deposition for high-performance photodetectors. *Nanoscale* **2019**, *11* (44), 21386−21393.

(112) Chen, C.; Han, T.-H.; Tan, S.; Xue, J.; Zhao, Y.; Liu, Y.; Wang, H.; Hu, W.; Bao, C.; Mazzeo, M.; Wang, R.; Duan, Y.; Yang, Y. Efficient Flexible Inorganic Perovskite Light-Emitting Diodes Fabricated with $CsPbBr_3$ Emitters Prepared via Low-Temperature in Situ Dynamic Thermal Crystallization. *Nano Lett.* **2020**, *20* (6), 4673−4680.

(113) Wang, S.; Yang, F.; Zhu, J.; Cao, Q.; Zhong, Y.; Wang, A.; Du, W.; Liu, X. Growth of metal halide perovskite materials. *Science China Materials* **2020**, *63* (8), 1438−1463.

(114) Clark, D. J.; Stoumpos, C. C.; Saouma, F. O.; Kanatzidis, M. G.; Jang, J. I. Polarization-selective three-photon absorption and subsequent photoluminescence in $CsPbBr_3$ single crystal at room temperature. *Phys. Rev. B* **2016**, *93* (19), 195202.

(115) Song, J.; Cui, Q.; Li, J.; Xu, J.; Wang, Y.; Xu, L.; Xue, J.; Dong, Y.; Tian, T.; Sun, H.; Zeng, H. Ultralarge All-Inorganic Perovskite Bulk Single Crystal for High-Performance Visible-Infrared Dual-Modal Photodetectors. *Advanced Optical Materials* **2017**, *5* (12), 1700157.

(116) Zhang, P.; Zhang, G.; Liu, L.; Ju, D.; Zhang, L.; Cheng, K.; Tao, X. Anisotropic optoelectronic properties of melt-grown bulk $CsPbBr_3$ single crystal. *J. Phys. Chem. Lett.* **2018**, *9* (17), 5040−5046.

(117) Zhang, P.; Hua, Y.; Li, X.; Zhang, L.; Liu, L.; Li, R.; Zhang, G.; Tao, X. Filter-free color image sensor based on $CsPbBr_{3-3n}X_{3n}$ (X = Cl, I) single crystals. *Journal of Materials Chemistry C* **2021**, *9* (8), 2840−2847.

(118) Arya, S.; Mahajan, P.; Gupta, R.; Srivastava, R.; Tailor, N. k.; Satapathi, S.; Sumathi, R. R.; Datt, R.; Gupta, V. A comprehensive review on synthesis and applications of single crystal perovskite halides. *Prog. Solid State Chem.* **2020**, *60*, 100286.

(119) Grancini, G.; D'Innocenzo, V.; Dohner, E. R.; Martino, N.; Srimath Kandada, A. R.; Mosconi, E.; De Angelis, F.; Karunadasa, H. I.; Hoke, E. T.; Petrozza, A. $CH_3NH_3PbI_3$ perovskite single crystals: surface photophysics and their interaction with the environment. *Chemical Science* **2015**, *6* (12), 7305−7310.

(120) Zhou, H.; Nie, Z.; Yin, J.; Sun, Y.; Zhuo, H.; Wang, D.; Li, D.; Dou, J.; Zhang, X.; Ma, T. Antisolvent diffusion-induced growth, equilibrium behaviours in aqueous solution and optical properties of $CH_3NH_3PbI_3$ single crystals for photovoltaic applications. *RSC Adv.* **2015**, *5* (104), 85344−85349.

(121) Liu, Y.; Sun, J.; Yang, Z.; Yang, D.; Ren, X.; Xu, H.; Yang, Z.; Liu, S. F. 20-mm-Large Single-Crystalline Formamidinium-Perovskite Wafer for Mass Production of Integrated Photodetectors. *Advanced Optical Materials* **2016**, *4* (11), 1829−1837.

(122) Zhumekenov, A. A.; Saidaminov, M. I.; Haque, M. A.; Alarousu, E.; Sarmah, S. P.; Murali, B.; Dursun, I.; Miao, X.-H.; Abdelhady, A. L.; Wu, T.; Mohammed, O. F.; Bakr, O. M. Formamidinium Lead Halide Perovskite Crystals with Unprecedented Long Carrier Dynamics and Diffusion Length. *ACS Energy Letters* **2016**, *1* (1), 32−37.

(123) Peng, J.; Xia, C. Q.; Xu, Y.; Li, R.; Cui, L.; Clegg, J. K.; Herz, L. M.; Johnston, M. B.; Lin, Q. Crystallization of $CsPbBr_3$ single

crystals in water for X-ray detection. *Nat. Commun.* **2021**, *12* (1), 1531.
(124) Cha, J. H.; Han, J. H.; Yin, W.; Park, C.; Park, Y.; Ahn, T. K.; Cho, J. H.; Jung, D. Y. Photoresponse of $CsPbBr_3$ and Cs_4PbBr_6 perovskite single crystals. *J. Phys. Chem. Lett.* **2017**, *8* (3), 565−570.
(125) He, Y.; Matei, L.; Jung, H. J.; McCall, K. M.; Chen, M.; Stoumpos, C. C.; Liu, Z.; Peters, J. A.; Chung, D. Y.; Wessels, B. W.; Wasielewski, M. R.; Dravid, V. P.; Burger, A.; Kanatzidis, M. G. High spectral resolution of gamma-rays at room temperature by perovskite $CsPbBr_3$ single crystals. *Nat. Commun.* **2018**, *9* (1), 1609−1616.
(126) Kanak, A.; Lishchuk, P.; Kuryliuk, V.; Kuzmich, A.; Lacroix, D.; Khalavka, Y.; Isaiev, M. Thermal conductivity of $CsPbBr_3$ halide perovskite: Photoacoustic measurements and molecular dynamics analysis. *THERMOPHYSICS 2020:25th International Meeting* **2020**, 020006.
(127) Nazarenko, O.; Kotyrba, M. R.; Worle, M.; Cuervo-Reyes, E.; Yakunin, S.; Kovalenko, M. V. Luminescent and Photoconductive Layered Lead Halide Perovskite Compounds Comprising Mixtures of Cesium and Guanidinium Cations. *Inorg. Chem.* **2017**, *56* (19), 11552−11564.
(128) Dursun, I.; De Bastiani, M.; Turedi, B.; Alamer, B.; Shkurenko, A.; Yin, J.; El-Zohry, A. M.; Gereige, I.; AlSaggaf, A.; Mohammed, O. F.; Eddaoudi, M.; Bakr, O. M. $CsPb_2Br_5$ Single Crystals: Synthesis and Characterization. *ChemSusChem* **2017**, *10* (19), 3746−3749.
(129) Acharyya, P.; Ghosh, T.; Pal, K.; Kundu, K.; Singh Rana, K.; Pandey, J.; Soni, A.; Waghmare, U. V.; Biswas, K. Intrinsically Ultralow Thermal Conductivity in Ruddlesden-Popper 2D Perovskite $Cs_2PbI_2Cl_2$: Localized Anharmonic Vibrations and Dynamic Octahedral Distortions. *J. Am. Chem. Soc.* **2020**, *142* (36), 15595−15603.
(130) Wang, K.; Yang, D.; Wu, C.; Shapter, J.; Priya, S. Monocrystalline perovskite photovoltaics toward ultrahigh efficiency? *Joule* **2019**, *3* (2), 311−316.
(131) Haque, M. A.; Troughton, J.; Baran, D. Processing-Performance Evolution of Perovskite Solar Cells: From Large Grain Polycrystalline Films to Single Crystals. *Adv. Energy Mater.* **2020**, *10* (13), 1902762.
(132) Song, Y.; Bi, W.; Wang, A.; Liu, X.; Kang, Y.; Dong, Q. Efficient lateral-structure perovskite single crystal solar cells with high operational stability. *Nat. Commun.* **2020**, *11* (1), 274−281.
(133) Min, H.; Lee, D. Y.; Kim, J.; Kim, G.; Lee, K. S.; Kim, J.; Paik, M. J.; Kim, Y. K.; Kim, K. S.; Kim, M. G.; Shin, T. J.; Seok, S., Il Perovskite solar cells with atomically coherent interlayers on SnO2 electrodes. *Nature* **2021**, *598* (7881), 444−450.
(134) Ye, T.; Fu, W.; Wu, J.; Yu, Z.; Jin, X.; Chen, H.; Li, H. Single-crystalline lead halide perovskite arrays for solar cells. *Journal of Materials Chemistry A* **2016**, *4* (4), 1214−1217.
(135) Liu, Y.; Ren, X.; Zhang, J.; Yang, Z.; Yang, D.; Yu, F.; Sun, J.; Zhao, C.; Yao, Z.; Wang, B.; Wei, Q.; Xiao, F.; Fan, H.; Deng, H.; Deng, L.; Liu, S. F. 120 mm single-crystalline perovskite and wafers: towards viable applications. *Science China Chemistry* **2017**, *60* (10), 1367−1376.
(136) Chen, Y. X.; Ge, Q. Q.; Shi, Y.; Liu, J.; Xue, D. J.; Ma, J. Y.; Ding, J.; Yan, H. J.; Hu, J. S.; Wan, L. J. General Space-Confined On-Substrate Fabrication of Thickness-Adjustable Hybrid Perovskite Single-Crystalline Thin Films. *J. Am. Chem. Soc.* **2016**, *138* (50), 16196−16199.
(137) Zhao, J.; Kong, G.; Chen, S.; Li, Q.; Huang, B.; Liu, Z.; San, X.; Wang, Y.; Wang, C.; Zhen, Y.; Wen, H.; Gao, P.; Li, J. Single crystalline $CH_3NH_3PbI_3$ self-grown on FTO/TiO_2 substrate for high efficiency perovskite solar cells. *Science Bulletin* **2017**, *62* (17), 1173−1176.
(138) Chen, Z.; Dong, Q.; Liu, Y.; Bao, C.; Fang, Y.; Lin, Y.; Tang, S.; Wang, Q.; Xiao, X.; Bai, Y.; Deng, Y.; Huang, J. Thin single crystal perovskite solar cells to harvest below-bandgap light absorption. *Nat. Commun.* **2017**, *8* (1), 1890.
(139) Chen, Z.; Turedi, B.; Alsalloum, A. Y.; Yang, C.; Zheng, X.; Gereige, I.; AlSaggaf, A.; Mohammed, O. F.; Bakr, O. M. Single-Crystal $MAPbI_3$ Perovskite Solar Cells Exceeding 21% Power Conversion Efficiency. *ACS Energy Letters* **2019**, *4* (6), 1258−1259.
(140) Alsalloum, A. Y.; Turedi, B.; Zheng, X.; Mitra, S.; Zhumekenov, A. A.; Lee, K. J.; Maity, P.; Gereige, I.; AlSaggaf, A.; Roqan, I. S.; Mohammed, O. F.; Bakr, O. M. Low-temperature crystallization enables 21.9% efficient single-crystal $MAPbI_3$ inverted perovskite solar cells. *ACS Energy Letters* **2020**, *5* (2), 657−662.
(141) Alsalloum, A. Y.; Turedi, B.; Almasabi, K.; Zheng, X.; Naphade, R.; Stranks, S. D.; Mohammed, O. F.; Bakr, O. M. 22.8%-Efficient single-crystal mixed-cation inverted perovskite solar cells with a near-optimal bandgap. *Energy Environ. Sci.* **2021**, *14* (4), 2263−2268.
(142) Huang, Y.; Zhang, Y.; Sun, J.; Wang, X.; Sun, J.; Chen, Q.; Pan, C.; Zhou, H. The Exploration of Carrier Behavior in the Inverted Mixed Perovskite Single-Crystal Solar Cells. *Advanced Materials Interfaces* **2018**, *5* (14), 1800224.
(143) Zhang, Z.; Geng, S.; Zhang, J.; Zhang, Z.; Xiong, Q.; Liang, L.; Mi, R.; Xiao, Z.; Scopelliti, R.; Gao, P. Atomic Permutation toward New Ruddlesden-Popper Two-Dimensional Perovskite with the Smallest Interlayer Spacing. *Journal of Physical Chmistry C* **2022**, *126* (19), 8268−8277.
(144) Yu, G.; Jiang, K.-J.; Gu, W.-M.; Li, Y.; Lin, Y.; Xu, Y.; Jiao, X.; Xue, T.; Zhang, Y.; Song, Y. Vacuum-Assisted Thermal Annealing of CsPbI3 for Highly Stable and Efficient Inorganic Perovskite Solar Cells. *Angew. Chem., Int. Ed. Engl.* **2022**, *61* (27), No. e2022037.
(145) Su, R.; Tiruvalam, R.; Logsdail, A. J.; He, Q.; Downing, C. A.; Jensen, M. T.; Dimitratos, N.; Kesavan, L.; Wells, P. P.; Bechstein, R.; et al. Designer titania-supported Au−Pd nanoparticles for efficient photocatalytic hydrogen production. *ACS Nano* **2014**, *8* (4), 3490−3497.
(146) Lee, L.; Baek, J.; Park, K. S.; Lee, Y. E.; Shrestha, N. K.; Sung, M. M. Wafer-scale single-crystal perovskite patterned thin films based on geometrically-confined lateral crystal growth. *Nat. Commun.* **2017**, *8*, 15882.
(147) Li, S. X.; Xu, Y. S.; Li, C. L.; Guo, Q.; Wang, G.; Xia, H.; Fang, H. H.; Shen, L.; Sun, H. B. Perovskite Single-Crystal Microwire-Array Photodetectors with Performance Stability beyond 1 Year. *Adv. Mater.* **2020**, *32* (28), No. e2001998.
(148) Liu, Y.; Zhang, Y.; Zhao, K.; Yang, Z.; Feng, J.; Zhang, X.; Wang, K.; Meng, L.; Ye, H.; Liu, M.; Liu, S. F. A 1300 mm(2) Ultrahigh-Performance Digital Imaging Assembly using High-Quality Perovskite Single Crystals. *Adv. Mater.* **2018**, *30*, No. e1707314.
(149) Lin, Q.; Armin, A.; Burn, P. L.; Meredith, P. Near infrared photodetectors based on sub-gap absorption in organohalide perovskite single crystals. *Laser & Photonics Reviews* **2016**, *10* (6), 1047−1053.
(150) Wang, K.; Wu, C.; Yang, D.; Jiang, Y.; Priya, S. Quasi-Two-Dimensional Halide Perovskite Single Crystal Photodetector. *ACS Nano* **2018**, *12* (5), 4919−4929.
(151) Li, J.; Wang, J.; Ma, J.; Shen, H.; Li, L.; Duan, X.; Li, D. Self-trapped state enabled filterless narrowband photodetections in 2D layered perovskite single crystals. *Nat. Commun.* **2019**, *10* (1), 806.
(152) Ge, C.; Zhai, W.; Tian, C.; Zhao, S.; Guo, T.; Sun, S.; Chen, W.; Ran, G. Centimeter-scale 2D perovskite $(PEA)_2PbBr_4$ single crystal plates grown by a seeded solution method for photodetectors. *RSC Adv.* **2019**, *9* (29), 16779−16783.
(153) Peng, W.; Yin, J.; Ho, K. T.; Ouellette, O.; De Bastiani, M.; Murali, B.; El Tall, O.; Shen, C.; Miao, X.; Pan, J.; Alarousu, E.; He, J. H.; Ooi, B. S.; Mohammed, O. F.; Sargent, E.; Bakr, O. M. Ultralow Self-Doping in Two-dimensional Hybrid Perovskite Single Crystals. *Nano Lett.* **2017**, *17* (8), 4759−4767.
(154) Liu, Y.; Zhang, Y.; Yang, Z.; Yang, D.; Ren, X.; Pang, L.; Liu, S. F. Thinness- and Shape-Controlled Growth for Ultrathin Single-Crystalline Perovskite Wafers for Mass Production of Superior Photoelectronic Devices. *Adv. Mater.* **2016**, *28* (41), 9204−9209.
(155) Yu, W.; Li, F.; Yu, L.; Niazi, M. R.; Zou, Y.; Corzo, D.; Basu, A.; Ma, C.; Dey, S.; Tietze, M. L.; Buttner, U.; Wang, X.; Wang, Z.; Hedhili, M. N.; Guo, C.; Wu, T.; Amassian, A. Single crystal hybrid perovskite field-effect transistors. *Nat. Commun.* **2018**, *9* (1), 5354.

(156) Tan, Z.; Wu, Y.; Hong, H.; Yin, J.; Zhang, J.; Lin, L.; Wang, M.; Sun, X.; Sun, L.; Huang, Y.; Liu, K.; Liu, Z.; Peng, H. Two-Dimensional $(C_4H_9NH_3)_2PbBr_4$ Perovskite Crystals for High-Performance Photodetector. *J. Am. Chem. Soc.* **2016**, *138* (51), 16612−16615.

(157) Huo, C.; Liu, X.; Wang, Z.; Song, X.; Zeng, H. High-Performance Low-Voltage-Driven Phototransistors through $CsPbBr_3$-2D Crystal van der Waals Heterojunctions. *Advanced Optical Materials* **2018**, *6* (16), 1800152.

(158) Bao, C.; Chen, Z.; Fang, Y.; Wei, H.; Deng, Y.; Xiao, X.; Li, L.; Huang, J. Low-Noise and Large-Linear-Dynamic-Range Photodetectors Based on Hybrid-Perovskite Thin-Single-Crystals. *Adv. Mater.* **2017**, *29* (39), 1703279.

(159) Yang, Z.; Deng, Y.; Zhang, X.; Wang, S.; Chen, H.; Yang, S.; Khurgin, J.; Fang, N. X.; Zhang, X.; Ma, R. High-Performance Single-Crystalline Perovskite Thin-Film Photodetector. *Adv. Mater.* **2018**, *30* (8), 16563−16572.

(160) Fang, Y.; Dong, Q.; Shao, Y.; Yuan, Y.; Huang, J. Highly narrowband perovskite single-crystal photodetectors enabled by surface-charge recombination. *Nat. Photonics* **2015**, *9* (10), 679−686.

(161) Dong, Y.; Zou, Y.; Song, J.; Song, X.; Zeng, H. Recent progress of metal halide perovskite photodetectors. *Journal of Materials Chemistry C* **2017**, *5* (44), 11369−11394.

(162) Yao, F.; Gui, P.; Zhang, Q.; Lin, Q. Molecular engineering of perovskite photodetectors: recent advances in materials and devices. *Molecular Systems Design & Engineering* **2018**, *3* (5), 702−716.

(163) Wang, H.; Kim, D. H. Perovskite-based photodetectors: materials and devices. *Chem. Soc. Rev.* **2017**, *46* (17), 5204−5236.

(164) Xie, C.; Liu, C. K.; Loi, H. L.; Yan, F. Perovskite-Based Phototransistors and Hybrid Photodetectors. *Adv. Funct. Mater.* **2020**, *30* (20), 1903907.

(165) Li, P.; Huang, W.; Xu, W.; Wei, X.; Chen, Y.; Meng, F.; Deng, W.; Liu, J. In Situ Polymer-Imprinted Architecture of Textured Perovskite Single-Crystal Sheets for Ultraweak-Light Photodetection. *Advanced Optical Materials* **2023**, *11*, 2201876.

(166) Kong, W.; Zhao, C.; Huang, T.; Li, X.; Xing, J.; Yu, Z.; Yang, P.; Li, W.; Yu, W. Accurate Adjusting the Lattice Strain of Triple-Cation and Mixed-Halide Perovskites for High-Performance Photodetector. *ACS APPLIED MATERIALS & INTERFACES* **2022**, *14* (24), 28154−28162.

(167) Chen, F.; Li, C.; Shang, C.; Wang, K.; Huang, Q.; Zhao, Q.; Zhu, H.; Ding, J. Ultrafast Response of Centimeter Scale Thin $CsPbBr_3$ Single Crystal Film Photodetector for Optical Communication. *Small* **2022**, *18* (45), 2203565.

(168) Huang, T.; Zhu, Z.; Zhao, C.; Kong, W.; Chen, X.; Li, R.; Yu, Z.; Shi, Z.; Li, D.; Yang, B.; Yu, W. Enhancing two-dimensional perovskite photodetector performance through balancing carrier density and directional transport. *Journal of Materials Chemistry A* **2022**, *10* (39), 21044−21052.

(169) Rao, H. S.; Chen, B. X.; Wang, X. D.; Kuang, D. B.; Su, C. Y. A micron-scale laminar $MAPbBr_3$ single crystal for an efficient and stable perovskite solar cell. *Chem. Commun. (Camb)* **2017**, *53* (37), 5163−5166.

(170) Yue, H.-L.; Sung, H.-H.; Chen, F.-C. Seeded Space-Limited Crystallization of $CH_3NH_3PbI_3$ Single-Crystal Plates for Perovskite Solar Cells. *Advanced Electronic Materials* **2018**, *4* (7), 1700655.

(171) Li, N.; Feng, A.; Guo, X.; Wu, J.; Xie, S.; Lin, Q.; Jiang, X.; Liu, Y.; Chen, Z.; Tao, X. Engineering the Hole Extraction Interface Enables Single-Crystal $MAPbI_3$ Perovskite Solar Cells with Efficiency Exceeding 22% and Superior Indoor Response. *Adv. Energy Mater.* **2022**, *12* (7), 2103241.

(172) Dong, Q.; Song, J.; Fang, Y.; Shao, Y.; Ducharme, S.; Huang, J. Lateral-Structure Single-Crystal Hybrid Perovskite Solar Cells via Piezoelectric Poling. *Adv. Mater.* **2016**, *28* (14), 2816−21.

(173) Wu, H.; Ge, Y.; Niu, G.; Tang, J. Metal Halide Perovskites for X-Ray Detection and Imaging. *Matter* **2021**, *4* (1), 144−163.

(174) Wegst, A. V. Radiation Detection and Measurement, by G. F. Knoll. *Medical Physics* **1980**, 7 (4), 397−398.

(175) Pan, W.; Wu, H.; Luo, J.; Deng, Z.; Ge, C.; Chen, C.; Jiang, X.; Yin, W.-J.; Niu, G.; Zhu, L.; Yin, L.; Zhou, Y.; Xie, Q.; Ke, X.; Sui, M.; Tang, J. $Cs_2AgBiBr_6$ single-crystal X-ray detectors with a low detection limit. *Nat. Photonics* **2017**, *11* (11), 726−732.

(176) Shen, Y.; Liu, Y.; Ye, H.; Zheng, Y.; Wei, Q.; Xia, Y.; Chen, Y.; Zhao, K.; Huang, W.; Liu, S. F. Centimeter-Sized Single Crystal of Two-Dimensional Halide Perovskites Incorporating Straight-Chain Symmetric Diammonium Ion for X-Ray Detection. *Angew. Chem., Int. Ed. Engl.* **2020**, *59* (35), 14896−14902.

(177) Nikl, M.; Yoshikawa, A. Recent R&D Trends in Inorganic Single-Crystal Scintillator Materials for Radiation Detection. *Advanced Optical Materials* **2015**, *3* (4), 463−481.

(178) Zhou, Y.; Chen, J.; Bakr, O. M.; Mohammed, O. F. Metal Halide Perovskites for X-ray Imaging Scintillators and Detectors. *ACS Energy Letters* **2021**, *6* (2), 739−768.

(179) Li, J.; Du, X.; Niu, G.; Xie, H.; Chen, Y.; Yuan, Y.; Gao, Y.; Xiao, H.; Tang, J.; Pan, A.; Yang, B. Rubidium Doping to Enhance Carrier Transport in CsPbBr3 Single Crystals for High-Performance X-Ray Detection. *ACS Appl. Mater. Interfaces* **2020**, *12* (1), 989−996.

(180) Wei, W.; Zhang, Y.; Xu, Q.; Wei, H.; Fang, Y.; Wang, Q.; Deng, Y.; Li, T.; Gruverman, A.; Cao, L.; Huang, J. Monolithic integration of hybrid perovskite single crystals with heterogenous substrate for highly sensitive X-ray imaging. *Nat. Photonics* **2017**, *11* (5), 315−321.

(181) Wang, W.; Meng, H.; Qi, H.; Xu, H.; Du, W.; Yang, Y.; Yi, Y.; Jing, S.; Xu, S.; Hong, F.; Qin, J.; Huang, J.; Xu, Z.; Zhu, Y.; Xu, R.; Lai, J.; Xu, F.; Wang, L.; Zhu, J. Electronic-Grade High-Quality Perovskite Single Crystals by a Steady Self-Supply Solution Growth for High-Performance X-ray Detectors. *Adv. Mater.* **2020**, *32* (33), No. e2001540.

(182) Myung, C. W.; Yun, J.; Lee, G.; Kim, K. S. A New Perspective on the Role of A-Site Cations in Perovskite Solar Cells. *Adv. Energy Mater.* **2018**, *8* (14), 1702898.

(183) Jodlowski, A. D.; Roldán-Carmona, C.; Grancini, G.; Salado, M.; Ralaiarisoa, M.; Ahmad, S.; Koch, N.; Camacho, L.; de Miguel, G.; Nazeeruddin, M. K. Large guanidinium cation mixed with methylammonium in lead iodide perovskites for 19% efficient solar cells. *Nature Energy* **2017**, *2* (12), 972−979.

(184) Huang, Y.; Qiao, L.; Jiang, Y.; He, T.; Long, R.; Yang, F.; Wang, L.; Lei, X.; Yuan, M.; Chen, J. A-site Cation Engineering for Highly Efficient $MAPbI_3$ Single-Crystal X-ray Detector. *Angew. Chem., Int. Ed. Engl.* **2019**, *58* (49), 17834−17842.

(185) Liu, Y.; Zheng, X.; Fang, Y.; Zhou, Y.; Ni, Z.; Xiao, X.; Chen, S.; Huang, J. Ligand assisted growth of perovskite single crystals with low defect density. *Nat. Commun.* **2021**, *12* (1), 1686.

(186) Song, Y.; Li, L.; Bi, W.; Hao, M.; Kang, Y.; Wang, A.; Wang, Z.; Li, H.; Li, X.; Fang, Y.; Yang, D.; Dong, Q. Atomistic Surface Passivation of $CH_3NH_3PbI_3$ Perovskite Single Crystals for Highly Sensitive Coplanar-Structure X-Ray Detectors. *Research* **2020**, *2020*, 5958243.

(187) Liu, Y.; Zhang, Y.; Zhu, X.; Feng, J.; Spanopoulos, I.; Ke, W.; He, Y.; Ren, X.; Yang, Z.; Xiao, F.; Zhao, K.; Kanatzidis, M.; Liu, S. F. Triple-Cation and Mixed-Halide Perovskite Single Crystal for High-Performance X-ray Imaging. *Adv. Mater.* **2021**, *33* (8), No. e2006010.

(188) Ji, C.; Wang, S.; Wang, Y.; Chen, H.; Li, L.; Sun, Z.; Sui, Y.; Wang, S.; Luo, J. 2D Hybrid Perovskite Ferroelectric Enables Highly Sensitive X-Ray Detection with Low Driving Voltage. *Adv. Funct. Mater.* **2020**, *30* (5), 1905529.

(189) Ji, C.; Li, Y.; Liu, X.; Wang, Y.; Zhu, T.; Chen, Q.; Li, L.; Wang, S.; Luo, J. Monolayer-to-Multilayer Dimensionality Reconstruction in a Hybrid Perovskite for Exploring the Bulk Photovoltaic Effect Enables Passive X-ray Detection. *Angew. Chem., Int. Ed. Engl.* **2021**, *60* (38), 20970−20976.

(190) Li, H.; Song, J.; Pan, W.; Xu, D.; Zhu, W. A.; Wei, H.; Yang, B. Sensitive and Stable 2D Perovskite Single-Crystal X-ray Detectors Enabled by a Supramolecular Anchor. *Adv. Mater.* **2020**, *32* (40), No. e2003790.

(191) He, Y.; Pan, W.; Guo, C.; Zhang, H.; Wei, H.; Yang, B. 3D/2D Perovskite Single Crystals Heterojunction for Suppressed Ions

Migration in Hard X-Ray Detection. *Adv. Funct. Mater.* **2021**, *31* (49), 2104880.
(192) Xu, Q.; Wang, X.; Zhang, H.; Shao, W.; Nie, J.; Guo, Y.; Wang, J.; Ouyang, X. $CsPbBr_3$ Single Crystal X-ray Detector with Schottky Barrier for X-ray Imaging Application. *ACS Applied Electronic Materials* **2020**, *2* (4), 879−884.
(193) Zhang, H.; Wang, F.; Lu, Y.; Sun, Q.; Xu, Y.; Zhang, B.-B.; Jie, W.; Kanatzidis, M. G. High-sensitivity X-ray detectors based on solution-grown caesium lead bromide single crystals. *Journal of Materials Chemistry C* **2020**, *8* (4), 1248−1256.
(194) Fan, Z.; Liu, J.; Zuo, W.; Liu, G.; He, X.; Luo, K.; Ye, Q.; Liao, C. Solution-Processed $MAPbBr_3$ and $CsPbBr_3$ Single-Crystal Detectors with Improved X-Ray Sensitivity via Interfacial Engineering. *physica status solidi (a)* **2020**, *217* (9), 2000104.
(195) Song, J.; Feng, X.; Li, H.; Li, W.; Lu, T.; Guo, C.; Zhang, H.; Wei, H.; Yang, B. Facile Strategy for Facet Competition Management to Improve the Performance of Perovskite Single-Crystal X-ray Detectors. *J. Phys. Chem. Lett.* **2020**, *11* (9), 3529−3535.
(196) Geng, X.; Feng, Q.; Zhao, R.; Hirtz, T.; Dun, G.; Yan, Z.; Ren, J.; Zhang, H.; Liang, R.; Tian, H.; Xie, D.; Yang, Y.; Ren, T.-L. High-Quality Single Crystal Perovskite for Highly Sensitive X-Ray Detector. *IEEE Electron Device Lett.* **2020**, *41* (2), 256−259.
(197) Li, L.; Liu, X.; Zhang, H.; Zhang, B.; Jie, W.; Sellin, P. J.; Hu, C.; Zeng, G.; Xu, Y. Enhanced X-ray Sensitivity of MAPbBr3 Detector by Tailoring the Interface-States Density. *ACS Appl. Mater. Interfaces* **2019**, *11* (7), 7522−7528.
(198) Wang, X.; Wu, Y.; Li, G.; Wu, J.; Zhang, X.; Li, Q.; Wang, B.; Chen, J.; Lei, W. Ultrafast Ionizing Radiation Detection by p−n Junctions Made with Single Crystals of Solution-Processed Perovskite. *Advanced Electronic Materials* **2018**, *4* (11), 1800237.
(199) Ye, F.; Lin, H.; Wu, H.; Zhu, L.; Huang, Z.; Ouyang, D.; Niu, G.; Choy, W. C. H. High-Quality Cuboid $CH_3NH_3PbI_3$ Single Crystals for High Performance X-Ray and Photon Detectors. *Adv. Funct. Mater.* **2019**, *29* (6), 1806984.
(200) Wei, H.; DeSantis, D.; Wei, W.; Deng, Y.; Guo, D.; Savenije, T. J.; Cao, L.; Huang, J. Dopant compensation in alloyed $CH_3NH_3PbBr_{3-x}Cl_x$ perovskite single crystals for gamma-ray spectroscopy. *Nat. Mater.* **2017**, *16* (8), 826−833.
(201) Li, X.; He, Y.; Kepenekian, M.; Guo, P.; Ke, W.; Even, J.; Katan, C.; Stoumpos, C. C.; Schaller, R. D.; Kanatzidis, M. G. Three-Dimensional Lead Iodide Perovskitoid Hybrids with High X-ray Photoresponse. *J. Am. Chem. Soc.* **2020**, *142* (14), 6625−6637.
(202) Wang, X.; Li, Y.; Xu, Y.; Pan, Y.; Zhu, C.; Zhu, D.; Wu, Y.; Li, G.; Zhang, Q.; Li, Q.; Zhang, X.; Wu, J.; Chen, J.; Lei, W. Solution-Processed Halide Perovskite Single Crystals with Intrinsic Compositional Gradients for X-ray Detection. *Chem. Mater.* **2020**, *32* (12), 4973−4983.
(203) Wu, J.; Wang, L.; Feng, A.; Yang, S.; Li, N.; Jiang, X.; Liu, N.; Xie, S.; Guo, X.; Fang, Y.; Chen, Z.; Yang, D.; Tao, X. Self-Powered $FA_{0.55}MA_{0.45}PbI_3$ Single-Crystal Perovskite X-Ray Detectors with High Sensitivity. *Adv. Funct. Mater.* **2022**, *32* (9), 2109149.
(204) Wang, H.; Wu, H.; Xian, Y.; Niu, G.; Yuan, W.; Li, H.; Yin, H.; Liu, P.; Long, Y.; Li, W.; Fan, J. Controllable CsxFA1-xPbI3 Single-Crystal Morphology via Rationally Regulating the Diffusion and Collision of Micelles toward High-Performance Photon Detectors. *ACS Appl. Mater. Interfaces* **2019**, *11* (14), 13812−13821.
(205) Zhang, B. B.; Liu, X.; Xiao, B.; Hafsia, A. B.; Gao, K.; Xu, Y.; Zhou, J.; Chen, Y. High-Performance X-ray Detection Based on One-Dimensional Inorganic Halide Perovskite $CsPbI_3$. *J. Phys. Chem. Lett.* **2020**, *11* (2), 432−437.